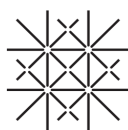


QUSTEC QCQT NCCR Summer School 2021

Engelberg, 14-17 September, 2021



University
of Basel

Department
of Physics



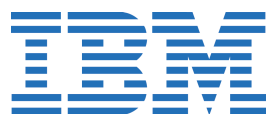
QUSTEC
Quantum Science and Technologies
at the European Campus



Spin Qubits in Silicon

National Centre of Competence in Research

SENSIRION



Contact

Carlo Ciaccia
University of Basel
Nanoelectronics Group
Tel.: +41 61 267 37 03
E-Mail: carlo.ciaccia@unibas.ch

Eoin Kelly
IBM Research Europe – Zurich
Quantum Technology Group
Tel.: +41 44 724 85 63
E-Mail: egk@zurich.ibm.com

Daniel Miller
IBM Research Europe – Zurich
Quantum Computing Group
Tel.: +41 44 724 87 62
E-Mail: DMI@zurich.ibm.com

Grazia Raciti
University of Basel
Nanophononics Group
Tel.: +41 61 207 56 77
E-Mail: grazia.raciti@unibas.ch

Konstantinos Tsoukalas
Quantum Technology Group
IBM Research Europe – Zurich
Tel.: +41 44 724 83 97
E-Mail: KTS@zurich.ibm.com

Contents

Contents	5
1 Program	9
2 Abstract Speakers	11
2.1 Jonathan Home: <i>"Quantum Information Processing with Trapped Ions"</i>	12
2.2 Guido Burkard: <i>"Hybrid Superconductor–Semiconductor Circuit QED and High-Fidelity Quantum Gates"</i>	12
2.3 Attila Geresdi: <i>"The physics and the road towards quantum technologies with Andreev bound states"</i>	12
2.4 Andreas Wallraff: <i>"Realizing the Surface Code: Quantum Error Correction with Superconducting Circuits"</i>	13
2.5 Sophia Economou: <i>"Variational quantum algorithms"</i>	13
2.6 Juan Sebastián Reparaz: <i>"Overview of Second Sound in Solid Materials: Searching for new alternatives to overcome Fourier heat transport"</i>	14
2.7 Andreas Fuhrer: <i>"Quantum Computing"</i>	15
2.8 Richard Warburton: <i>"A semiconductor-based single-photon source"</i>	15
2.9 Klaus Ensslin: <i>"Novel Quantum 2D Materials"</i>	15
2.10 Valerio Piazza: <i>"Novel Semiconducting Nanostructure for applications in Quantum Nano-electronics"</i>	16
3 Abstracts Students	17
3.1 Namrata Bansal: <i>"Investigating magnetic domains of Fe_3GeTe_3 by spin-polarized scanning tunneling microscopy"</i>	18
3.2 Andris Erglis: <i>"Nested Open Quantum Systems Approach to Photonic Bose-Einstein Condensation"</i>	19

3.3	Mohammed Guerboub: “ <i>First-principles molecular dynamics modelling of amorphous $GexSbyTez$ systems</i> ”	21
3.4	Jung-Ching Liu: “ <i>On-surface Synthesis on the Superconducting Substrate</i> ”	22
3.5	Giang N. Nguyen: “ <i>Quantum Interference of Identical Photons from Remote Quantum Dots</i> ”	24
3.6	Clemens Spinnler: “ <i>High-Frequency Optomechanics with Semiconductor Quantum Dots</i> ”	26
3.7	Pietro Vahramian: “ <i>A cryogenic hybrid trap for cold molecules and cold ions</i> ”	28
3.8	Viktoria Yurgens: “ <i>Laser writing of low-charge noise nitrogen-vacancy centers in diamond using a solid-immersion lens</i> ”	29
3.9	Alessandra Colla: “ <i>Entropy Production and Correlations in the driven Caldeira-Leggett model</i> ”	31
3.10	Nadia Olympia Antoniadis: “ <i>A quantum dot in a microcavity as a diode for single-photons</i> ”	33
3.11	Marcelo Janovitch Broinizi Pereira: “ <i>Quantum mean-square predictors of work</i> ”	35
3.12	Christoph Adelsberger: “ <i>Theory of Hole Spin Qubits in Ge Nanowire Quantum Dots: Effects of Orbital Magnetic Field, Anisotropies, and Strain</i> ”	37
3.13	Manuel Morgado: “ <i>Optimization of entanglement generation and state protection using Rydberg atoms</i> ”	39
3.14	Anmol Shukla: “ <i>Electronic Correlations and Nematic Fluctuations in $Fe_{1+y}Se_{0.5}Te_{0.5}$</i> ”	40
3.15	G Preisser: “ <i>Bipartite entropy build-up in open system matrix product state simulations</i> ”	42
3.16	Maria Spethmann: “ <i>Superconductor-mediated coupling of spin qubits and the impact of spin-orbit interaction</i> ”	44
3.17	Fabio Bersano: “ <i>Fabrication of FD-SOI Single Electron Transistors for spin qubits readout</i> ”	46
3.18	Richard Hess: “ <i>Local and nonlocal quantum transport due to Andreev bound states in finite Rashba nanowires with superconducting and normal sections</i> ”	48
3.19	Madhavakkannan Saravanan: “ <i>Storing single photons from an SPDC source in a Rb quantum memory</i> ”	50
3.20	Katharina Laubscher: “ <i>Fractional boundary charges with quantized slopes in interacting one- and two-dimensional systems</i> ”	52
3.21	Mikolaj Franciszek Roguski: “ <i>Precision spectroscopy and coherent manipulation of single trapped molecular ions</i> ”	54
3.22	Daria Sostina: “ <i>Development of a millikelvin STM for single spin resonance</i> ”	56
3.23	Apurba Das: “ <i>Quantum Simulations: Setting up increasingly complex quantum systems-atom by atom</i> ”	57
3.24	Julian Arnold: “ <i>Interpretable and unsupervised phase classification</i> ”	58
3.25	Yuhao Zhao: “ <i>Corner and Edge Charges in Systems with Chiral Hinge Modes</i> ”	60
3.26	Deepankar Sarmah: “ <i>Protecting RF-circuitry with superconducting low-pass filters</i> ”	61

3.27	Chaitanya Arya: <i>“Platforms for measuring the thermal conductivity of Superlattices Nanowires”</i> . . .	63
3.28	Salvatore Gatto: <i>“Hierarchical equations of motions (HEOM) approach to the study of thermodynamic uncertainty relations”</i>	65
3.29	Petar Tomic: <i>“Quality of gate-induced 2D hole gases in silicon with 10 nm oxide”</i>	67
3.30	Nicolas Forrer: <i>“Control of Growth Direction of Ge Nanowires”</i>	69
3.31	Arianna Nigro: <i>“Planar heterostructures for quantum dot spin qubits”</i>	71
3.32	Yashpreet Kaur: <i>“Thermal rectification in telescopic nanowires”</i>	74
3.33	Giulio De Vito and Grazia Raciti: <i>“Electrical and optical techniques to observe hydrodynamic phonon transport in 2D materials”</i>	77
3.34	Carlo Ciaccia: <i>“Towards Andreev Spin Qubits with Proximitized InAs 2DEG”</i>	80
4	Advertisement	81
4.1	Zurich Instruments	81
4.2	Linktronix	83

1

Program

NCCR QCQT QUSTEC Summer School 2021

	COMMUNITY		ACADEMIA	Thursday , Sept 16		INDUSTRY
	Tuesday, Sept 14		Wednesday, Sept 15	Thursday , Sept 16		Friday, Sept 17
		8:30-9:00	J. Nieden (Intro)			
		09:00-10:15	A. Fuhrer	J. Home	9:00-10:00	Successful Careers: P. Ruch
		Until 10:30	Coffee break	Coffee break	Until 10:15	Coffee break
Flexible	Arrival in Engelberg	10:30-11:45	V. Piazza	A. Wallraff	10:15-12:00	Qiskit: T. Palmen
		12:00-13:30	Lunch	Lunch	12:00-13:30	Lunch
	Group activities	13:30-14:45	R. Warburton	K. Ensslin	13:30-14:15	QNAMI: P. Maletinsky
		15:00-16:15	G. Burkard	S. Reparaz	14:30-17:30	Industry Fair
		Until 16:30	Coffee break	Coffee break		
After 16:00	Check-in Hotel	16:30-17:45	A. Geresdi	S. Economou		
18:30-20:00	Dinner at the Hotel	18:30-20:00	Dinner at the Hotel	Free time	18:00	Closing remarks Departure
20:00-22:00	Poster session Part 1	20:00-22:00	Poster session Part 2	Conference Dinner		

2

Abstract Speakers

2.1 Jonathan Home:

”Quantum Information Processing with Trapped Ions”

Department of Physics, ETH Zürich, Switzerland
Institute for Quantum Electronics
jhome@ethz.ch

Trapped atomic ions confined by electro-magnetic fields in ultra-high vacuum are extremely well isolated from the environment, giving excellent quantum coherence. They can be controlled using laser and microwave fields at the highest fidelities of any system in the laboratory today. For this reason they form one of the leading platforms for large-scale quantum computing, the future of which critically depends on gate error rates. I will review the basics of this approach, as well as giving an overview of the state of the art and prospects for scaling. Questions throughout the talk will be welcome.

2.2 Guido Burkard:

”Hybrid Superconductor–Semiconductor Circuit QED and High-Fidelity Quantum Gates”

University of Konstanz
guido.burkard@uni-konstanz.de

Synthetic spin-orbit coupling in the form of static magnetic field gradients enables circuit QED with spins in hybrid semiconductor-superconductor systems in the strong coupling limit [1]. This talk will review the basics and state of the art of circuit QED with spins and give an outlook to open problems and possible future research. The second part of the talk focuses on another use of magnetic field gradients which in combination with the exchange coupling allow for efficient two-qubit gates [2,3], using a technique that has recently been used to achieve high gate fidelities [4].

References:

- [1] G. Burkard et al., Nature Rev. Phys. 2, 129 (2020)
- [2] M. Russ et al., Phys. Rev. B 97, 085421 (2018)
- [3] D. M. Zajac et al., Science 359, 439 (2018)
- [4] A. Noiri et al., arXiv:2108.02626

2.3 Attila Geresdi:

"The physics and the road towards quantum technologies with Andreev bound states"

Chalmers University of Technology
Quantum Device Physics Laboratory
geresdi@chalmers.se

Andreev bound states are the basis of the microscopic picture of the Josephson effect, describing the coupling of two superconductors via a weak link by the formation of localized, single quasiparticle states decoupled from the continuum above the superconducting gap. With the recent improvement of superconductor-semiconductor nanoscale hybrid devices, the readout and manipulation of quasiparticles occupying the Andreev levels became experimentally feasible.

In this talk, I will first discuss the physics of Andreev levels and continue with the experimental settings for the measurement of them. Next, focusing on microwave domain measurements in a circuit QED setting, I will provide an overview of the coherent manipulation and readout of the quasiparticle charge and spin. Finally, I will comment on the connection with scalable quantum technologies.

2.4 Andreas Wallraff:

"Realizing the Surface Code: Quantum Error Correction with Superconducting Circuits"

Department of Physics, ETH Zurich, Switzerland
Quantum device lab
www.qudev.ethz.ch

Superconducting circuits are ideally suited for studying quantum phenomena at the macroscopic scale. Since complex circuits containing a few tens to a few hundreds of elements can be designed, fabricated, and operated with relative ease, they are one of the prime contenders for realizing quantum computers. Both academic and industrial labs work on realizing universal fault-tolerant quantum computers. Building systems, which can address commercially relevant computational problems continues to require significant conceptual and technological progress. In this lecture, I will first introduce how quantum error detection and correction is realized using the surface code. Then I will present our experimental results on quantum error detection in a distance-two surface code [1] and our progress towards error correction with a distance-three surface code. If time allows, I will discuss the challenges we face on the route toward large-scale quantum processors based on Reference:

[1] C. K. Andersen et al., Nature Physics 16, 875–880 (2020)

2.5 Sophia Economou:

”Variational quantum algorithms”

Virginia Tech Physics
Quantum Information Science, Condensed Matter Theory and Quantum Optics
economou@vt.edu

Variational quantum algorithms (VQAs) constitute a class of hybrid quantum-classical algorithms that are envisioned to be appropriate for noisy intermediate scale quantum processors. The majority of VQAs focus on quantum simulation, and particularly finding properties of many-body quantum systems, such as the ground state energies of complicated molecules. Other problems, such as optimization and machine learning are also being explored with this approach. In VQAs, the quantum processor is where the quantum state is variationally prepared and where measurements are made, while the classical computer performs optimization. In this tutorial, I will present the concept of VQAs and focus on their main aspects: state preparation, measurement, and optimization.

2.6 Juan Sebastián Reparaz:

”Overview of Second Sound in Solid Materials: Searching for new alternatives to overcome Fourier heat transport”

Institute of Materials Science of Barcelona - CSIC
jsreparaz@icmab.es

The study of heat transport beyond Fourier’s regime has attracted renewed interest in recent years. Great efforts have been performed to unravel the physical properties of thermal waves, as well as the experimental conditions that are necessary for their observation. Applications based on such concepts have been envisioned and discussed extensively already in many recent publications.[1]–[4] The spatio-temporal propagation of the temperature field in the form of waves is known as “second sound,” a term that was adopted in analogy to “first sound” (or simply “sound”, i.e. mechanical lattice vibrations). First and Second Sound are both described by a similar equation where the variables have a different physical meaning, i.e. pressure and temperature, respectively.[5] Second sound is known as the thermal transport regime where heat is carried by temperature waves. Its experimental observation was previously restricted to a small number of materials (solid He, Bi, NaF, SrTiO₃, and graphite), usually in rather narrow temperature windows. I will present a comprehensive overview on the experimental observation of second sound, with special emphasis on the occurrence of different flavours of thermal waves depending on the excitation/detection conditions. In particular, I will discuss the recent experimental observation of high frequency second sound,[6] which emerges by driving the system with a rapidly varying temperature field. This type of second sound, i.e. “high-frequency second sound”, is demonstrated in bulk natural Ge between 7 kelvin and room temperature by studying the phase lag of the thermal response under a harmonic high frequency external thermal excitation, and addressing the relaxation time and the propagation velocity of the heat waves.

References:

- [1] N. Li et al., Rev. Mod. Phys. 84, 1045–1066 (2012).
- [2] M. Maldovan, Appl. Phys. Rev. 1, 011305 (2014).
- [4] M. Gandolfi et al., Phys. Rev. Lett. 125, 265901 (2020).

- [5] R. J. Hardy, Phys. Rev. B 2, 1193–1207 (1970).
[6] A. Beardo et al., Science Advances 7, eabg4677 (2021).

2.7 **Andreas Fuhrer:** *”Quantum Computing”*

IBM Zurich Research Laboratory, Zurich, Switzerland
afu@zurich.ibm.com

In this lecture I will give a motivation why we should invest our time and resources into developing quantum computing as a new computing paradigm. I’ll present an overview of what I think quantum computing is, how it may outperform any classical computing system and where we are at IBM on the road towards useful quantum computing systems based on superconducting qubits. In the second part of the lecture, I’ll give an overview of an alternative solid-state quantum computing platform, namely spin qubits. At IBM Research in Zürich we have recently joined up with the University of Basel and other academic partners to work towards a scalable silicon spin qubit platform as part of NCCR SPIN. I’ll discuss the underlying principles of spin-based quantum computing, show how a bad transistor might be a good qubit, and outline the potential advantages of, specifically, hole spin qubits in silicon.

2.8 **Richard Warburton:** *”A semiconductor-based single-photon source”*

Department of Physics, University of Basel, Switzerland
Nanophotonics Group
richard.warburton@unibas.ch

The photon is the quantum particle of light. Photons constitute qubits, a means of encoding quantum information. Photons at optical frequencies enable quantum information to be sent efficiently over large distances – the photon therefore plays a central role in quantum technology. How can single photons be created and controlled? The merger of atomic and solid-state physics is providing new answers to these questions. One example concerns recent advances towards a deterministic source of single photons using a semiconductor. The talk will describe the basic building blocks, a semiconductor quantum dot and an optical microcavity, along with the quantum optical techniques used to analyse the output. Routes to creating more complex quantum states of light will be sketched.

2.9 Klaus Ensslin:

"Novel Quantum 2D Materials"

Department of Physics, ETH Zürich, Switzerland
Nanophysics Group
ensslin@phys.ethz.ch

2.10 Valerio Piazza:

"Novel Semiconducting Nanostructure for applications in Quantum Nano-electronics"

Postdoctoral Researcher
Laboratory of Semiconductor Materials (LMSC)
École Polytechnique Fédérale de Lausanne (EPFL)

3

Abstracts Students

Investigating magnetic domains of Fe_3GeTe_2 by spin-polarized scanning tunneling microscopy

Namrata Bansal,¹ Hung-Hsiang Yang,¹ Philipp Rüßmann,² Markus Hoffmann,² Lichuan Zhang,² Dongwook Go,² Amir-Abbas Haghighirad,³ Kaushik Sen,³ Matthieu Le Tacon,³ Yuriy Mokrousov,² and Wulf Wulfhekel¹

¹*Physikalisches Institut, Karlsruhe Institute of Technology, 76131 Karlsruhe, Germany*

²*Peter Grünberg Institut (PGI-1) and Institute for Advanced Simulation (IAS-1) Forschungszentrum Jülich GmbH, D-52425 Jülich*

³*Institute for Quantum Materials and Technologies, Karlsruhe Institute of Technology, 76131 Karlsruhe, Germany*

Two-dimensional (2D) magnets have great potential application in the field of spintronics. Natural 2D magnets can be found in magnetic layered 2D materials. Here we report on the magnetic structure of the van der Waal material Fe_3GeTe_2 (FGT) using low temperature (0.7 K) spin-polarized scanning tunneling microscopy (SP-STM). We have performed the out-of-plane magnetic imaging on FGT using chromium coated tungsten tips. Differential tunnelling conductance (dI/dV) maps were recorded to investigate the magnetic contrasts as function of magnetic field. We observe a shape transition of magnetic bubbles from elliptical to circular shape and finally collapsing of the topologically protected bubble at an out of plane magnetic field of 0.32 T. An inverse relation between the size of the magnetic bubbles and magnetic field was observed. SP-STM is a powerful tool for measuring the electronic and magnetic properties at the nanoscale. With the high lateral resolution, we resolved the domain wall profile and widths as function of magnetic field.

Nested Open Quantum Systems Approach to Photonic Bose-Einstein Condensation

Andris Erglis¹ and Stefan Yoshi Buhmann²

¹*Institute of Physics, University of Freiburg, Germany*

²*Institute of Physics, University of Kassel, Germany*

The photonic Bose–Einstein condensate is a recently observed collective ground state of a coupled light–matter system. We describe this quantum state based on macroscopic quantum electrodynamics in dispersing and absorbing environments. To describe the coupled photon–dye dynamics, we derive a master equation using a nested open quantum systems approach with all the necessary parameters to describe the condensation process.

In step 1, we derive constants responsible for spontaneous and cavity decay and laser pumping by tracing out the respective photonic baths. In step 2, we trace out the rovibrational modes of the molecules as an effective bath, which are influenced by dissipation constants derived in step 1. In this manner, we obtain the cavity mode absorption and emission rates of the dye molecules.

I. INTRODUCTION

Photonic Bose–Einstein condensation (BEC) is a phenomenon where photons reach thermal equilibrium with a well-defined effective temperature and macroscopically occupy the lowest energy state possible in the system.

For a long time, it was assumed that photons cannot form a BEC because of their non-interacting nature and because they disappear in the cavity walls when decreasing the temperature, as described in the black-body radiation model. It turns out that photon condensate is possible if one uses a dye-filled microcavity with highly reflective mirrors¹.

Here, we develop a general theory of condensation and derive all of the necessary decay and pumping constants using nested open quantum systems and macroscopic quantum electrodynamics (QED)^{2,3}. Our theoretical model consists of multiple systems and baths interacting with each other. We exploit the concept of nested open quantum systems, which is as follows: In step 1, we derive the master equation in Lindblad form for the cavity and molecular decay and pumping constants. Then, in step 2, we separate the remaining system Hamiltonian into the new system, bath, and interaction parts and derive the master equation for absorption/emission rates, which are now influenced by the previously derived rates from step 1.

II. THE MODEL

Fig. 1 shows the model of photon Bose-Einstein condensate. Inside a cavity that consists of two highly reflective mirrors, laser light is being pumped with a pumping rate Γ_{\uparrow} . Because the mirrors are not perfectly reflecting, photons may leak from the cavity with a rate κ . Inside the cavity, there are dye molecules, which can absorb the cavity mode photons with a rate $\Gamma(\delta_m)$. Molecules can emit photons in two ways: emitting photons into either a cavity or a non-cavity mode with rates $\Gamma(-\delta_m)$ and Γ_{\downarrow} , respectively. Once a critical value of photons (or pumping Γ_{\uparrow}) is exceeded inside a cavity, photon BEC can form, which is illustrated in Fig. 1 as a bright yellow line in the middle of the cavity.

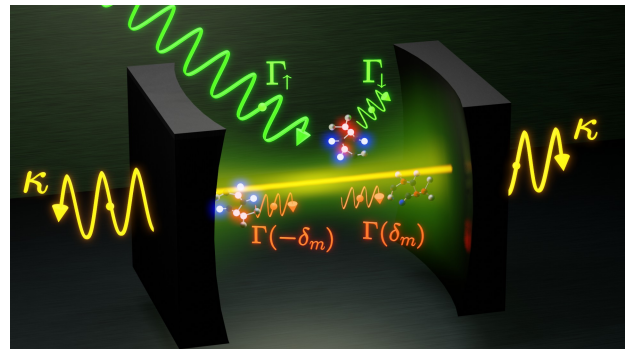


FIG. 1: Photon BEC setup. Photons from a laser enter a cavity with a rate Γ_{\uparrow} and are absorbed by a molecule with a rate $\Gamma(\delta_m)$. The molecule can emit a photon into a cavity mode m with a rate $\Gamma(-\delta_m)$. Photons are lost from the cavity by spontaneous emission from the molecule with a rate Γ_{\downarrow} or by cavity decay with a rate κ .

III. STEP 1: INTERMEDIATE MASTER EQUATION

Fig. 2 shows a schematic diagram of a nested open quantum system for our model. In step 1, there are three independent baths responsible for cavity and spontaneous decay and laser pumping (see Fig. 2). The system Hamiltonians H_{S1} and H_{S2} are coupled to the bath Hamiltonians H_{B1} , H_{B2} through the interaction Hamiltonians. Once we derive the master equation for the corresponding system, in step 2, we separate the remaining system Hamiltonian to a corresponding system, bath, and interaction Hamiltonians. Then we derive $\Gamma(\pm\delta_m)$.

Using the microscopic derivation of open quantum systems we derive the intermediate master equation:

$$\begin{aligned} \dot{\rho}_S &= -\frac{i}{\hbar}[H_S, \rho_S] \\ &- \sum_{m,i} \left\{ \frac{\kappa}{2} \mathcal{L}[a_m] + \frac{\Gamma_{\downarrow}}{2} \mathcal{L}[\sigma_i] + \frac{\Gamma_{\uparrow}}{2} \mathcal{L}[\sigma_i^{\dagger}] \right\} \rho_S. \end{aligned} \quad (1)$$

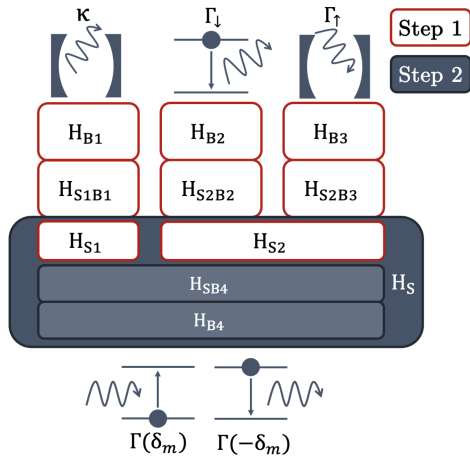


FIG. 2: Schematic representation of a nested open quantum systems approach for our model. In step 1 we derive the rates κ , Γ_{\downarrow} and Γ_{\uparrow} from baths B1, B2 and B3, and their interaction with systems S1 and S2. There are additional terms H_{B4} and H_{SB4} which we treat as part of the system in step 1. In step 2, they take on the roles of bath and system-bath interaction and from their interaction with H_{S1} and H_{S2} we derive $\Gamma(\pm\delta_m)$.

IV. STEP 2 - THE FINAL MASTER EQUATION

The next step is to redefine the remaining system Hamiltonian to be the new starting Hamiltonian $H_S \equiv$

H . We employ a dissipative interaction picture where the a and σ operators exhibit a dissipative time evolution. Integrating out the bath, we obtain the final master equation:

$$\begin{aligned} \dot{\rho}_S = & -\frac{i}{\hbar}[H_S, \rho_S] \\ & - \sum_{m,i} \left\{ \frac{\Gamma_{\downarrow}}{2} \mathcal{L}[\sigma_i] + \frac{\kappa}{2} \mathcal{L}[a_m] + \frac{\Gamma_{\uparrow}}{2} \mathcal{L}[\sigma_i^{\dagger}] \right. \\ & \left. + \frac{\Gamma(\delta_m)}{2} \mathcal{L}[a_m \sigma_i^{\dagger}] + \frac{\Gamma(-\delta_m)}{2} \mathcal{L}[a_m^{\dagger} \sigma_i] \right\} \rho_S. \end{aligned} \quad (2)$$

where now $\Gamma(\pm\delta_m) = \Gamma(\pm\delta_m)(\Gamma_{\downarrow}, \Gamma_{\uparrow}, \kappa)$ is a function of previously derived dissipative constants.

V. CONCLUSIONS

We have constructed a general theory and derived the necessary parameters to describe a photon Bose–Einstein condensation in a dye-filled cavity using a microscopic description of a molecule and photon interaction. We have demonstrated that $\Gamma(\pm\delta_m)$ are influenced by Γ_{\uparrow} , Γ_{\downarrow} and κ since molecule rovibrational states are influenced by cavity and spontaneous decay and laser pumping. The next step will be to use this technique by applying it to different geometries and calculating the threshold of the condensate.

¹ J. Klaers, J. Schmitt, F. Vewinger, and M. Weitz, *Bose–einstein condensation of photons in an optical microcavity*, Nature **468**, 545 (2010).

² H.-P. Breuer, F. Petruccione, et al., *The theory of open quantum systems* (Oxford University Press on Demand,

2002).

³ S. Y. Buhmann, *Dispersion Forces I: Macroscopic quantum electrodynamics and ground-state Casimir, Casimir–Polder and van der Waals forces*, vol. 247 (Springer, 2013).

First-principles molecular dynamics modelling of amorphous GexSbyTez systems

Mohammed Guerboub,¹ Assil Bouzid,² Mauro Boero,¹ Carlo Massobrio,¹ and Guido Ori

¹*Université de Strasbourg, CNRS, Institut de Physique et Chimie des Matériaux de Strasbourg, UMR 7504, F-67034 Strasbourg, France*

²*Institut de Recherche sur les Céramiques, UMR 7315 CNRS-Université de Limoges, Centre Européen de la Céramique, 12 rue Atlantis 87068 Limoges Cedex, France*

Gex-Sby-Tez (GST) chalcogenide-based systems represent one of the most established and successful class of phase change materials (PCMs)¹ that is nowadays tested in both memory devices and data storage applications. Their large use of this type of PCMs is due to its high switching speed and remarkable optical contrast between the amorphous and the crystalline phases. To exploit the properties of GST and optimize applications, a precise understanding of its atomic scale network and bonding properties is highly desirable. This can be highly beneficial to unveil the cause of current technological limitations involving resistance drift and threshold switching phenomena. In this work, we investigate through first-principles molecular dynamics (FPMD) combined with density functional theory (DFT) the structural properties of three amorphous GST compositions along the pseudobinary line of the GST ternary diagram between GeTe and Sb₂Te₃: Ge₂Sb₂Te₅ (GST-225), Ge₃Sb₂Te₆ (GST-326), and Ge₈Sb₂Te₁₁ (GST-8211)². In particular, great attention is devoted to the quantitative assessment of the total and partial structure factors, pair distribution functions and local environment coordination analysis. The degree of quantitative prediction of this work is evaluated by a thorough comparison with the available experimental data. This work paves the way to the building of FPMD observables database to be employed for the construction of a machine learning (ML) Gaussian Approximation Potentials (GAP) for the atomistic modelling of GST amorphous systems that will allow targeting larger size and times scales as a complementary work with respect to the original FPMD approach³.

Acknowledgments

We acknowledge Eucor – The European Campus for financial support through the QUSTEC funding from the European Union’s Horizon 2020 research and innovation

programme under the Marie Skłodowska-Curie Grant Agreement No. 847471. Calculation were performed by using resources from the Pole HPC Équipe@Meso of the University of Strasbourg.

¹ W. Zhang, R. Mazzarello, M. Wuttig, and E. Ma, *Designing crystallization in phase-change materials for universal memory and neuro-inspired computing*, Nat Rev Mater **4**, 150 (2019).

² A. Bouzid, G. Ori, M. Boero, E. Lampin, and C. Massobrio, *Atomic-scale structure of the glassy Ge₂Sb₂Te₅ phase change material: A quantitative assessment via first-*

principles molecular dynamics, Phys. Rev. B **96**, 224204 (2017).

³ A. P. Bartok and G. Csanyi, *Gaussian approximation potentials: A brief tutorial introduction*, International Journal of Quantum Chemistry **115**, 1051–1057 (2015).

On-surface Synthesis on the Superconducting Substrate

Jung-Ching Liu,¹ Philipp D'astolfo,¹ Carl Drechsel,¹ Xunshan Liu,² Silvio Decurtins,² Shi-Xia Liu,² Rémy Pawlak,¹ Wulf Wulfhekel,³ and Ernst Meyer¹

¹*Department of Physics, University of Basel, Klingelbergstrasse 82, 4056 Basel, Switzerland*

²*Department of Chemistry and Biochemistry, University of Bern, Freiestrasse 3, 3012 Bern, Switzerland*

³*Physikalisches Institut, Karlsruhe Institute of Technology, Wolfgang-Gaede-Str. 1, D-76131 Karlsruhe, Germany*

On-surface reactions are known for their ability to construct nanostructures with atomic precision. With the need for a convenient method to introduce superconductivity to carbon-based materials, we utilize Ullmann-type reaction to synthesize graphene nanoribbons (GNRs) on the superconducting Ag/Nb(110) substrate. Through the investigation with low-temperature scanning probe microscopy, we confirm the induced superconductivity on the Ag layer, and find four different chain-like structures synthesized on the surface. Our success in sample preparation provides a new path for studying the interplay between GNR topology and superconductivity.

I. INTRODUCTION

Due to the non-Abelian properties, braiding Majorana fermions is considered as a promising approach to realize topological quantum computation.^{1–3} The key to Majorana-based qubits lies on the emergence of topological superconductivity, which was observed as Majorana zero mode (MZM) in several hybrid condensed matter systems.^{4–6} With the prospect of tailoring complex structures that host topological superconductivity, on-surface synthesis is an ideal strategy, since the fabricated structure can be modified by selecting different molecule precursors.

To generate topological states specifically on graphene nanoribbons (GNRs) or carbon-based structures,^{7–9} Ullmann polymerization is an effective method. However, Ullmann reaction is so far restricted to noble metal surfaces^{10–12} and TiO₂.¹³ With the need of a convenient method to couple topological state and superconductivity on GNRs, we propose to perform on-surface reaction directly on the superconducting Ag/Nb(110) substrate.¹⁴

To test the feasibility of our scheme, we first grow Ag films under ultra-high vacuum (UHV) on Nb(110), and perform Ullmann reaction on Ag using 10,10'-dibromo-9,9'-bianthracene (DBBA) as the precursor. With the investigation by scanning tunneling microscopy (STM) and atomic force microscopy (AFM) at 4.7K, we confirm the proximity-induced superconductivity on the Ag layer, as well as nanostructures acquired via on-surface reactions. We believe the success in synthesis enables in-depth study regarding the role of GNR configurations on topological superconductivity.

II. RESULTS AND DISCUSSION

Our aim is to reproduce Ullmann polymerization on the superconducting Ag/Nb substrate as depicted in FIG. 1.¹² Upon molecule deposition, we find linear stackings situated mostly at step edges or defects. Similar to the reaction path on Ag(111), we observe polyanthrylene and organometallic chains as zigzag and armchair configurations under STM respectively. A further an-

neal is able to enforce cyclodehydrogenation, and lead to flattened straight and curved chains depending on the temperature.

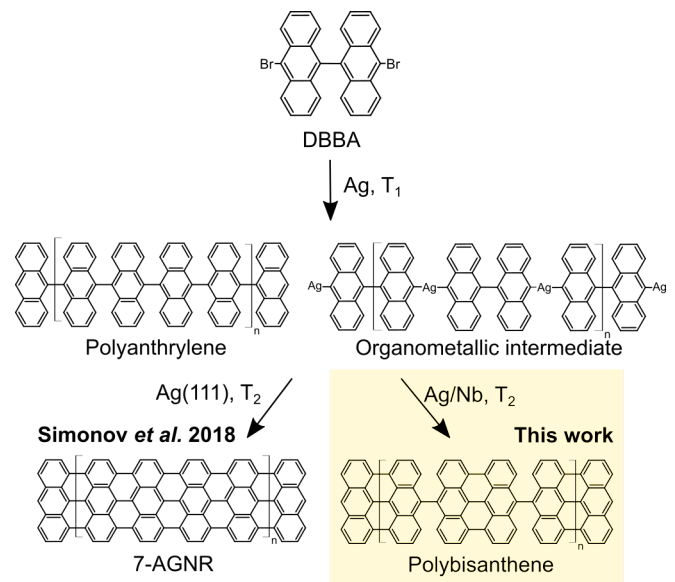


FIG. 1: The reaction path of DBBA on the superconducting Ag/Nb substrate.

By annealing the sample at 300°C, DBBA assemblies transform to flat straight chains. Close investigation of the structure is shown in FIG. 2a, b. From the AFM image (FIG. 2b), the straight chain is composed of bisanthrene molecules linked with single C-C bonds. This structure indicates that cyclodehydrogenation only occurs within a DBBA, whereas it does not take place between two bisanthenes. The deviation from the conventional reaction path might be the result of large involvement of the substrate during the synthesis. Nevertheless, polybisanthene is the first time being found during the Ullmann reaction using DBBA as the precursor.

Annealing the sample at 392°C further closes the C-C bond between adjacent bisanthenes. Instead of forming straight 7-carbon wide GNRs, we observe curved chains (FIG. 2c). The AFM investigation (FIG. 2d) reveals that

curved chains are irregularly fused nanographenes. Similar curved morphology was also observed by Simonov *et al.*¹² on Ag(111). They attributed the curved chain as the consequence of surface-assisted dehydrogenation at high annealing temperature. Since we find the same trend at high annealing temperature, we infer the high involvement of the substrate gives rise to fused nanographenes. Nonetheless, short segments of 7-AGNRs can be occasionally seen as marked by the red rectangle in FIG. 2d.

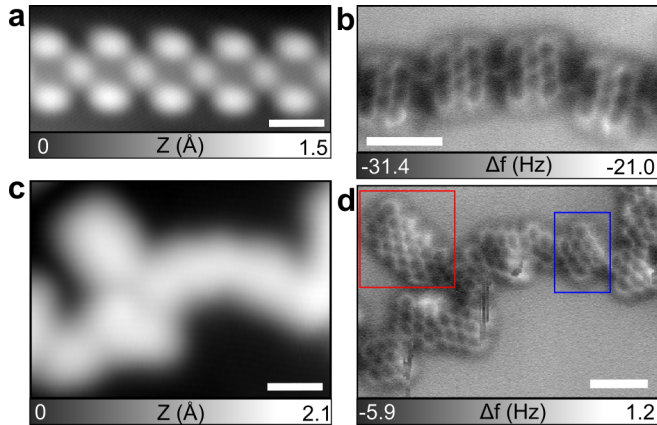


FIG. 2: STM and AFM images of polybisanthene and irregularly fused nanographene. (a) A close STM image of polybisanthene. (b) The AFM image of polybisanthene acquired by a CO-functionalized tip. (c) A close STM image of fused nanographene. (d) The AFM image of fused nanographene. All the scale bars are 1 nm.

III. CONCLUSION

Due to the low reactivity of the Ag surface, we are able to perform on-surface reactions on the superconducting Ag/Nb substrate. With the investigation of low-temperature STM and AFM, we find four different chain configurations, among which polybisanthene is synthesized for the first time. However, the large involvement of the substrate modifies the reaction pathway, and the chemical mechanism remains to be understood. Our exciting results demonstrate the possibility of fabricating complex frameworks on a superconductor. A promising application of this scheme is to synthesize doped 1D or 2D framework, or conjugate magnetic atoms with organic molecules. The consequent structures may generate MZMs or spin textures due to magnetic exchange and the interaction with superconductivity.

Acknowledgments

This project is under the scope of the QUSTEC program. The QUSTEC program has received funding from the European Union's Horizon 2020 research and innovation program under the Marie Skłodowska-Curie grant number 847471.

- ¹ J. Alicea, Y. Oreg, G. Refael, F. von Oppen, and M. P. A. Fisher, *Non-abelian statistics and topological quantum information processing in 1d wire networks*, Nat. Phys. **7**, 412 (2011).
- ² A. Stern and N. H. Lindner, *Topological quantum computation—from basic concepts to first experiments*, Science **339**, 1179 (2013).
- ³ S. D. Sarma, M. Freedman, and C. Nayak, *Majorana zero modes and topological quantum computation*, npj Quantum Inf. **1**, 15001 (2015).
- ⁴ L. Fu and C. L. Kane, *Superconducting proximity effect and majorana fermions at the surface of a topological insulator*, Phys. Rev. Lett. **100**, 096407 (2008).
- ⁵ S. Nadj-Perge, I. K. Drozdov, J. Li, H. Chen, S. Jeon, J. Seo, A. H. MacDonald, B. A. Bernevig, and A. Yazdani, *Observation of majorana fermions in ferromagnetic atomic chains on a superconductor*, Science **346**, 602 (2014).
- ⁶ S. Manna, P. Wei, Y. Xie, K. T. Law, P. A. Lee, and J. S. Moodera, *Signature of a pair of majorana zero modes in superconducting gold surface states*, PNAS **117**, 8775 (2020).
- ⁷ P. Delplace, D. Ullmo, and G. Montambaux, *Zak phase and the existence of edge states in graphene*, Phys. Rev. B **84**, 195452 (2011).
- ⁸ T. Cao, F. Zhao, and S. G. Louie, *Topological phases in graphene nanoribbons: Junction states, spin centers, and quantum spin chains*, Phys. Rev. Lett. **119**, 076401 (2017).
- ⁹ O. Gröning, S. Wang, X. Yao, C. A. Pignedoli, G. B. Barin, C. Daniels, A. Cupo, V. Meunier, X. Feng, A. Narita, et al., *Engineering of robust topological quantum phases in graphene nanoribbons*, Nature **560**, 209 (2018).
- ¹⁰ J. Cai, P. Ruffieux, R. Jaafar, M. Bieri, T. Braun, S. Blankenburg, M. Muoth, A. P. Seitsonen, M. Saleh, X. Feng, et al., *Atomically precise bottom-up fabrication of graphene nanoribbons*, Nature **466**, 470 (2010).
- ¹¹ L. Talirz, P. Ruffieux, and R. Fasel, *On-surface synthesis of atomically precise graphene nanoribbons*, Adv. Mater. **28**, 6222 (2016).
- ¹² K. A. Simonov, A. V. Generalov, A. S. Vinogradov, G. I. Svirskiy, A. A. Cafolla, C. McGuinness, T. Taketsugu, A. Lyalin, N. Mårtensson, and A. B. Preobrajenski, *Synthesis of armchair graphene nanoribbons from the 10,10-dibromo-9,9'-bianthracene molecules on ag(111): the role of organometallic intermediates*, Sci. Rep. **8**, 3506 (2018).
- ¹³ M. Kolmer, A.-K. Steiner, I. Izydorczyk, W. Ko, M. Englund, M. Szymonski, A.-P. Li, and K. Amsharov, *Rational synthesis of atomically precise graphene nanoribbons directly on metal oxide surfaces*, Science **369**, 571 (2020).
- ¹⁴ T. Tomanic, M. Schackert, W. Wulfhekel, C. Stürgers, and H. v. Löhneysen, *Two-band superconductivity of bulk and surface states in ag thin films on nb*, Phys. Rev. B **94**, 220503 (2016).

Quantum Interference of Identical Photons from Remote Quantum Dots

Giang N. Nguyen,¹ Liang Zhai,¹ Clemens Spinnler,¹ Julian Ritzmann,² Matthias C. Löbl,¹ Andreas D. Wieck,² Arne Ludwig,² Alisa Javadi,¹ and Richard J. Warburton¹

¹*Department of Physics, University of Basel, Klingelbergstrasse 82, CH-4056 Basel, Switzerland*

²*Lehrstuhl für Angewandte Festkörperphysik, Ruhr-Universität Bochum, DE-44780 Bochum, Germany*

Scaling the complexity of photonic quantum technologies requires photonic architectures containing a large number of indistinguishable photons. Semiconductor quantum dots are bright and fast sources of coherent single-photons. For applications, a significant roadblock is the poor quantum coherence upon interfering photons created by independent quantum dots. Here, we demonstrate two-photon interference with near-unity visibility using photons from remote quantum dots. Exploiting the quantum interference, we demonstrate a photonic controlled-not circuit and a high-fidelity entanglement between photons of different origins.

From large-scale quantum simulations [1] to multi-user quantum networks [2], scaling of photonic technologies requires a large number of indistinguishable photons. While current proof-of-principle demonstrations of photonic quantum applications rely mostly on parametric down-conversion sources [2], the adoption of semiconductor quantum dots (QDs) is a clear trend: QDs are on-demand emitters of single photons with significantly higher efficiency and photon generation-rate than down-conversion sources [3]. However, to create a large number of photons, the prevalent approach – active demultiplexing from a single QD [1] – is not optimal. It introduces additional losses and leads to a large resource overhead, limiting the maximal number of photons. A more advantageous approach is to create indistinguishable photons simultaneously from multiple QDs. This method facilitates scaling up to higher photon numbers without sacrificing efficiency. However, putting this idea into practice has been a challenge for many years [4, 5]. So far, the highest visibility [4] on interfering photons created by two separate QDs is limited to 51%.

In this work [6] we present a breakthrough in this direction: By interfacing the photons created by two separate GaAs QDs in distant cryostats, we report an unprecedentedly high two-photon interference visibility of $\mathcal{V} = 93\%$. We exploit the photon-photon interference to introduce entangling capabilities to the remote solid-state systems [Fig. 1(a)]. We demonstrate a controlled-not (CNOT) gate – the fundamental two-qubit logic in quantum algorithms – between two independently generated streams of photons. Utilising the CNOT operation, an entangled two-photon state is created: one photon is created by one semiconductor chip, the other photon is created by a separate chip far apart. Our results suggest that the GaAs QD platform represents a versatile launchpad for scalable photonic technologies.

Our semiconductor system consists of GaAs QDs in an $\text{Al}_{0.33}\text{Ga}_{0.67}\text{As}$ matrix grown by local droplet etching [7] [Figure 1(a)]. These QDs create single photons at deep-red wavelengths (750 – 800 nm), a very convenient spectral band: low-loss optical fibres, semiconductor lasers and highly efficient single-photon detectors are readily available. On account of ultra-pure materials and

a specially designed *n-i-p* diode, the noise in the system is very low. Close-to-lifetime-limited spectral linewidths and elimination of blinking [7] are observed on the majority of QDs in our heterostructure.

Owing to this low noise behaviour, we find close-to-unity Hong-Ou-Mandel (HOM) visibility not only between consecutive emitted photons (13 ns, set by pulsed-laser repetition period) but also for photons separated by $1\ \mu\text{s}$ (77th laser pulse). The photon indistinguishability is tested in an unbalanced Mach-Zender interferometer revealing HOM visibilities of $\mathcal{V}^{13\text{ns}} = (98.2 \pm 1.3)\%$ and $\mathcal{V}^{1\ \mu\text{s}} = (97.8 \pm 1.8)\%$ [6].

For multi-qubit applications, however, the ultimate goal is to achieve two-photon quantum-interference from independent single-photon sources. For QD-based sources, the challenge lies not only in matching the emitters spectrally and temporally but also in suppressing the noise over a huge bandwidth. QD1 and QD2 are located in two individual wafer pieces and are hosted in two cryostats separated by 20 metres (in fibre length). The environments of QD1 and QD2 are therefore completely uncorrelated. As such, the HOM interference of the photons created by two remote QDs is, to a certain extent, equivalent to the coalescence of two infinitely delayed photons from the same source. Despite the sensitivity to environmental noise, the remote HOM visibility is profound, $\mathcal{V}^{\text{remote}} = (93.0 \pm 0.8)\%$ [Fig. 1(b)]. We further emphasize that this unprecedentedly high visibility is not limited to these two QDs but is rather a sign of high quality QDs: photons interfered from a third QD matching spectrally and temporally with the other QDs show similar high indistinguishability.

The highly indistinguishable photons from distant QDs enable the creation of a quantum logical unit, a controlled-not gate. The information can be encoded into the two separate streams of photons, and the CNOT unit allows the creation of entanglement between photons of different origins [8]. We evaluate the gate performance using the input-output relations in both the computational basis $|H\rangle/|V\rangle$ and in the basis defined by the linear superpositions $|\pm\rangle = 1/\sqrt{2}(|H\rangle \pm |V\rangle)$. For every input state, the output state is mapped out using four simultaneous coincidence measurements in a quantum to-

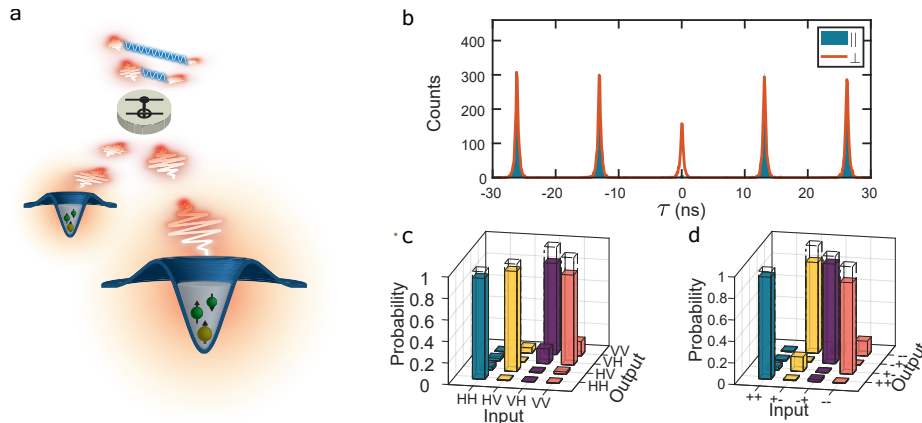


FIG. 1. **Two-photon interference from remote quantum dots** (a) A schematic view of an entangling gate between photons from two separate GaAs QDs. (b) HOM interference from photons generated by two remote QDs. The vanishing central peak indicates indistinguishable single photons. (c, d) Truth tables of the CNOT gate for $|H\rangle/|V\rangle$ and $|+\rangle/|-\rangle$ bases.

mography setup. The fidelity of the CNOT operation is $\mathcal{F}_{ZZ} = (88.90 \pm 5.34)\%$, and $\mathcal{F}_{XX} = (89.34 \pm 5.29)\%$ [Fig. 1(c, d)]. We calculate the bound for the quantum process fidelity [9] of our CNOT gate yielding $(78.24 \pm 7.53)\% < \mathcal{F}_{\text{proc}} < (88.90 \pm 5.34)\%$.

Finally, we demonstrate the ability to create maximally entangled states using the photonic qubits from remote QDs. This is the hallmark of the CNOT operation – by preparing the input state as $|-\rangle_c |V\rangle_t$, the Bell state $|\Psi^-\rangle = \frac{1}{\sqrt{2}}(|HV\rangle - |VH\rangle)$ is produced. We obtain an entanglement fidelity of $\mathcal{F}_{\Psi^-} = (85.02 \pm 0.97)\%$, which exceeds the threshold of $(2 + 3/\sqrt{2})/8 = 0.78$ for violating Bell inequalities [8]. To quantify the entanglement, we calculate the concurrence $C = (74.67 \pm 1.93)\%$ and

the linear entropy $S_L = (34.04 \pm 1.94)\%$. These values indicate a high level of entanglement and purity of the generated $|\Psi^-\rangle$ state.

In conclusion, we have demonstrated that GaAs QDs are interconnectable sources of indistinguishable single photons. Our work provides a feasible solution to the scaling bottleneck of photonic quantum technologies. From a quantum-information perspective, increasing the number of identical single-photons to ~ 50 will lead to quantum advantage in a photonic boson sampling experiment [10]. This number of indistinguishable photons is within reach, for instance using two or three low-noise GaAs QD sources together with current photonic technologies [1].

-
- [1] H. Wang, J. Qin, X. Ding, M.-C. Chen, S. Chen, X. You, Y.-M. He, X. Jiang, L. You, Z. Wang, et al., *Boson sampling with 20 input photons and a 60-mode interferometer in a 10^{14} -dimensional Hilbert space*, Phys. Rev. Lett. **123**, 250503 (2019).
- [2] D. Llewellyn, Y. Ding, I. I. Faruque, S. Paesani, D. Bacco, R. Santagati, Y.-J. Qian, Y. Li, Y.-F. Xiao, M. Huber, et al., *Chip-to-chip quantum teleportation and multi-photon entanglement in silicon*, Nat. Phys. **16**, 148 (2020).
- [3] N. Tomm, A. Javadi, N. O. Antoniadis, D. Najer, M. C. Löbl, A. R. Korsch, R. Schott, S. R. Valentin, A. D. Wieck, A. Ludwig, et al., *A bright and fast source of coherent single photons*, Nat. Nanotechnol. **16**, 399 (2021).
- [4] M. Reindl, K. D. Jöns, D. Huber, C. Schimpf, Y. Huo, V. Zwiller, A. Rastelli, and R. Trotta, *Phonon-assisted two-photon interference from remote quantum emitters*, Nano Lett. **17**, 4090 (2017).
- [5] M. Zopf, T. Macha, R. Keil, E. Uruñuela, Y. Chen, W. Alt, L. Ratschbacher, F. Ding, D. Meschede, and O. G. Schmidt, *Frequency feedback for two-photon interference from separate quantum dots*, Phys. Rev. B **98**, 161302 (2018).
- [6] L. Zhai, G. N. Nguyen, C. Spinnler, J. Ritzmann, M. C. Löbl, A. D. Wieck, A. Ludwig, A. Javadi, and R. J. Warburton, *Quantum interference of identical photons from remote quantum dots*, arXiv: 2106.03871 (2021).
- [7] L. Zhai, M. C. Löbl, G. N. Nguyen, J. Ritzmann, A. Javadi, C. Spinnler, A. D. Wieck, A. Ludwig, and R. J. Warburton, *Low-noise GaAs quantum dots for quantum photonics*, Nat. Commun. **11**, 4745 (2020).
- [8] N. Kiesel, C. Schmid, U. Weber, R. Ursin, and H. Weinfurter, *Linear optics controlled-phase gate made simple*, Phys. Rev. Lett. **95**, 210505 (2005).
- [9] Y.-M. He, Y. He, Y.-J. Wei, D. Wu, M. Atatüre, C. Schneider, S. Höfling, M. Kamp, C.-Y. Lu, and J.-W. Pan, *On-demand semiconductor single-photon source with near-unity indistinguishability*, Nat. Nanotechnol. **8**, 213 (2013).
- [10] R. Uppu, L. Midolo, X. Zhou, J. Carolan, and P. Lodahl, *Single-photon quantum hardware: towards scalable photonic quantum technology with a quantum advantage*, arXiv: 2103.01110 (2021).

High-Frequency Optomechanics with Semiconductor Quantum Dots

Clemens Spinnler,¹ Giang N. Nguyen,¹ Liang Zhai,¹ Alisa Javadi,¹ Matthias C. Löbl,¹ Andreas D. Wieck,² Arne Ludwig,² Ying Wang,³ Leonardo Midolo,³ Peter Lodahl,³ and Richard J. Warburton¹

¹*Department of Physics, University of Basel, Klingelbergstrasse 82, CH-4056 Basel, Switzerland*

²*Lehrstuhl für Angewandte Festkörperphysik, Ruhr-Universität Bochum, DE-44780 Bochum, Germany*

³*Niels Bohr Institute, University of Copenhagen, Blegdamsvej 17, Copenhagen DK-2100, Denmark*

Quantum dot optomechanics was proposed by Wilson-Rae et al. in 2004. To date, several successful attempts were made to couple quantum dots to the Brownian motion of MHz mechanical resonators. Coupling quantum dots to GHz phonons, however, remains challenging and so far relied on the additional excitation of mechanical motion. Here, we present a route to Brownian-motion quantum dot optomechanics in the sideband-resolved regime for the first time.

Coupling of mechanical motion to optical fields is of fundamental interest and has recently found great success using optical cavities and miniaturized mechanical resonators. This includes not only resolved-sideband cooling¹ but also squeezed light², wavelength conversion³, and entanglement between two spatially separated mechanical modes⁴. To date, coupling of semiconductor quantum dots (QDs) to MHz-phonons was achieved using mechanical resonators such as trumpets⁵ or cantilever-like structures⁶. Further, GHz QD optomechanics was shown by coupling QDs to piezomechanically excited surface acoustic waves⁷.

The coupling of quantum dots to mechanical resonators is of non-linear nature by itself whereas the coupling of optical cavities to mechanical resonators is linearized by the classical optical driving field inside the cavity. Though the linearized coupling of optical cavities has advantages in many aspects, e.g. optomechanical heating and cooling, QDs are better candidates for operations involving single-photons and single-phonons. Working with optical cavities in the single-photon limit, as needed for mechanical entanglement, can only be achieved by driving with highly attenuated laser fields, leading to a low photon count rate. In contrary, the single-photon rate of a QD is mainly limited by its lifetime.

Here, we present a design for optomechanical coupling of QDs to GHz-frequency mechanical resonators. The two main criteria for such systems to be addressed are a well confined mechanical mode, to achieve small mode volumes and thus high coupling rates, and also to reduce the mechanical dissipation. The QDs are incorporated in a 180 nm thin nano-structured membrane, Fig. 1 (c). The nanostructure is fabricated using soft-mask electron-beam lithography followed by a selective under-etching process of an underlying sacrificial layer.

The fundamental mechanical breathing mode of the mechanical resonator at $\omega_m/2\pi = 2$ GHz is surrounded by a phononic-bandgap shield⁸ which confines the mechanical motion to a small mode volume and reduces the radiation loss to the surrounding substrate, Fig. 1 (a) and (b). Using a finite-element simulation and deformation potential couplings⁹ we estimate the vacuum

optomechanical coupling rate g_0 to be several MHz. More specifically, for the design shown in Fig. 1 (b), the coupling rate is estimated to be $g_0/2\pi = 5.5$ MHz.

The QDs of choice are either self-assembled InAs QDs embedded in a GaAs matrix¹⁰ or droplet-etched GaAs QDs embedded in a AlGaAs matrix¹¹. In the current membrane-design the QDs are placed in a *p-i-n* diode structure. This allows to deterministically charge the QD with single electrons but also helps to stabilize the charge environment of the QD, resulting in narrow optical linewidths of $\kappa/2\pi \approx 1$ GHz. Together with the high mechanical frequency, Brownian motion optomechanics in the sideband-resolved regime ($\omega_m \gg \kappa$) is possible.

We further present basic mechanical characterization of membrane-cantilevers fabricated on the same sample as the phononic nanostructures. Fig. 1 (d) shows a scanning electron microscope image of a 10 μm long, 1 μm wide, and 180 nm thick cantilever. The mechanical properties are optically characterized using a low-finesse optical cavity ($l_{\text{cav}} = 1.15 \mu\text{m}$) in the hollow space below the cantilever, formed during the under-etch procedure.

The measured mechanical quality factor of a 15 μm long cantilever at room temperature and at 4.2 K is $Q_m^{\text{RT}} = 400$ and $Q_m^{4\text{K}} = 5000$, respectively. The noise spectrum of the reflected laser beam shows a Lorentzian lineshape, Fig. 1 (e). Since the cantilever is very thin, we speculate that one of the main limiting loss channels is surface losses¹². When increasing the probe laser power, the effective mechanical quality factor increases and the mechanical motion is amplified due to the optomechanical interaction. At a threshold of 110 μW , the intrinsic mechanical damping is compensated by the optomechanically induced interaction and the cantilever undergoes self-sustained oscillations - leading to mechanical-lasing, Fig. 1 (f).

To conclude, the design presented here promises high frequency and high quality factor optomechanics with deformation potential coupled QDs. The vacuum optomechanical coupling rate lies in the range of a few MHz which is comparable to the state-of-the art cavity optomechanical devices⁴.

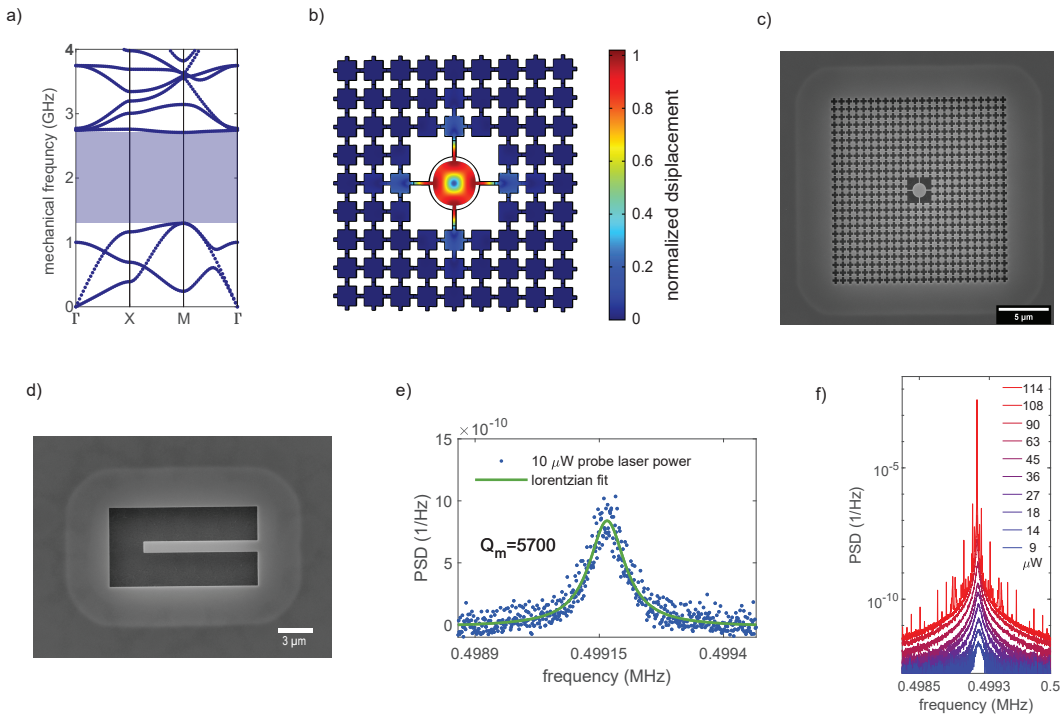


FIG. 1: **Optomechanical structures and characterization** (a) Band-structure for even modes of the phononic shield shown in (b). The shield opens up a phononic bandgap around the mechanical breathing mode of 2 GHz. (b) Comsol study of the fundamental in-plane breathing mode, surrounded by the phononic shield, showing a well localized in-plane mode. (c) Scanning electron microscope image of the membrane-nanostructure incorporating the QDs in the centre of the slab. (d) Scanning electron microscope image of a membrane-cantilever. The membrane hosts the InAs QDs embedded in a *p-i-n* diode structure. (e) Mechanical noise spectrum measured via the optical under-etch cavity. (f) Same as in (e) but as a function of increasing laser power. At a threshold of about 110 μW the mechanical cantilever undergoes self-sustained oscillations.

Acknowledgments

The work was supported by NCCR QSIT and SNF Project No. 200020 175748. LZ, GNN, AJ received funding from the European Union's Horizon 2020 Re-

search and Innovation Programme under the Marie Skłodowska-Curie grant agreement No. 721394 (4PHOTON), No. 861097 (QUDOT-TECH), and No. 840453 (HiFig), respectively.

- ¹ A. Schliesser, R. Rivière, G. Anetsberger, O. Arcizet, and T. J. Kippenberg, *Nature Physics* **4**, 415 (2008).
- ² A. H. Safavi-Naeini, S. Gröblacher, J. T. Hill, J. Chan, M. Aspelmeyer, and O. Painter, *Nature* **500**, 185 (2013).
- ³ J. T. Hill, A. H. Safavi-Naeini, J. Chan, and O. Painter, *Nature Communications* **3**, 1196 (2012).
- ⁴ R. Riedinger, A. Wallucks, I. Marinković, C. Löschnauer, M. Aspelmeyer, S. Hong, and S. Gröblacher, *Nature* **556**, 473 (2018).
- ⁵ M. Munsch, A. V. Kuhlmann, D. Cadeddu, J.-M. Gérard, J. Claudon, M. Poggio, and R. J. Warburton, *Nature Communications* **8**, 76 (2017).
- ⁶ S. Carter, A. Bracker, G. Bryant, M. Kim, C. Kim, M. Zhalutdinov, M. Yakes, C. Czarnocki, J. Casara, M. Scheibner, and D. Gammon, *Physical Review Letters* **121**, 246801 (2018).
- ⁷ M. Weiß, D. Wigger, D. Wigger, D. Wigger, M. Nägele, K. Müller, J. J. Finley, T. Kuhn, P. Machnikowski, and H. J. Krenner, *Optica* **8**, 291 (2021).

- ⁸ A. H. Safavi-Naeini and O. Painter, *Optics Express* **18**, 14926 (2010).
- ⁹ I. Yeo, P.-L. de Assis, A. Gloppe, E. Dupont-Ferrier, P. Verlot, N. S. Malik, E. Dupuy, J. Claudon, J.-M. Gérard, A. Auffèves, G. Nogues, S. Seidelin, J.-P. Poizat, O. Arcizet, and M. Richard, *Nature Nanotechnology* **9**, 106 (2014).
- ¹⁰ M. C. Löbl, I. Söllner, A. Javadi, T. Pregolato, R. Schott, L. Midolo, A. V. Kuhlmann, S. Stobbe, A. D. Wieck, P. Lodahl, A. Ludwig, and R. J. Warburton, *Physical Review B* **96**, 165440 (2017).
- ¹¹ L. Zhai, M. C. Löbl, G. N. Nguyen, J. Ritzmann, A. Javadi, C. Spinnler, A. D. Wieck, A. Ludwig, and R. J. Warburton, *Nature Communications* **11**, 4745 (2020).
- ¹² K. Yasumura, T. Stowe, E. Chow, T. Pfafman, T. Kenny, B. Stipe, and D. Rugar, *Journal of Microelectromechanical Systems* **9**, 117 (2000).

A cryogenic hybrid trap for cold molecules and cold ions

Pietro Vahramian¹, Claudio von Planta¹, Dominik Haas¹,
Christian Mangeng¹, Richard Karl¹, Yanning Yin¹,
Dongdong Zhang², Thomas Kierspel¹, Stefan Willitsch¹

¹*Department of Chemistry, University of Basel, Basel, Switzerland*

²*Institute of Atomic and Molecular Physics, Jilin University, Changchun, China*

At cold (\sim mK) translational temperatures, the physics of ion-molecule chemical reactions is a vastly uncharted territory. Their manipulation and control has made rapid progress in the past years [1], both for neutral [2] and charged [3] molecules, reaching even the coherent control on the internal state at the single particle level [4].

Here the goal is to study the chemistry of cold, reactive collisions between simultaneously trapped *neutral polar molecules* (e.g. OH) and *molecular* or *atomic ions* (e.g. Ca^+ and N_2^+). Employing state-of-the-art techniques, we aim at overlapping physically the two trapped species, while retaining control over the internal state of the ion and observing state-dependent reaction rates in the millikelvin temperature range.

As initial step we will study collisions between atomic ions and polar molecules. In a later stage, molecular ions would be cooled and coherently manipulated by means of auxiliary Ca^+ ions and quantum-non demolition measurement techniques, as recently demonstrated [4].

In my poster I will introduce the experiment developed in the previous years. The heart of the setup is a cryogenic hybrid trap consisting of a linear RF ion trap and a static magnetic trap for neutral molecules, where long-term trapping of Stark decelerated paramagnetic radicals has already been demonstrated [2].

I will also report on the recent implementation of an advanced switching scheme of the Stark decelerator, first developed in [5], that increases the number of molecules trapped by a factor of 7, greatly enhancing the number of collisions expected to be observed and the statistic of the experiment overall.

References

- [1] Dulieu, Olivier, et al. "*Physics and chemistry of cold molecules.*" *Physical Chemistry Chemical Physics* 13.42 (2011): 18703-18704.
- [2] Haas, Dominik, et al. "*Long-term trapping of Stark-decelerated molecules.*" *Communications Physics* 2.1 (2019): 1-7.
- [3] Willitsch, Stefan. "*Chemistry with controlled ions.*" *Adv. Chem. Phys* 162 (2017): 307-340.
- [4] Sinhal, Mudit, et al. "*Quantum-nondemolition state detection and spectroscopy of single trapped molecules.*" *Science* 367.6483 (2020): 1213-1218.
- [5] Reens, David, et al. "*Beyond the limits of conventional Stark deceleration.*" *Physical Review Research* 2.3 (2020): 033095.

Laser writing of low-charge noise nitrogen-vacancy centers in diamond using a solid-immersion lens

Viktoria Yurgens,¹ Josh A. Zuber,¹ Sigurd Flågan,¹ Marta De Luca,¹ Brendan J. Shields,¹ Ilaria Zardo,¹ Patrick Maletinsky,¹ Richard J. Warburton,¹ and Tomasz Jakubczyk^{1,2}

¹Department of Physics, University of Basel, CH-4056 Basel, Switzerland

²Faculty of Physics, University of Warsaw, 02-093 Warsaw, Poland

We report on pulsed-laser induced generation of nitrogen-vacancy (NV) centers in diamond facilitated by a solid-immersion lens (SIL). The SIL enables laser writing over a wide range of pulse energies and allows vacancies to be formed close to a diamond surface without inducing surface graphitization. We operate in the previously unexplored regime where lattice vacancies are created following tunneling breakdown. We demonstrate the positioning ability of laser writing by creating NV center arrays at arbitrary depth and in-plane locations within a diamond sample, presenting optical linewidth distributions with means as low as 62.1 MHz. The results include spectral diffusion induced by off-resonant repump, which emphasizes the exceptionally low charge-noise environment of laser-written NVs – a crucial prerequisite for the realization of distributed quantum networks based on spins in diamond.

I. INTRODUCTION

The negatively charged nitrogen-vacancy (NV) center in diamond is among the most promising solid-state systems implementations of a quantum bit, with recent progress demonstrated in the implementation of an NV-based multinode quantum network [1]. However, the interconnection of many NV centers for large-scale quantum networks still suffers from the low generation rate of indistinguishable photons from individual NV centers.

To this end, an open Fabry-Perot microcavity coupled to an NV center in diamond is a promising spin-photon interface [2, 3]. It improves the collection efficiency and enables easy optical access, mode-matching, and *in situ* tuning of the cavity resonance to an emitter, using the Purcell effect to increase the coherent photon flux. Implementation of diamond into the system requires thinning it down to $\sim 1 \mu\text{m}$ thickness while maintaining the NV optical coherence, a well-known challenge with standard NV creation methods such as nitrogen-ion implantation followed by high-temperature annealing [4–6]. Due to its permanent electric dipole moment, the NV center is particularly sensitive to the local electric field, and so charge noise in its surroundings lead to random spectral jumps of the zero-phonon line (ZPL) frequency. Methods of NV center creation that do not result in the formation of charge traps in the form of parasitic defects and impurities are therefore desired. Recent studies have further shown that NV centers formed from implanted nitrogen ions have on average much poorer optical quality than their counterparts formed from native nitrogen [7, 8].

II. LASER WRITING OF NV CENTERS

Laser writing, a recently developed method for NV center creation [9], is based on irradiation of a diamond sample with single high-energy femtosecond pulses. The laser pulses create vacancies; NV centers form in a subsequent thermal annealing step in which the mobile va-

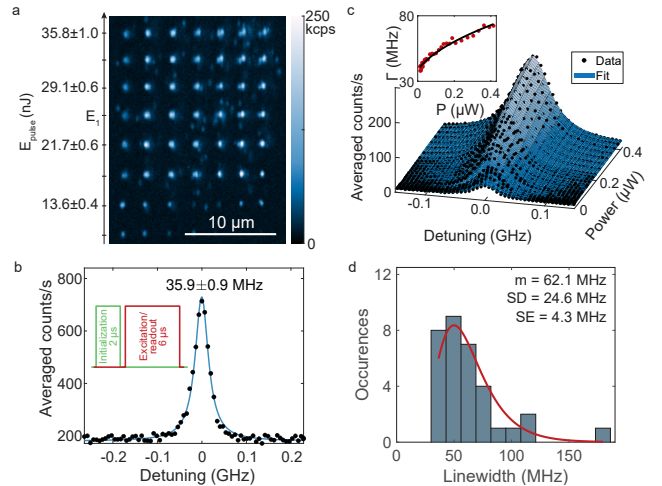


FIG. 1. (a) Array of laser-written NV centers. (b) Optical linewidth measured on a laser-written NV center. Inset: PLE measurement sequence. (c) Resonant power dependence of the ZPL of a laser-written NV. Inset: dependence of the extracted FWHM linewidth on power. (d) Histogram over measured linewidths with a log-normal fit.

cancies combine with nitrogen impurities in the diamond. The method induces minimum damage to the diamond lattice, set only by the size of the laser focus, and the colour centers are formed exclusively from native nitrogen. The laser focus quality, impaired by spherical aberration at the diamond interface, is of extreme importance and requires corrective optics. Initial studies demonstrated laser writing of NV centers using an oil-immersion lens in combination with wavefront correction [9]. We use a different approach employing a standard air objective together with a truncated hemispheric cubic zirconia solid-immersion lens (t-SIL), which not only enables NV center creation with low pulse energies, but also makes it possible to laser-write in close proximity to the diamond surface without inducing graphitization [10]. We use sin-

gle 35 fs pulses with a wavelength centered at 800 nm to create NV center arrays such as the one shown in Fig. 1a.

The dominant mechanism responsible for the vacancy creation can be determined using the Keldysh parameter γ [11]. In our work, $\gamma \ll 1$, which corresponds to a regime where tunneling breakdown is dominant over multi-photon ionization, in contrast to previous work [9]. Further, we are able to create NV centers with pulse energies between 5.8 and 35.8 nJ, which is a remarkably wide energy window compared to previous studies. We propose that this is a key consequence and advantage of NV center laser writing in the tunneling regime.

We characterize the created NV centers through photoluminescence excitation (PLE). The measurement cycle, consisting of an off-resonant charge-state repump pulse followed by resonant excitation and readout, is repeated at a frequency of 100 kHz (inset Fig. 1b). A measured linewidth is shown in Fig. 1b, with a Lorentzian lineshape with a FWHM linewidth of 35.9 ± 0.9 MHz, which is close to the lifetime-limit of 13 MHz.

To disentangle inhomogeneous broadening of the linewidths from power broadening, we perform a systematic study of the linewidth as a function of resonant power. We model the experimentally measured line shapes as a convolution of a Lorentzian spectral diffusion shape and the occupation of the excited level of a driven two-level system. The result of a fit following this model is shown in Fig. 1c. The model gives a value of 25.5 ± 1.2 MHz for the inhomogeneous broadening,

less than 13 MHz above the Fourier-transform-limited linewidth, which indicates an extremely low charge-noise in the NV center surroundings.

Fig. 1d shows a histogram over linewidths measured in a laser-written sample, with a mean as low as 62.1 MHz and a standard deviation of only 24.6 MHz. From the corresponding empirical cumulative distribution function, we can extract a 90.9% chance of measuring a linewidth below the figure of merit of 100 MHz. Considering the regular off-resonant charge-state repump performed during the measurements, one would expect a significant linewidth broadening due to the loading and unloading of vicinal charge traps. The minimal inhomogeneous broadening emphasizes the excellent optical quality and low charge-noise environment of the created NV centers.

III. CONCLUSION

In conclusion, we have demonstrated laser writing of NV centers in diamond using a t-SIL with a wide interval of useful pulse energies. We show high probabilities of measuring inhomogeneously broadened linewidths below 100 MHz, illustrating that laser writing yields an exceptionally high probability of generating narrow-linewidth NV centers compared to standard NV creation methods [4, 7, 8]. We measure record-low charge-noise levels even in the presence of an off-resonant charge-state repump [4, 9, 12], which makes the created NV centers excellent candidates for applications based on spin-photon entanglement.

-
- [1] M. Pompili, S. L. N. Hermans, S. Baier, H. K. C. Beukers, P. C. Humphreys, R. N. Schouten, R. F. L. Vermeulen, M. J. Tiggelman, L. dos Santos Martins, B. Dirkse, et al., *Realization of a multinode quantum network of remote solid-state qubits*, *Science* **372**, 259 (2021).
 - [2] R. J. Barbour, P. A. Dalgarno, A. Curran, K. M. Nowak, H. J. Baker, D. R. Hall, N. G. Stoltz, P. M. Petroff, and R. J. Warburton, *A tunable microcavity*, *J. Appl. Phys.* **110**, 053107 (2011).
 - [3] H. Kaupp, T. Hümmer, M. Mader, B. Schlederer, J. Benedikter, P. Haeusser, H. C. Chang, H. Fedder, T. W. Hänsch, and D. Hunger, *Purcell-enhanced single-photon emission from nitrogen-vacancy centers coupled to a tunable microcavity*, *Phys. Rev. Appl.* **6**, 054010 (2016).
 - [4] Y. Chu, N. P. De Leon, B. J. Shields, B. Hausmann, R. Evans, E. Togan, M. J. Burek, M. Markham, A. Stacey, A. S. Zibrov, et al., *Coherent optical transitions in implanted nitrogen vacancy centers*, *Nano Lett.* **14**, 1982 (2014).
 - [5] E. Janitz, M. Ruf, M. Dimock, A. Bourassa, J. Sankey, and L. Childress, *Fabry-Perot microcavity for diamond-based photonics*, *Phys. Rev. A* **92**, 43844 (2015).
 - [6] D. Riedel, I. Söllner, B. J. Shields, S. Starosielec, P. Appel, E. Neu, P. Maletinsky, and R. J. Warburton, *Deterministic enhancement of coherent photon generation from a nitrogen-vacancy center in ultrapure diamond*, *Phys. Rev. X* **7**, 031040 (2017).
 - [7] S. B. Van Dam, M. Walsh, M. J. Degen, E. Bersin, S. L. Mouradian, A. Galiullin, M. Ruf, M. Ijspeert, T. H. Taminiau, R. Hanson, et al., *Optical coherence of diamond nitrogen-vacancy centers formed by ion implantation and annealing*, *Phys. Rev. B* **99**, 161203 (2019).
 - [8] M. Kasperczyk, J. A. Zuber, J. Kölbl, V. Yurgens, S. Flågan, T. Jakubczyk, B. Shields, R. J. Warburton, and P. Maletinsky, *Statistically modeling optical linewidths of nitrogen vacancy centers in microstructures*, *Phys. Rev. B* **102**, 075312 (2020).
 - [9] Y.-C. Chen, P. S. Salter, S. Knauer, L. Weng, A. C. Frangeskou, C. J. Stephen, S. N. Ishmael, P. R. Dolan, S. Johnson, B. L. Green, et al., *Laser writing of coherent colour centres in diamond*, *Nat. Photonics* **11**, 77 (2017).
 - [10] V. Yurgens, J. A. Zuber, S. Flågan, M. De Luca, B. J. Shields, I. Zardo, P. Maletinsky, R. J. Warburton, and T. Jakubczyk, *Low-charge-noise nitrogen-vacancy centers in diamond created using laser writing with a solid-immersion lens*, *ACS Photonics* **8**, 1726 (2021).
 - [11] L. V. Keldysh, *Ionization in the field of a strong electromagnetic wave*, *J. Exp. Theor. Phys.* **47**, 1945 (1964).
 - [12] M. Ruf, M. Ijspeert, S. Van Dam, N. De Jong, H. Van Den Berg, G. Evers, and R. Hanson, *Optically coherent nitrogen-vacancy centers in micrometer-thin etched diamond membranes*, *Nano Lett.* **19**, 3987 (2019).

Entropy Production and Correlations in the driven Caldeira-Leggett model

Alessandra Colla¹ and Heinz-Peter Breuer^{1,2}

¹*Institute of Physics, University of Freiburg, D-79104 Freiburg, Germany*

²*EUCOR Centre for Quantum Science and Quantum Computing,
University of Freiburg, D-79104 Freiburg, Germany*

The driven Caldeira-Leggett model of quantum Brownian motion, taken with a large but finite number of bath modes, is exactly solvable, and the assumption of a Gaussian initial state leads to an efficient numerical simulation of all desired observables in a wide range of model parameters. This set-up is ideal for the investigation on the proper definition of thermodynamic quantities such as work, heat and entropy production. Here, we illustrate how the presence of a driving force on the system has a non-trivial effect on the conceptual and numerical comparison between the definition of entropy production proposed by Deffner and Lutz and the one from Esposito, Lindenberg and van den Broeck, as well as on the role of three contributing quantities making up the latter.

I. INTRODUCTION

One of the central goals of the theory of open quantum systems is the development of an efficient description of the reduced dynamics of the open system in which the degrees of freedom of the environment have been eliminated¹. While this is very useful in many cases of interest, there can be physically relevant quantities which require knowledge about the total system-environment state and/or the reduced environmental state. Such quantities arise, for example, in the construction of certain expressions for the entropy production in systems coupled to heat baths, or in the study of the role of correlations generated by the system-environment interaction.

To tackle these questions, a possible strategy is to analyze paradigmatic model systems. The Caldeira-Leggett model² of quantum Brownian motion models a central harmonic oscillator (here, driven), representing the open system, which is coupled to a reservoir of harmonic oscillators describing the environment:

$$H = \underbrace{\frac{1}{2}p_0^2 + \frac{1}{2}\omega_0^2 x_0^2 - F(t)x_0}_{H_S} + \underbrace{\sum_{n=1}^N \left(\frac{1}{2}p_n^2 + \frac{1}{2}\omega_n^2 x_n^2 \right)}_{H_E} - \underbrace{x_0 \sum_{n=1}^N \kappa_n x_n}_{H_I} + \underbrace{x_0^2 \sum_{n=1}^N \frac{\kappa_n^2}{2\omega_n^2}}_{V_c}. \quad (1)$$

This is a well-known integrable model which can serve as a suitable ground for testing theories that rely on the knowledge of the dynamics of the system and the environment altogether. Taking a large but finite number of environmental harmonic oscillator modes, the Caldeira-Leggett model can be solved exactly by a transformation to normal modes³ which, together with the assumption of Gaussian initial states, leads to an efficient method for the evaluation of general physical quantities of the total system in a wide range of model parameters such as temperature, system-environment coupling, driving frequency and amplitude. We here review some previous studies which were performed in the case of undriven

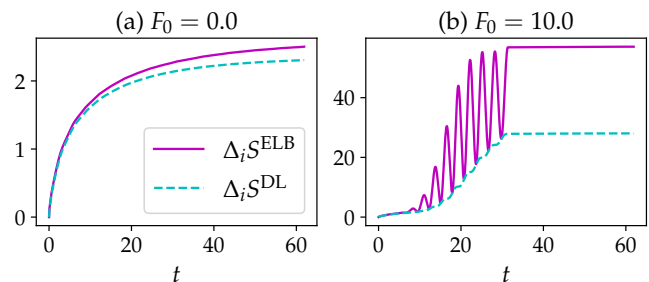


FIG. 1: The two different expressions of entropy production in their convergence limit (high temperature and weak coupling) with $N = 400$, $\gamma = 0.01$ and $T = 10$. When driving is strong (b), they do not converge.

systems, and find that the addition of a driving force has non-trivial consequences on those results.

II. TWO THERMODYNAMIC STUDIES

Two definitions of entropy production

There is no general consensus on how to define proper thermodynamic quantities at a quantum level, especially in the strong coupling regime. Different definitions of work and heat consequently lead to different forms of entropy production. In the “standard approach”⁴, the heat exchange is seen as arising from the dynamic change of the central system Hamiltonian. This leads to the well-known form of the entropy production originally proposed by Spohn^{5,6} and to the later generalization to the driven case by Deffner and Lutz⁷ (DL entropy production):

$$\Delta_i S^{\text{DL}}(t) = S(\rho_S(0) || \rho_S^{\text{eq}}(0)) - S(\rho_S(t) || \rho_S^{\text{eq}}(t)) - \int_0^t ds \text{Tr} \{ \rho_S(s) \partial_s \ln \rho_S^{\text{eq}}(s) \}, \quad (2)$$

where $S(\rho_A || \rho_B)$ denotes the relative entropy of the states ρ_A, ρ_B .

While extensively in use in the weak coupling regime, this expression can become drastically negative at strong coupling. A different proposal for entropy production

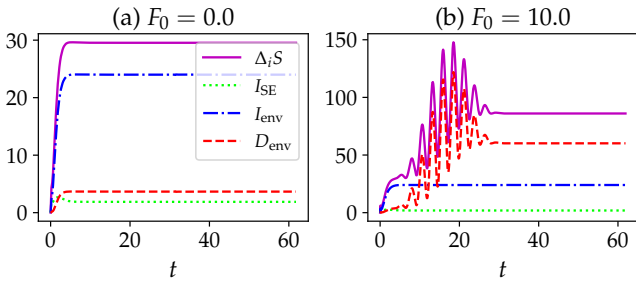


FIG. 2: Time evolution of the ELB entropy production and its three contributions, at $N = 400$, $\gamma = 1$ and $T = 5$. Comparison between undriven and strongly driven case.

has been developed by Esposito, Lindenberg and van den Broeck⁸ (ELB entropy production), where the heat exchange is associated to the change of the mean bath energy. This corresponds to also taking into account the contribution coming from the interaction. Imposing then an uncorrelated initial state with the bath in thermal equilibrium leads to an expression for entropy production which is positive at all times:

$$\Delta_i S^{\text{ELB}}(t) = S(\rho_{SE}(t) || \rho_S(t) \otimes \rho_E^{\text{eq}}). \quad (3)$$

From the origin of the two definitions (2) and (3), one can see how the difference between them should vanish in the limit of some coupling strength going to zero. A comparison between the two different approaches has been already performed for the undriven Caldeira-Leggett model⁹, confirming their compatibility in the small coupling regime. On the contrary, we find that the two definitions are instead incompatible when driving is present on the central oscillator (Fig. 1), which points

at possible fundamental discrepancies between the two approaches¹⁰.

Contributions to the ELB entropy production

The ELB entropy production (3) can be split into three non-negative parts representing the mutual information between system and environment, the mutual information describing the intra-environmental correlations, and the sum of the distances of the individual bath modes from their initial state:

$$\Delta_i S^{\text{ELB}}(t) = I_{SE}(t) + I_{\text{env}}(t) + D_{\text{env}}(t). \quad (4)$$

The relevance of each of these quantities was discussed recently¹¹ for a quantum dot coupled to fermionic baths, showcasing the importance of the intra-environment correlations as the main contribution to entropy production. However, in the Caldeira-Leggett model these need not provide the dominant contribution¹⁰. Depending on the coupling-temperature parameter regime, each of the three quantities may represent the most contributing part to entropy production. Moreover, driving the central oscillator leads to a drastic change of the relative size of the various contributions: especially for strong and resonant driving, the distance of the environment modes increases with respect to its non-driven value and has the possibility to triumph over the intra-environment mutual information as the dominant contribution of entropy production (See Fig. 2).

Acknowledgments

This project has received funding from the European Union's Framework Programme for Research and Innovation Horizon 2020 (2014-2020) under the Marie Skłodowska-Curie Grant Agreement No. 847471.

¹ H.-P. Breuer and F. Petruccione, *The Theory of Open Quantum Systems* (Oxford University Press, Oxford, 2002).

² A. Caldeira and A. Leggett, *Quantum tunnelling in a dissipative system*, Annals of Physics **149**, 374 (1983), ISSN 0003-4916.

³ P. Ullersma, *An exactly solvable model for brownian motion: I. derivation of the langevin equation*, Physica **32**, 27 (1966), ISSN 0031-8914.

⁴ G. T. Landi and M. Paternostro, *Irreversible entropy production, from quantum to classical* (2020), 2009.07668.

⁵ H. Spohn, *Entropy production for quantum dynamical semigroups*, Journal of Mathematical Physics **19**, 1227 (1978).

⁶ H. Spohn and J. L. Lebowitz, *Irreversible Thermodynamics for Quantum Systems Weakly Coupled to Thermal Reservoirs* (John Wiley & Sons, Ltd, 1978), pp. 109–142, ISBN

9780470142578.

⁷ S. Deffner and E. Lutz, *Nonequilibrium entropy production for open quantum systems*, Phys. Rev. Lett. **107**, 140404 (2011).

⁸ M. Esposito, K. Lindenberg, and C. V. den Broeck, *Entropy production as correlation between system and reservoir*, New Journal of Physics **12**, 013013 (2010).

⁹ L. Pucci, M. Esposito, and L. Peliti, *Entropy production in quantum Brownian motion*, Journal of Statistical Mechanics: Theory and Experiment **2013**, P04005 (2013).

¹⁰ A. Colla and H.-P. Breuer, *Entropy production and the role of correlations in quantum brownian motion* (2021), 2108.02599.

¹¹ K. Ptaszyński and M. Esposito, *Entropy production in open systems: The predominant role of intra-environment correlations*, Phys. Rev. Lett. **123**, 200603 (2019).

A quantum dot in a microcavity as a diode for single-photons

Nadia Olympia Antoniadis,¹ Alisa Javadi,¹ Natasha Tomm,¹ Rüdiger Schott,² Sascha René Valentin,² Andreas Dirk Wieck,² Arne Ludwig,² and Richard John Warburton¹

¹*Department of Physics, University of Basel, Klingelbergstrasse 82, CH-4056 Basel, Switzerland*

²*Lehrstuhl für Angewandte Festkörperphysik, Ruhr-Universität Bochum, D-44780 Bochum, Germany*

Light’s most fundamental properties, reciprocity and linearity, can simultaneously be broken via a coherent light-matter interaction. Here, we use a semiconductor quantum dot in a tunable microcavity to demonstrate highly non-reciprocal (with an isolation of 10.7 dB) and non-linear (at low powers in the order of 100 pW) transport of single-photons. The open nature of the microcavity enables us to tune the coupling strength β between the cavity and the quantum dot to the critical point and, hence, realise a diode for single-photons.

I. INTRODUCTION

Reciprocity and linearity are the most basic and intuitive properties of light. While breaking these properties within the same system is of interest from the fundamental research point of view, non-reciprocal and non-linear elements also have a unique role in optical quantum information processing. A broad range of non-reciprocal devices, such as diodes and circulators, already exist for electrons. Optical circuits still lack a fully functioning counterpart to these elements. As the photonic quantum technologies develop further, the need for such non-reciprocal and non-linear devices at the single-photon regime emanates. Furthermore, scalability is very important for new quantum circuits, making devices on the single-emitter level excellent candidates for a variety of applications.

II. OPERATION PRINCIPLE OF THE DIODE

Non-reciprocity, the dependence of transmission on the propagation direction, can be achieved by chirally coupling photons to a quantum dot in a one-sided, polarisation-degenerate cavity [1, 2], as shown in Fig. 1. The transmission through a chiral system is given by [3, 4]

$$T = |1 - 2\beta|^2, \quad (1)$$

where β is the coupling strength between the cavity and the quantum dot. We can tune the system to the critical point, $\beta = 0.5$, by moving the quantum dot’s position with respect to the cavity mode. In this critical coupling regime, light propagating in the backward direction (port 2 to port 1) will be polarisation-matched to the transition of the quantum dot and interact according to Eq. 1, and therefore light will be lost in the cavity. On the other hand, light propagating in the forward direction (port 1 to port 2) will not be polarisation-matched to the transition of the dipole and be transmitted through the “diode” unchanged. Essential here are the optical components of the microscope head, allowing full control over the polarisation at the input of the cavity and the collected light. The second requirement for a diode, non-linearity in photon transport, is naturally achieved through the “atom-like” energy structure of the quantum dot.

III. EXPERIMENTAL RESULTS

In our experiment we measure the transmission of light in the both propagation directions as a function of gate voltage (V_g) applied to the quantum dot. Figure 2a shows how the the propagation in backward direction is suppressed by a factor of 11.9 compared to the forward direction (10.7 dB). This is the highest non-reciprocal response recorded on a single quantum emitter in the solid state. Furthermore, a non-linearity at the single-photon

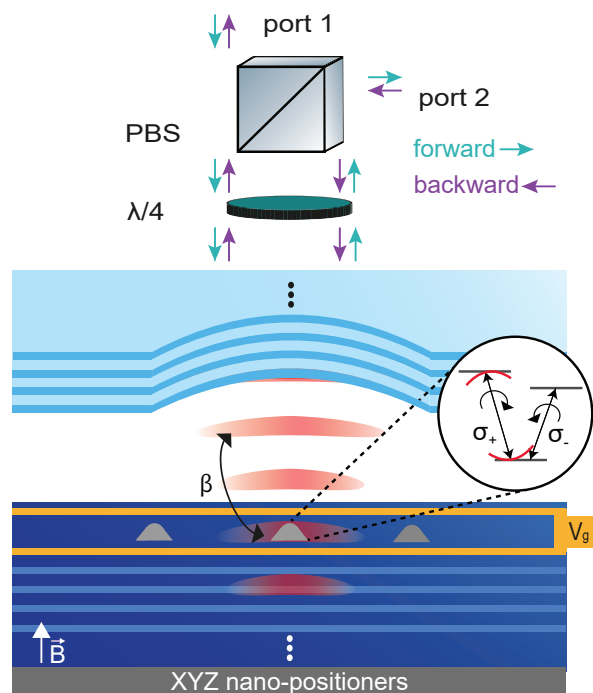


FIG. 1. **Schematic of the diode.** A circular dipole is embedded in a tunable, open microcavity. The optical setup consists of a polarising beam-splitter (PBS) and a quarter-wave plate ($\lambda/2$). These optical elements allow control over the polarisation of the photons travelling through the cavity. A magnetic field splits the two transitions of the quantum dot enough, that only one of them couples to the cavity with an efficiency β . The purple and turquoise arrows define the two propagation directions of the system.

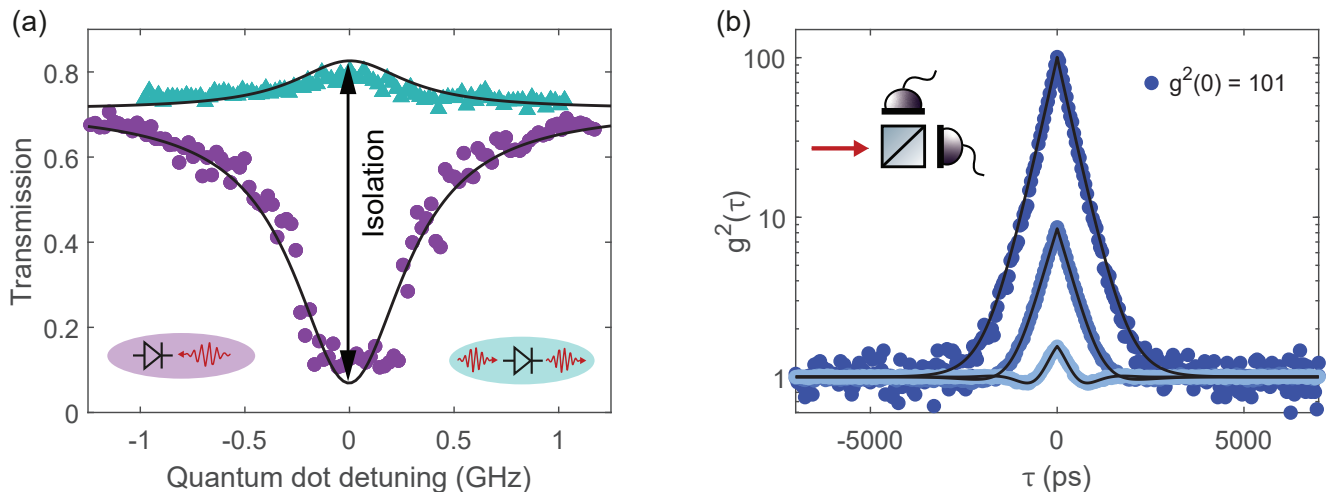


FIG. 2. **(a)** The transmission through the “diode” for forward (turquoise) and backward (purple) propagation. Transmission at resonance shows a strong non-reciprocal behaviour shown here at an optical power of 2.1 pW with an isolation of 10.7 dB. The maximum transmission is limited by the residual non-degeneracy of the cavity to 0.7. **(b)** Autocorrelation function $g^{(2)}(\tau)$ of the transmitted light in backward direction for three different powers. At lowest optical power (2.1 pW) a bunching of 101 is observed. For increasing power bunching decreases exponentially.

level with a saturation power of 213 pW is observed. The non-linearity is revealed in a profound change in the statistics of the photons transmitted by the diode (see $g^{(2)}(\tau)$ in Fig. 2b), from highly bunched ($g^{(2)}(0) = 101$) at low power, to coherent-state like ($g^{(2)}(0) = 1$) at “high” power. This statistical behaviour can be explained by the single-photon components of a coherent laser interacting with the emitter, i.e. being lost, while higher photon-number components are detected in bunches. These results demonstrate that our system can be operated as a diode for single-photons.

IV. CONCLUSION AND OUTLOOK

The reported experiments reveal strong non-reciprocal and non-linear transport of single-photons through a quantum emitter in a microcavity, revamping the fundamental transport characteristics of electromagnetic fields. We show how the tunable nature of the open microcavity enables its implementation as a diode for single-photons,

surpassing any other reported quantum system with respect to non-reciprocal optical transmission. We can further foresee a range of applications in quantum optics, e.g. optical switches, by exploiting the spin-state of a charge-carrier in our quantum dots. The strong bunching of photons in the transmission of the system is a manifestation of bound-state formation between photons, and may find application in realising exotic photonic states. Moreover, an optimised design of the cavity can be operated at lower wavelengths where very high β -factors are achievable. Such a device would be ideal for non-linear phase shifts, allowing the implementation of universal phase-gates for quantum computation [5].

ACKNOWLEDGMENTS

We acknowledge financial support from Swiss National Science Foundation project 200020_175748, NCCR QSIT and Horizon-2020 FET-Open Project QCLUSTER. AJ acknowledges support from the European Unions Horizon 2020 research and innovation program under the Marie Skłodowska-Curie grant agreement No. 840453 (HiFig).

-
- [1] N. Tomm, A. Javadi, N. O. Antoniadis, D. Najer, M. C. Löbl, A. R. Korsch, R. Schott, S. R. Valentin, A. D. Wieck, A. Ludwig, et al., *A bright and fast source of coherent single photons*, Nat. Nanotechnol. **16**, 399 (2021).
 [2] D. Najer, I. Söllner, P. Sekatski, V. Dolique, M. C. Löbl, D. Riedel, R. Schott, S. Starsielec, S. R. Valentin, A. D. Wieck, et al., *A gated quantum dot strongly coupled to an optical microcavity*, Nature **575**, 622 (2019).
 [3] P. Lodahl, S. Mahmoodian, S. Stobbe, A. Rauschenbeutel, P. Schneeweiss, J. Volz, H. Pichler, and P. Zoller, *Chiral*

- quantum optics*, Nature **541**, 473 (2017).
 [4] I. Söllner, S. Mahmoodian, S. L. Hansen, L. Midolo, A. Javadi, G. Kiršanskė, T. Pregolato, H. El-Ella, E. H. Lee, J. D. Song, et al., *Deterministic photon-emitter coupling in chiral photonic circuits*, Nat. Nanotechnol. **10**, 775 (2015).
 [5] T. Ralph, I. Söllner, S. Mahmoodian, A. White, and P. Lodahl, *Photon Sorting, Efficient Bell Measurements, and a Deterministic Controlled-Z Gate Using a Passive Two-Level Nonlinearity*, Phys. Rev. Lett. **114**, 173603 (2015).

Quantum mean-square predictors of work

Marcelo Janovitch^{1,2} and Gabriel T. Landi^{2,*}

¹*Department of Physics, University of Basel, CH-4056 Basel, Switzerland*[†]

²*Instituto de Física da Universidade de São Paulo, 05314-970 São Paulo, Brazil.*

In initially coherent systems, it is impossible to measure work without destroying coherence. Thus, work distributions either disregard coherence or need to allow for non-operational prescriptions. We give a partial solution to this conundrum by deriving a predictor of work; a quantity that gives optimal information of work based on heat measurements, thereby leaving coherence untouched. We illustrate our findings through the three-level engine of Scovil & Schulz-DuBois, which operates in a coherent limit-cycle.

I. THERMODYNAMICS: FROM CLASSICAL TO QUANTUM

The advancement of technology in the last few centuries has been driven by the construction of engines of all sort. Be them vapor engines or top-notch laser technologies, at the core of their designs lies efficiency. And thermodynamics is the physical theory of efficiency.

In spirit, heat encodes the energy flux from abundant and usually entropic resources, while work entails the desired task to be performed. The simplest heat engine (S) is supplied by a hot (H) and a cold (C) bath with heats Q_H, Q_C . If we wait long enough, so the internal energy of S no longer changes, such engine establishes a steady conversion of heat into work,

$$\langle Q_H \rangle + \langle Q_C \rangle = \langle W \rangle. \quad (1)$$

This is the the first law of thermodynamics once S is in its steady-state. In Carnot's statement, the second law constrains efficiency of the conversion of heat into work, $\eta = W/Q_H$,

$$\eta = 1 - \frac{T_C}{T_H} + \frac{T_C}{\langle Q_H \rangle} \langle \Sigma \rangle, \quad (2)$$

where T_H, T_C are temperatures of hot and cold bath, and $\langle \Sigma \rangle$ is the entropy production. $\langle \Sigma \rangle$ is always non-negative and quantifies how irreversible a process is. It guarantees that any process which involves heat will deviate from optimal efficiency, $\eta_{\text{Carnot}} = 1 - T_C/T_H$ ¹.

Fluctuations in classical systems

Thermodynamics was yet conceived as a phenomenological theory and holds only at the macroscopic scale. For small systems, one has to allow heat and work to fluctuate in order to reconcile them with the microscopic physics. For non-equilibrium classical systems, the probability distributions of thermodynamic observables, say $P(Q), P(W), P(\Sigma)$, were shown to satisfy generalizations of the laws of thermodynamics, the so-called fluctuation theorems (FTs). For example, Crooks' FT² states that

$$\frac{P(\Sigma)}{\tilde{P}(-\Sigma)} = e^{\Sigma}, \quad (3)$$

where $\tilde{P}(\Sigma)$ is the probability of the reverse process. Hence, it upgrades the second law to allow for negative (stochastic) entropy production, yet with exponentially less probability than its positive counterparts.

Quantum Thermodynamics

The first evidence of the validity of thermodynamics in quantum systems was given by Scovil and Schulz-DuBois in 1959³, who argued that the efficiency of a three-level maser was constrained by Carnot's bound. However, at the time, quantum technologies were far from reach.

With the control of quantum system achieved in the present days, it is useful to extend thermodynamics to the widest range of quantum systems in order to develop efficient quantum devices. In particular, understanding how to entail genuine quantum features, such as coherence, is one of the central challenges of quantum thermodynamics. With the tools of quantum information and open quantum systems, the field was already successful in extending the first and second law of thermodynamics for a broad range of quantum systems¹. But, in general, only at the level of averages.

The impasse of quantum fluctuations in thermodynamics

Naturally, in the quantum scale fluctuations are even more prominent than in classical systems. Hence, averages are often not a satisfactory description. The quantum realm yet presents severe difficulties associated to the probabilistic description of thermodynamic observables. First, fluctuations stemming from classical ignorance are intertwined with the inherent probabilistic nature of quantum theory. Second, such probabilities demand the quantum description of measurement, which often erases the precise quantum features we try to capture in thermodynamic processes.

This difficulty can be illustrated as follows. Let ρ_S describe a quantum system of interest and H_S its Hamiltonian. Suppose that it is in contact with an environment E , with Hamiltonian H_E , prepared in a Gibbs state $\rho_E^{\text{th}} = \exp\{-\beta H_E\}/Z_E$. At $t = 0$ they are initialized

as $\rho_{SE} = \rho_S \otimes \rho_E^{\text{th}}$ evolve until $t = \tau$ through $U_\tau = \exp\{-i\tau(H_S + H_E + H_{SE})\}$ to a state $\rho'_{SE} = U_\tau \rho_{SE} U_\tau^\dagger$. To obtain the distribution of heat exchanged in this time-interval, $P(Q)$, one often resorts to the *two-point measurement* (TPM) protocol⁴: Measure E in its energy eigenbasis before evolution, with outcome ϵ_μ ; evolve through U_τ ; and again measure the environment's energy, $\epsilon_{\mu'}$. Their difference is then associated to heat, $Q = \epsilon_{\mu'} - \epsilon_\mu$, and its probability distribution writes

$$P(Q) = \sum_{\mu, \mu'} \delta(Q - (\epsilon_{\mu'} - \epsilon_\mu)) P(\mu', \mu), \quad (4)$$

where δ is the Kroenecker delta and $P(\mu', \mu)$ is given by Born's rule

$$P(\mu', \mu) = \text{Tr}(U_\tau^\dagger \Pi_{\mu'} U_\tau \Pi_\mu \rho_{SE}), \quad (5)$$

where $\Pi_\mu = |\mu\rangle\langle\mu|$ are environment projectors in the H_E eigenbasis. The TPM protocol employed above has the correct average, $\sum_Q Q P(Q) = \text{Tr}\{(H_E(\rho'_{SE} - \rho_{SE}))\}$. Further, it has been successful in providing distributions which also satisfy FTs. However, it has a serious drawback: it only works for initially energy-incoherent systems. That is, in this case, because $[\rho_E^{\text{th}}, H_E] = 0$. If we try to do the same to define the distribution of internal energy change, $P(\delta U)$, this would only work if $[\rho_S, H_S] = 0$ — in the contrary, we attain the wrong average. The reason is that, at the first measurement, we'd collapse the system in an energy eigenstate and coherence is lost. Upon averaging, we do not restore it. If we were then to define stochastic work $W = Q + \delta U$, its probabilities, $P(W)$, inherit the same illness.

The conundrum of quantum work distributions has been crystallized in a no-go theorem⁵. In practice, the theorem states that every $P(W)$ which (i) agrees with the TPM for incoherent systems; and (ii) attains the correct average for any initial state; is fated either to negative probabilities or operational drawbacks (e.g. quan-

tum Bayesian networks⁶). Hence, TPM protocols cannot account for coherent processes.

II. ACCESSIBLE WORK FLUCTUATIONS

Our contribution to this puzzle is, at the cost of some error, predict work fluctuations indirectly. That is, we perform only measurements which do not lead to decoherence. In particular, we use the quantum Bayesian network formalism⁶ to provide a distribution $P(W, Q)$ and, from it, we derive the best possible predictor of work given only heat measurements, the so-called *quantum mean-square predictor of work*⁷. As mentioned, heat can be measured non-invasibly, in accordance with the TPM performed *in the environment*.

Formally, we find the function of heats which minimizes the mean-square error relative to $P(Q, W)$. This process is common in statistical prediction⁸, whenever one can provide a theoretical model $P(Q, W)$, but only partial data of the full distribution is available.

Our result provides an operational definition of fluctuating work in coherent systems. We illustrate it through the heat engine of Scovil & Schulz-DuBois³. This device converts heat into work, in the form of coherent light, in which coherence within the qutrit is crucial for the coherent light output. From the jump unravelings of the Lindblad master equation, we then predict work within each quantum jump encompassing heat.

Acknowledgments

M. J. would like to thank the University of Basel, the QUSTEC programme and the financial support from the Brazilian funding agency CAPES. The QUSTEC programme has received funding from the European Union's Horizon 2020 research and innovation programme under the Marie Skłodowska-Curie grant agreement number 84747.

* Electronic address: gtlandi@gmail.com

† Electronic address: m.janovitch@unibas.ch

¹ G. T. Landi and M. Paternostro, *Irreversible entropy production, from quantum to classical*, arXiv pp. 1–62 (2020), ISSN 23318422, 2009.07668, URL <http://arxiv.org/abs/2009.07668>.

² G. E. Crooks, *Journal of Statistical Physics, Volume 90, Numbers 5-6 - SpringerLink*, Journal of Statistical Physics **90**, 1481 (1998).

³ H. E. D. Scovil and E. O. Schulz-DuBois, *Three-Level Masers as Heat Engines*, Physical Review Letters **2**, 262 (1959), ISSN 0031-9007, URL <https://link.aps.org/doi/10.1103/PhysRevLett.2.262>.

⁴ P. Talkner, E. Lutz, and P. Hänggi, *Fluctuation theorems: Work is not an observable*, Physical Review E - Statistical, Nonlinear, and Soft Matter Physics **75**, 050102 (2007), ISSN 15502376, 0703189, URL <https://link.aps.org/doi/10.1103/PhysRevE.75.050102>.

[org/doi/10.1103/PhysRevE.75.050102](https://doi.org/10.1103/PhysRevE.75.050102).

⁵ M. Perarnau-Llobet, E. Bäumer, K. V. Hovhannisyan, M. Huber, and A. Acin, *No-Go Theorem for the Characterization of Work Fluctuations in Coherent Quantum Systems*, Physical Review Letters **118**, 1 (2017), ISSN 10797114, 1606.08368.

⁶ K. Micadei, G. T. Landi, and E. Lutz, *Quantum Fluctuation Theorems beyond Two-Point Measurements*, Physical Review Letters **124**, 90602 (2020), ISSN 10797114, 1909.12189, URL <https://doi.org/10.1103/PhysRevLett.124.090602>.

⁷ M. Janovitch and G. T. Landi, *Quantum mean-square predictors of work* (2021), 2104.07132, URL <http://arxiv.org/abs/2104.07132>.

⁸ P. J. Bickel and K. A. Doksum, *Mathematical Statistics: Basic Ideas and Selected Topics*, **1**, 412 (1977), ISSN 0040-1706.

Theory of Hole Spin Qubits in Ge Nanowire Quantum Dots: Effects of Orbital Magnetic Field, Anisotropies, and Strain

Christoph Adelsberger,¹ Mónica Benito,^{1,2} Stefano Bosco,¹ Jelena Klinovaja,¹ and Daniel Loss¹

¹*Department of Physics, University of Basel, Klingelbergstrasse 82, 4056 Basel, Switzerland*

²*Institute of Physics, University of Augsburg, 86135 Augsburg, Germany*

Hole spin qubits in nanowires (NW) are a promising platform for quantum information processing because of the strong spin-orbit interaction (SOI). We present analytical results for the SOI in Ge semiconductors. At the magnetic field used for spin qubit operation, orbital effects can crucially influence the qubit response. We study holes in Ge NWs under the influence of electric and magnetic fields applied perpendicularly to the device and include orbital effects exactly. These effects lead to a strong renormalization of the g -factor. We find a sweet-spot of the NW g -factor where charge noise is strongly suppressed and present an effective low-energy model that captures the dependence of the SOI on the electromagnetic fields. Considering a quantum dot (QD), we demonstrate that the NW g -factor sweet spot is retained in the QD. Our calculations reveal that this sweet spot can be designed to coincide with the maximum of the SOI, yielding highly coherent qubits with large Rabi frequencies.

I. INTRODUCTION

A crucial step on the way to quantum computing with spin qubits defined on quantum dots (QD)¹ is to make them scalable. As a promising platform to achieve that goal hole spins in semiconductors like germanium (Ge) and silicon (Si) have attracted much attention lately because they naturally enable strong SOI in contrast to electron systems^{2,3}. The strong SOI allows for electrical control. Another great advantage of hole devices is their tunable response to the hyperfine interactions⁴⁻⁶.

The effective low-dimensional physics of hole systems depends strongly on the details of the confinement, the material strain and the applied electromagnetic fields^{2,7-10}. The strongest SOI enabling the fastest and most power efficient operations are achieved in quasi one-dimensional structures, which can be fabricated in different ways^{2,9}.

In order to define qubits, a magnetic field is necessary to energetically split different spin states. When a magnetic field is applied perpendicular to the axis of the one-dimensional structure, e.g. a nanowire (NW), the orbital effects can strongly influence the performance of the qubit. In two-dimensional heterostructures with the magnetic field applied in-plane, the influence of these orbital effects strongly depends on the width of the two-dimensional electron or hole gas. In this case one can observe a correction of the g -factor¹¹ and a renormalization of the effective mass¹².

In this work we analyze the SOI, effective g -factor, and effective masses of the lowest-energy states in NWs with rectangular cross-section. We compare different designs by also fully accounting for the orbital effects in a moderate magnetic and electric field. Interestingly, we predict that, at the point with the largest SOI, the g -factor is in a sweet spot at which the charge noise is negligible. Similar sweet spots have been predicted in Ref.¹³ in hole systems possessing a SOI that is cubic in momentum and showing in EDSR experiments a Rabi frequency two orders of magnitude weaker than elongated QDs⁹. We further find

that the effective masses of the low-energy holes depend strongly on both electric and magnetic fields and become spin-dependent when a B field is applied.

II. MODEL FOR THE NANOWIRE

The model we employ for the analysis of low-energy holes in Ge reads

$$H = H_{\text{LK}} + H_Z + H_E + V, \quad (1)$$

where H_{LK} is the Luttinger-Kohn (LK) Hamiltonian^{2,14} describing the spin-3/2 holes near the Γ point. Using the kinematic momentum allows us to include orbital effects to our model. In addition, H_Z is the Zeeman Hamiltonian describing the coupling of the spin to an external magnetic field B . The term H_E includes the electrostatic energy produced by an externally applied gate potential. We assume an electric and magnetic field perpendicular to the NW. In order to define a NW with rectangular cross-section, we consider a hard-wall (HW) confinement potential V .

III. DIRECT RASHBA SPIN-ORBIT COUPLING

Strong heavy-hole-light-hole mixing terms in the LK Hamiltonian in the presence of an inversion symmetry breaking electric field E lead to a strong direct Rashba SOI^{2,15}. By assuming an infinitely long wire and choosing the Landau gauge such that the translational invariance along the NW is preserved we can calculate the SOI analytically. We predict that the maximum SOI is achieved for a rectangular cross-section in agreement with the result for squeezed QDs⁹. The SOI can effectively be described by the simple term $H_{so} = \alpha_{so} k_y \sigma_x$. Under the assumption of a weak electric field without including orbital effects and if the difference of confinement energies is small compared to the Zeeman term we find for a square NW with side length L the SO term $\alpha_{so} = 0.094eEL^2$.

Including orbital effects exactly, we see that the SOI decreases with increasing magnetic field when the magnetic length becomes comparable to the NW side length.

IV. EFFECTIVE LOW-ENERGY ONE-DIMENSIONAL MODEL

From second order perturbation theory we obtain an effective model Hamiltonian up to second order in momentum along the NW k^2

$$H_{\text{eff}} = \frac{\hbar^2}{2\bar{m}}k^2 - \beta\sigma_zk^2 + g\frac{\mu_B B}{2}\sigma_z + \alpha_{so}k\sigma_x \quad (2)$$

with the average heavy-hole–light-hole effective mass \bar{m} , a spin-dependent mass-like term β the effective g -factor g , the Bohr magneton μ_B and the effective SOI α_{so} . Following a numerical approach using a discrete basis fulfilling the HW boundary conditions shows that our analytical results for the SOI coincide excellently with the numerics for small E . For the effective g -factor we find a strong renormalization due to orbital effects even at small magnetic field. Moreover, the g -factor is large ($g > 5$) and has a sweet spot as a function of the electric field where the effect of charge noise is drastically reduced. Due to time-reversal symmetry $\beta = 0$ at $B = 0$ and for small magnetic field β is linear in E .

V. QUANTUM DOT PHYSICS

Confining the NW harmonically via gates to a QD and driving the QD we show that it is still possible to have

a QD g -factor sweet spot and that its position can be moved to the same electric field as the maximum SOI allowing for ultrafast gates at low power.

VI. OUTLOOK

In our work we further include strain induced by a Si shell around the Ge NW and show that it allows for larger SOI at the cost of a larger electric field and it increases the g -factor. Strain is an important parameter to tune the position of the QD g -factor. Furthermore, we compare our results for a NW with rectangularly to one with circular cross-section and to a harmonically confined one-dimensional channel in a SiGe/Ge/SiGe heterostructure. We see that at strong electric field the 1D channel resembles a rectangular cross-section NW because the wave function is compressed at the top of the Ge layer and the parabolic confinement is less relevant. An analysis of different NW growth directions shows that our model is valid for most of the relevant growth directions. The g -factor depends on the growth direction and orbital effects can influence this dependence drastically.

Our QD analysis reveals for certain electric and magnetic fields a flat band ground state that is dominated by a k^4 -term. This interesting point could open up the possibility of investigating strongly correlated systems.

Acknowledgments

We would like to thank Christoph Kloeffel for useful discussions and comments. This work is supported by the Swiss National Science Foundation and NCCR SPIN. M.B. acknowledges support by the Georg H. Endress Foundation.

-
- ¹ D. Loss and D. P. DiVincenzo, *Quantum computation with quantum dots*, Physical Review A **57**, 120 (1998).
 - ² C. Kloeffel, M. J. Rančić, and D. Loss, *Direct rashba spin-orbit interaction in si and ge nanowires with different growth directions*, Physical Review B **97**, 235422 (2018).
 - ³ F. N. M. Froning, M. J. Rančić, B. Hetényi, S. Bosco, M. K. Rehmann, A. Li, E. P. A. M. Bakkers, F. A. Zwambag, D. Loss, D. M. Zumbühl, et al., *Strong spin-orbit interaction and g -factor renormalization of hole spins in ge/si nanowire quantum dots*, Physical Review Research **3**, 013081 (2021).
 - ⁴ J. Fischer and D. Loss, *Hybridization and spin decoherence in heavy-hole quantum dots*, Physical Review Letters **105**, 266603 (2010).
 - ⁵ F. Maier and D. Loss, *Effect of strain on hyperfine-induced hole-spin decoherence in quantum dots*, Physical Review B **85**, 195323 (2012).
 - ⁶ J. H. Prechtel, A. V. Kuhlmann, J. Houel, A. Ludwig, S. R. Valentin, A. D. Wieck, and R. J. Warburton, *Decoupling a hole spin qubit from the nuclear spins*, Nature Materials **15**, 981 (2016).
 - ⁷ D. V. Bulaev and D. Loss, *Spin relaxation and decoherence of holes in quantum dots*, Physical Review Letters **95**, 076805 (2005).
 - ⁸ D. V. Bulaev and D. Loss, *Electric dipole spin resonance for heavy holes in quantum dots*, Physical Review Letters

- 98**, 097202 (2007).
- ⁹ S. Bosco, M. Benito, C. Adelsberger, and D. Loss, *Squeezed hole spin qubits in ge quantum dots with ultrafast gates at low power*, arXiv preprint (2021), arXiv:2103.16724.
- ¹⁰ P. Philippopoulos, S. Chesi, D. Culcer, and W. A. Coish, *Pseudospin-electric coupling for holes beyond the envelope-function approximation*, Physical Review B **102**, 075310 (2020).
- ¹¹ P. Stano, C.-H. Hsu, M. Serina, L. C. Camenzind, D. M. Zumbühl, and D. Loss, *g -factor of electrons in gate-defined quantum dots in a strong in-plane magnetic field*, Physical Review B **98**, 195314 (2018).
- ¹² P. Stano, C.-H. Hsu, L. C. Camenzind, L. Yu, D. Zumbühl, and D. Loss, *Orbital effects of a strong in-plane magnetic field on a gate-defined quantum dot*, Physical Review B **99**, 085308 (2019).
- ¹³ Z. Wang, E. Marcellina, A. R. Hamilton, J. H. Cullen, S. Rogge, J. Salfi, and D. Culcer, *Optimal operation points for ultrafast, highly coherent ge hole spin-orbit qubits*, npj Quantum Information **7**, 54 (2021).
- ¹⁴ J. M. Luttinger and W. Kohn, *Motion of electrons and holes in perturbed periodic fields*, Physical Review **97**, 869 (1955).
- ¹⁵ C. Kloeffel, M. Trif, and D. Loss, *Strong spin-orbit interaction and helical hole states in Ge/Si nanowires*, Physical Review B **84**, 195314 (2011).

Optimization of entanglement generation and state protection using Rydberg atoms

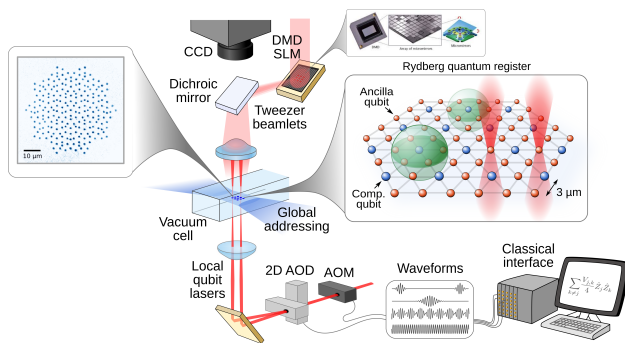
M.Morgado,¹ L.Chang,¹ and S.Whitlock¹

¹CESQ & Institut de Science et d'Ingénierie Supramoléculaires (ISIS, UMR7006), University of Strasbourg and CNRS

Quantum simulators based on Rydberg atoms generated from arrays of optically trapped atoms have emerged as an attractive platform for digital quantum simulation. We aim to explore and develop features regarding coherent control of platforms based on ³⁹K alkali atoms, thanks to recent upgrades in our Rydberg excitation lasers and the integration of a new pulse-shaped microwave addressing to our experiment. These features are important for show coherence in different Rydberg qubit encoding.

Abstract

Entanglement is an important resource for quantum algorithms within quantum information processing, which relies on the capability of using a large number of entangled qubits¹. In the same sense, digital quantum simulations using full programmable operations have a strong interest in how entanglement can play a key role in the study of the behaviour and states of matter².



Different states of matter even in the presence of dissipation mechanisms have been demonstrated using Rydberg atoms³. To investigate controllable quantum dynamics and entanglement generation at the University of Strasbourg, we have recently upgraded our quantum simulator experiment with a characterized and fully pro-

grammable 40GHz bandwidth microwave system to address different Rydberg states. Qubits are encoded in nS and nP excited states of atomic ensembles of Potassium-39 with a qubit frequency of 20GHz and lifetimes of $T_1 \approx 200\mu s$. Here we defined an rr-qubit encoding with coherence times of $T_2^* \approx 6\mu s$, using optimized 200MHz bandwidth protocols for: Rabi and Ramsey sequences that are affected by different mechanisms of noise and decoherence attributed to interactions and hardware synchronization. With this qubit encoding we aim to create an entangled quantum register in large arrays of micro-ensembles⁴ whose state will be self-protected to decoherence using IQ-protocols, optimal timing and hardware-aware pulse-shaping as proof-of-principles of high-fidelity Rydberg quantum gates⁵.

Acknowledgments

This work is supported by the 'Investissements d'Avenir' programme through the Excellence Initiative of the University of Strasbourg (IdEx) and the University of Strasbourg Institute for Advanced Study (USIAS). M.M acknowledges the French National Research Agency (ANR) through the Programme d'Investissement d'Avenir under contract ANR17-EURE-0024 and QUSTEC funding from the European Union's Horizon 2020 research and innovation programme under the Marie Skłodowska-Curie grant agreement No. 847471.

¹ D. Bruß and C. Macchiavello, *Multipartite entanglement in quantum algorithms*, Physical Review A **83**, 052313 (2011).
² A. Browaeys and T. Lahaye, *Many-body physics with individually controlled rydberg atoms*, Nature Physics **16**, 132 (2020).
³ S. Ebadi, T. T. Wang, H. Levine, A. Keesling, G. Semeghini, A. Omran, D. Bluvstein, R. Samajdar, H. Pichler, W. W. Ho, et al., *Quantum phases of matter on a 256-atom programmable quantum simulator*, Nature **595**, 227 (2021).

⁴ Y. Wang, S. Shevate, T. M. Wintermantel, M. Morgado, G. Lochead, and S. Whitlock, *Preparation of hundreds of microscopic atomic ensembles in optical tweezer arrays*, npj Quantum Information **6**, 1 (2020).
⁵ M. Morgado and S. Whitlock, *Quantum simulation and computing with rydberg-interacting qubits*, AVS Quantum Science **3**, 023501 (2021).

Electronic Correlations and Nematic Fluctuations in $\text{Fe}_{1+y}\text{Se}_{0.5}\text{Te}_{0.5}$

Anmol Shukla, Liran Wang, Frédéric Hardy, Kristin Willa, A. A. Haghhighrad, Thomas Wolf, Michael Merz, Christoph Meingast¹

¹*Institute for Quantum Materials and Technologies,
Karlsruhe Institute of Technology, PO Box 3640, 76021 Karlsruhe, Germany*

Electronic correlations and nematic fluctuations of $\text{Fe}_{1+y}\text{Se}_{0.5}\text{Te}_{0.5}$ are investigated by measuring resistivity, heat capacity, thermal expansion and Young's modulus. Using Te-vapor annealing, we have removed the excess-Fe in non-superconducting $\text{Fe}_{1+y}\text{Se}_{0.5}\text{Te}_{0.5}$ single crystals. We observe the appearance of superconductivity is necessarily accompanied by a divergence in the B_{2g} nematic susceptibility.

The Fe(Se,Te) system is the structurally simplest among the Fe-based superconductors. The end member FeTe is a non-superconducting anti-ferromagnet and is the most correlated among the Fe-based materials¹. The other end member FeSe is a superconductor ($T_C = 9$ K) and has a nematic-structural transition around 90 K with no magnetic order. The disappearance of nematic order with Te doping coincides with maximization of T_C to 14 K². Recently it has been shown that there is an evolution from (strongly correlated) metallic phase to orbital selective Mott phase in Fe(Se,Te) as Se concentration is reduced³.

The interplay between orbital selectivity and nematicity has also been highlighted using the elastoresistivity and inelastic neutron measurements^{4,5}. The substitution of Se in FeTe upto 12% results in the divergence of B_{1g} nematic susceptibility χ . The inelastic neutron experiments in this region show short-range magnetic correlations near $(0, \pi)$. On further substitution of Se, the $\chi_{B_{1g}}$ becomes independent of temperature and the $\chi_{B_{2g}}$ diverges, with appearance of (π, π) spin fluctuations. The $\chi_{B_{2g}}$ signal shows a Curie-Weiss behavior upto 50 K. The deviation above this temperature is explained by the orbital selectivity in $\text{FeSe}_{1-x}\text{Te}_x$.

These studies suggest that the nematic and magnetic fluctuations, as well as orbital physics, are strongly intertwined in Fe(Se,Te). We aim to study these effects in Fe(Se,Te) with help of thermal expansion and Young's modulus measurement.

Large single crystals of $\text{FeSe}_{0.5}\text{Te}_{0.5}$ were obtained

using Bridgman method and characterized using Laue diffraction. The single crystals obtained via this route often contain a significant amount of excess interstitial iron. To remove this excess iron, we follow the Te-vapor annealing method⁶. Different annealing time and molar ratio of crystals to Te were tried to maximize the superconducting volume fraction and transition temperature.

The heat capacity, which probes the volume superconductivity, was measured before and after annealing. Nearly 100% superconducting volume fraction were realised as indicated by the very small residual C/T values at low temperature. There are clear superconducting anomalies in the annealed samples although longer annealing reduces the T_C .

The thermal expansion plotted as α/T highlights that the electronic contribution is quite anomalous. It shows a large anomaly at the superconductivity transition and an electronic signal that is very non-Fermi liquid like over the whole temperature range up to room temperature and appears to diverge slowly down to the superconducting transition. This is likely related the orbital-selective-Mott transition, but needs to be studied further.

The Young's modulus of the sample has been measured using 3-point bending in a capacitance dilatometer⁷. The shear modulus C_{66} is obtained by measuring the Young's modulus along the tetragonal [110] direction. The annealed samples show a softening in the elastic shear modulus. The superconductivity is always accompanied with a diverging nematic signal. The nematic susceptibility obtained fits with the Curie-Weiss dependence.

¹ Z. Yin, K. Haule, and G. Kotliar, *Kinetic frustration and the nature of the magnetic and paramagnetic states in iron pnictides and iron chalcogenides*, Nature materials **10**, 932 (2011).

² J. M. Tranquada, G. Xu, and I. A. Zaliznyak, *Magnetism and superconductivity in $\text{Fe}_{1+y}\text{Te}_{1-x}\text{Se}_x$* , Journal of Physics: Condensed Matter **32**, 374003 (2020).

³ M. Yi, Z. Liu, Y. Zhang, R. Yu, J.-X. Zhu, J. Lee, R. Moore, F. Schmitt, W. Li, S. Riggs, et al., *Observation of universal strong orbital-dependent correlation effects in iron chalcogenides*, Nature communications **6**, 1 (2015).

⁴ Q. Jiang, Y. Shi, M. H. Christensen, J. Sanchez, B. Huang,

Z. Lin, Z. Liu, P. Malinowski, X. Xu, R. M. Fernandes, et al., *Nematic fluctuations in an orbital selective superconductor $\text{Fe}_{1+y}\text{Te}_{1-x}\text{Se}_x$* , arXiv preprint arXiv:2006.15887 (2020).

⁵ T. Liu, J. Hu, B. Qian, D. Fobes, Z. Q. Mao, W. Bao, M. Reehuis, S. Kimber, K. Prokeš, S. Matas, et al., *From $(\pi, 0)$ magnetic order to superconductivity with (π, π) magnetic resonance in $\text{Fe}_{1.02}\text{Te}_{1-x}\text{Se}_x$* , Nature materials **9**, 718 (2010).

⁶ Z. Xu, J. Schneeloch, M. Yi, Y. Zhao, M. Matsuda, D. Pajerowski, S. Chi, R. Birgeneau, G. Gu, J. Tranquada, et al., *Coexistence of superconductivity and short-range double-*

stripe spin correlations in te-vapor annealed FeTe_{1-x}Se_x ($x \leq 0.2$), Physical Review B **97**, 214511 (2018).

⁷ A. E. Böhrer and C. Meingast, *Electronic nematic sus-*

ceptibility of iron-based superconductors, Comptes Rendus Physique **17**, 90 (2016).

Bipartite entropy build-up in open system matrix product state simulations

G. Preisser,¹ D. Wellnitz,^{2,1} V. Alba,³ J. Dubail,^{4,1} and J. Schachenmayer^{1,2,*}

¹*ISIS (UMR 7006), CNRS and Université de Strasbourg, 67000 Strasbourg, France*

²*IPCMS (UMR 7504), CNRS, 67000 Strasbourg, France*

³*Institute for Theoretical Physics, Universiteit van Amsterdam, Science Park 904, Postbus 94485, 1098 XH Amsterdam, The Netherlands*

⁴*Université de Lorraine, CNRS, LPCT, F-54000 Nancy, France*

(Dated: September 8, 2021)

We analyze the far-from-equilibrium dynamics in open one dimensional quantum spin models in presence of spontaneous emission and absorption, and with dephasing. We study the growth of von Neumann entropies of bipartitions in numerical simulations of a many-body Lindblad master equation. We compare simulations where the full density matrix is expressed as a matrix product operator (MPO) with simulations where the density matrix is unravelled into quantum trajectories (QT+MPS). For large dissipation we find that the quantum trajectory approach, while dealing with a much smaller state space, can exhibit significantly larger entropy build-up and a less favorable scaling with time. In some scenarios, this can make the MPO approach fundamentally more efficient than QT+MPS. We furthermore point out other fundamental technical advantages of the MPO approach regarding the time-step convergence behavior. Compared to other approaches for matrix product density matrices, here we introduce a new decomposition in terms of a generalized matrix product Bloch vector, which exhibits certain numerical advantages.

I. EXTENDED ABSTRACT

In recent years, experimental developments have made it possible to analyze and control almost fully coherent quantum many-body dynamics [1], in particular for effective spin-1/2 models, e.g. with trapped ultracold atoms or molecules in optical lattices [2, 3], Rydberg excitations [4–7], or ion traps [8]. One focus of such setups has been to experimentally measure the evolution of bipartite entanglement entropies [9–11]. The study of such entanglement in many-body models has been a long-standing theory quest [12, 13], especially also their time-dependent growth [14].

The interest in entanglement evolution is partly motivated by the fact that in one dimension (1D), the growth of bipartite entanglement entropy (S) between two blocks of the chain, can be directly connected to the question whether dynamics can be simulated on a classical computer. This connection can be made via the concept of matrix product states (MPS) [15–18]. An MPS is a numerical decomposition of a many-body state vector into a product of $\chi \times \chi$ matrices (where the entries of the matrices are local kets). In such a representation, the bipartite entanglement is limited by $\max[S] \propto \log(\chi)$. Consequently, to represent a state as MPS over time, the matrix size has to evolve as $\chi \propto \exp(S)$. An evolution where S increases faster than logarithmic can therefore be considered computationally inefficient.

In nature, every experiment has small couplings to an environment, and should therefore be considered as an

open quantum system with a state described by a density matrix $\hat{\rho}$. Then, the definition of entanglement becomes more delicate: A bipartition of the 1D chain into two blocks is effectively a tripartition, with the environment acting as third party. Nevertheless, analogously to MPS for pure states, also a matrix product decomposition of the density matrix (MPO) can be defined. Also then, a bipartite entropy of such a decomposition, denoted as operator space entanglement (OSEE) [19, 20], determines the efficiency of the representation. Alternatively, the density matrix is a statistical mixture of pure states. Therefore, its evolution can also be described by a finite number of (stochastic) pure state trajectories, a technique known as quantum Monte-Carlo wavefunction method or quantum trajectories (QT) [21]. Then, each trajectory pure state can itself be expressed as MPS, and the bipartite entropy of each trajectory determines the efficiency of the numerical simulation. We denote this approach as QT+MPS.

Using these two approaches, we study bipartite entropy growth in a 1D XXZ spin-chain under a Lindblad master equation. Comparing both approaches we find considerable advantages of MPO over QT+MPS, which are related mainly with a bigger convergence value for time-step and less entropy growth, especially on large time scales. Such advantages become more significant the more sites there are on the spin chain, making MPO a more efficient approach.

* schachenmayer@unistra.fr

[1] J. I. Cirac and P. Zoller, Goals and opportunities in quantum simulation, *Nat. Phys.* **8**, 264 (2012).

[2] I. Bloch, J. Dalibard, and S. Nascimbène, Quantum sim-

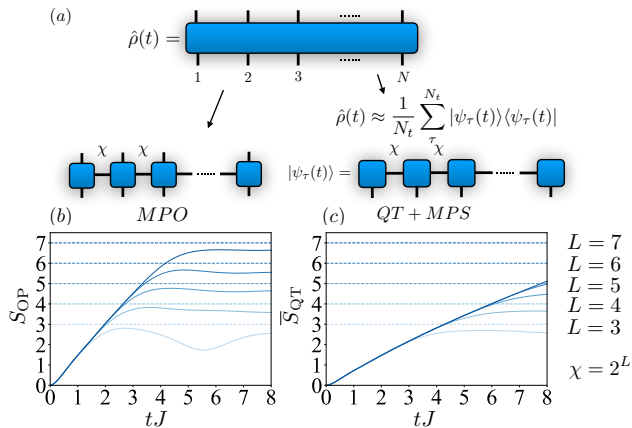


FIG. 1. (a) Schematics of different state representations to numerically simulate master equation dynamics in terms of: i) a decomposition of the density matrix into an MPO; or ii) with an unravelling of the density matrix into MPS quantum trajectories (MPS+QT). Both representation are limited by a finite bond dimension χ , which limits the bipartite entropies that can be captured (see text). (b/c) Example evolution of bipartite entropies for the two different state representations S_{OP} [for MPO, panel (b)] and S_{QT} [for QT, panel (c)] under the master equation with very small dissipation ($N = 40$, $J = V = 1$, $\gamma_{\pm} = 0.01J$, initial Néel state). Shown are simulations with increasingly large bond dimensions $\chi = 2^L$ and $L = 3, \dots, 7$.

ulations with ultracold quantum gases, *Nat. Phys.* **8**, 267 (2012).

- [3] B. Gadway and B. Yan, Strongly interacting ultracold polar molecules, *J. Phys. B: At. Mol. Opt. Phys.* **49**, 152002 (2016).
- [4] R. Löw, H. Weimer, J. Nipper, J. B. Balewski, B. Butscher, H. P. Büchler, and T. Pfau, An experimental and theoretical guide to strongly interacting Rydberg gases, *J. Phys. B: At. Mol. Opt. Phys.* **45**, 113001 (2012).
- [5] C. S. Adams, J. D. Pritchard, and J. P. Shaffer, Rydberg atom quantum technologies, *J. Phys. B: At. Mol. Opt. Phys.* **53**, 012002 (2019).
- [6] A. Browaeys and T. Lahaye, Many-body physics with individually controlled Rydberg atoms, *Nat. Phys.* **16**, 132 (2020).
- [7] M. Morgado and S. Whitlock, Quantum simulation and computing with rydberg-interacting qubits, *AVS Quantum Science* **3**, 023501 (2021).

- [8] R. Blatt and C. F. Roos, Quantum simulations with trapped ions, *Nat. Phys.* **8**, 277 (2012).
- [9] R. Islam, R. Ma, P. M. Preiss, M. Eric Tai, A. Lukin, M. Rispoli, and M. Greiner, Measuring entanglement entropy in a quantum many-body system, *Nature* **528**, 77 (2015).
- [10] A. M. Kaufman, M. E. Tai, A. Lukin, M. Rispoli, R. Schittko, P. M. Preiss, and M. Greiner, Quantum thermalization through entanglement in an isolated many-body system, *Science* **353**, 794 (2016).
- [11] A. Daley, H. Pichler, J. Schachenmayer, and P. Zoller, Measuring entanglement growth in quench dynamics of bosons in an optical lattice, *Physical review letters* **109**, 020505 (2012).
- [12] L. Amico, R. Fazio, A. Osterloh, and V. Vedral, Entanglement in many-body systems, *Rev. Mod. Phys.* **80**, 517 (2008).
- [13] J. Eisert, M. Cramer, and M. B. Plenio, Colloquium: Area laws for the entanglement entropy, *Rev. Mod. Phys.* **82**, 277 (2010).
- [14] V. Alba and P. Calabrese, Entanglement dynamics after quantum quenches in generic integrable systems, *SciPost Phys.* **4**, 017 (2018).
- [15] G. Vidal, Efficient Simulation of One-Dimensional Quantum Many-Body Systems, *Phys. Rev. Lett.* **93**, 040502 (2004).
- [16] F. Verstraete, V. Murg, and J. I. Cirac, Matrix product states, projected entangled pair states, and variational renormalization group methods for quantum spin systems, *Adv. Phys.* **57**, 143 (2008).
- [17] U. Schollwöck, The density-matrix renormalization group in the age of matrix product states, *Ann. Phys.* **326**, 96 (2011).
- [18] S. Paeckel, T. Köhler, A. Swoboda, S. R. Manmana, U. Schollwöck, and C. Hubig, Time-evolution methods for matrix-product states, *Ann. Phys.* **411**, 167998 (2019).
- [19] V. Alba, J. Dubail, and M. Medenjak, Operator entanglement in interacting integrable quantum systems: The case of the rule 54 chain, *Phys. Rev. Lett.* **122**, 250603 (2019).
- [20] J. Dubail, Entanglement scaling of operators: a conformal field theory approach, with a glimpse of simulability of long-time dynamics in 1+1d, *Journal of Physics A: Mathematical and Theoretical* **50**, 234001 (2017).
- [21] A. J. Daley, Quantum trajectories and open many-body quantum systems, *Adv. Phys.* **63**, 77 (2014).

Superconductor-mediated coupling of spin qubits and the impact of spin-orbit interaction

Maria Spethmann,¹ Xiangpeng Zhang,¹ Jelena Klinovaja,¹ and Daniel Loss¹

¹*Department of Physics, University of Basel, 4056 Basel, Switzerland*

Spin-based quantum computing requires two-qubit gates with spin-spin interaction. It was previously shown that spin qubits can be coupled via the Cooper pairs of a superconductor, allowing the dots to be further apart than in a setup where the quantum dots are directly coupled¹. Here we analyze how this superconductor-mediated coupling is influenced by spin-orbit interaction. We find that the spin-orbit interaction rotates the spin bases of the dots and results in additional anisotropic interaction and Dzyaloshinskii-Moriya interaction.

Introduction

Spin qubits² consists of quantum dots with a bound electron. The two spin states of this electron define the two logical states of the qubit. Single qubit rotations can be performed by applying a magnetic field pulse. In order to perform arbitrary calculations within a quantum computer, one also needs to realize at least one two-qubit gate, where the spins of two different qubits interact and get entangled. The most widely used method to couple two spin qubits is to vary the voltage barrier between the dots and allow for a small tunneling probability, giving rise to a Heisenberg-type exchange coupling². However, Choi *et al.*¹ proposed to couple the quantum dots not directly but via a superconductor, as shown in Fig. 1. We emphasize that this superconductor is not a resonator. Such a superconductor-mediated coupling has two advantages: First, the spin can be coupled over distances as large as the superconducting coherence length¹ (e.g. $\sim 1 \mu\text{m}$ for aluminum³), whereas directly coupled quantum dots need to have a distance of the order 100 nm ⁴. The reason is that the coupling is mediated by Cooper pairs in the superconductor, which consist of two electrons with correlated, opposite spins. The second advantage of this superconductor-mediated coupling is that when a second superconducting lead is added such that the system

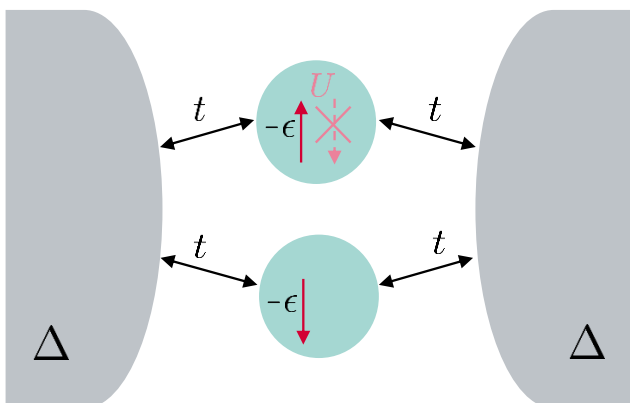


FIG. 1: Model setup: Two quantum dots (turkis) are tunnel coupled to two superconductors (gray) but not to each other

builds a Josephson Junction, the spin-spin interaction can be controlled by the phase difference between the superconductors.¹

Experimentally, the manufacture of such a device has recently started to become possible. In Ref.⁵ they realized a setup with strong coupling between superconductor and quantum dots. Their transport measurements show signature of a so-called Andreev molecule, a state resulting from the hybridization of the quantum dot states through an Andreev process. A closely related set of experiments are Cooper pair splitters, where Cooper pairs from a superconductor are split up into spin-entangled electrons on different quantum dots, very similar to our mechanism⁶.

Here we want to extend the model of Choi *et al.* by including spin orbit interaction, which is present in many materials and is therefore of interest.

Superconductor-mediated coupling of spin qubits: Review of Choi *et al.*¹

Our model consists of two quantum dots

$$H_D = \sum_{n\sigma} (-\epsilon) \hat{d}_{n\sigma}^\dagger \hat{d}_{n\sigma} + U \hat{d}_{n\uparrow}^\dagger \hat{d}_{n\uparrow} \hat{d}_{n\downarrow}^\dagger \hat{d}_{n\downarrow} \quad (1)$$

where $\hat{d}_{n\sigma}^\dagger$ creates an electron at dot number $n = 1, 2$ with spin σ at the energy level $-\epsilon$ and with onsite Coulomb repulsion U . U is assumed to be the largest energy scale of the system, such that we can neglect any doubly occupied dot states in our calculation. Next, we have two superconducting leads

$$H_S = \sum_{j\mathbf{k}} \sum_{\sigma} \xi_{\mathbf{k}} \hat{c}_{j\mathbf{k}\sigma}^\dagger \hat{c}_{j\mathbf{k}\sigma} - \Delta_j \hat{c}_{j\mathbf{k}\uparrow}^\dagger \hat{c}_{j-\mathbf{k}\downarrow}^\dagger + H.c. \quad (2)$$

where $\hat{c}_{j\mathbf{k}\sigma}^\dagger$ creates an electron at superconductor $j = L, R$ with wave vector \mathbf{k} and energy $\xi_{\mathbf{k}}$, and $\Delta_j = \Delta e^{-i\phi_j}$ is the pairing potential with superconducting phase ϕ_j and gap Δ . Finally, Choi *et al.* include a weak tunnel coupling

$$H_T = \sum_{j\mathbf{k}n\sigma} t_{j\mathbf{k}} \hat{c}_{j\mathbf{k}\sigma}^\dagger \hat{d}_{n\sigma} + H.c.$$

between the dots and the lead described by the tunnel parameter t_{jk} . Choi *et al.* now calculate the effective Hamiltonian in the spin-1/2 subspace by treating H_T as a perturbation. Since at least four tunnel processes are needed for the spins on the dot to interact, the perturbation is taken at the fourth order and requires $\pi t^2 \rho_F \ll \epsilon, \Delta \ll U$. Choi *et al.* evaluate the perturbation theory by diagonalizing the superconducting Hamiltonian via a Bogoliubov transformation and summing up all virtual intermediate states. Their result is a Heisenberg interaction ($\epsilon \ll \Delta$)

$$H_{\text{eff}} = \tilde{J} t^4 \boldsymbol{\sigma}_1 \cdot \boldsymbol{\sigma}_2, \quad \tilde{J} \propto \frac{\rho_F^2}{\epsilon} (1 + \cos(\phi_L - \phi_R)) \quad (3)$$

with positive exchange coupling \tilde{J} , which depends on the superconducting phase difference. Since \tilde{J} is positive, the ground state is a singlet, a result of the singlet pairing of the superconductors. When we assume the tunnel amplitudes to differ between the two dots, $t = t_n$, the effective Hamiltonian is evaluated to be $H_{\text{eff}} = \tilde{J} t_1^2 t_2^2 \boldsymbol{\sigma}_1 \cdot \boldsymbol{\sigma}_2$.

Extending the model with spin-orbit coupling

Spin-orbit coupling is a relativistic effect, where an electron moving through an electric field experiences this electric field as a magnetic field in its rest system. This magnetic field couples to the spin, such that the spin starts to precess around the effective magnetic field axis. An electric field can be intrinsically present in a material due to bulk inversion asymmetry of the crystal, and also arises from the confining potential. We include spin-orbit interaction in our model by introducing a nonzero probability of the spin to flip during the tunnel process t' and by making the tunnel amplitudes complex.

$$H_T = \sum_{jkn\sigma} t_{jkn\sigma} \hat{c}_{jkn\sigma}^\dagger \hat{d}_{n\sigma} + t'_{jkn\sigma} \hat{c}_{jkn\sigma}^\dagger \hat{d}_{n-\sigma} + H.c. \quad (4)$$

$$t_{jkn\sigma} \propto t_n e^{i\sigma\alpha_n}$$

$$t'_{jkn\sigma} \propto \sigma t'_n e^{i\sigma\alpha'_n}$$

Here we parameterized the complex tunnel parameters by their absolute values t_n, t'_n and their complex arguments $\sigma\alpha_n, \sigma\alpha'_n$, which depend on the spin in order to preserve time reversal symmetry.

Our ansatz translates into a dot-dependent rotation of the degenerate spin-up and spin-down states of the dot.

$$\begin{pmatrix} \hat{d}_{n\uparrow} \\ \hat{d}_{n\downarrow} \end{pmatrix} := M_n \begin{pmatrix} \hat{d}_{n\uparrow} \\ \hat{d}_{n\downarrow} \end{pmatrix} \quad (5)$$

$$M_n := \frac{1}{\sqrt{t_n^2 + t_n'^2}} \begin{pmatrix} t_n e^{i\alpha_n} & t'_n e^{i\alpha'_n} \\ -t'_n e^{-i\alpha'_n} & t_n e^{-i\alpha_n} \end{pmatrix} =: e^{i\frac{1}{2}\phi_n \mathbf{u}_n \cdot \boldsymbol{\sigma}} \quad (6)$$

The parameter ϕ_n are defined as the length and \mathbf{u}_n as the direction of the rotation vector. In this rotated dot basis $\{\hat{d}_{n\sigma}\}$, we only have real, spin-conserving tunnel couplings. In other words, we can map our system with spin-orbit coupling to a system without spin-orbit coupling in the rotated dot basis.

$$H_T = \sum_{jkn\sigma} \sqrt{t_n^2 + t_n'^2} c_{jkn\sigma}^\dagger \tilde{d}_{n\sigma} + H.c. \quad (7)$$

Now we can easily evaluate the effective Hamiltonian and rotate back to our original basis. When we combine the two rotations on the dots into one single rotation with rotation vector $\phi \mathbf{u} = \phi_2 \mathbf{u}_2 - \phi_1 \mathbf{u}_1$ we get:

$$H_{\text{eff}} = \tilde{J} (t_1^2 + t_1'^2) (t_2^2 + t_2'^2) \times \left[\cos(\phi) \boldsymbol{\sigma}_1 \cdot \boldsymbol{\sigma}_2 + (1 - \cos(\phi)) (\mathbf{u} \cdot \boldsymbol{\sigma}_1) (\mathbf{u} \cdot \boldsymbol{\sigma}_2) + \sin(\phi) (\boldsymbol{\sigma}_1 \times \boldsymbol{\sigma}_2) \cdot \mathbf{u} \right]$$

We see that in addition to the isotropic Heisenberg exchange we obtain anisotropy in \mathbf{u} direction, as well as a Dzyaloshinskii-Moriya interaction in \mathbf{u} direction.

Conclusion

We analyzed the effect of spin-orbit interaction on the superconductor-mediated coupling of two quantum dots. We found that spin-orbit interaction rotates the spin basis on the dots, which results in additional anisotropic spin-spin interaction and Dzyaloshinskii-Moriya interaction.

Acknowledgments

This work was supported by the Swiss National Science Foundation and NCCR SPIN.

¹ M. S. Choi, C. Bruder, and D. Loss, *Spin-dependent Josephson current through double quantum dots and measurement of entangled electron states*, Phys. Rev. B **62**, 13569 (2000).
² D. Loss and D. P. DiVincenzo, *Quantum computation with quantum dots*, Phys. Rev. A **57**, 120 (1998).
³ M. Veldhorst, C. H. Yang, J. C. Huang, W. Huang, J. P. Dehollain, J. T. Muhonen, S. Simmons, A. Laucht, F. E. Hudson, K. M. Itoh, et al., *A two-qubit logic gate in silicon*, Nature **526**, 410 (2015).

⁴ C. Kittel, *Introduction to Solid State Physics* (Wiley, New York, 2004), 8th ed.
⁵ O. Kürtössy, Z. Scherübl, G. Fülöp, I. E. Lukács, T. Kanne, J. Nygård, P. Makk, and S. Csonka, *Andreev molecule in parallel InAs nanowires* (2021), arXiv: 2103.14083.
⁶ L. Hofstetter, S. Csonka, A. Baumgartner, G. Fülöp, S. D'Hollosy, J. Nygård, and C. Schönenberger, *Finite-bias Cooper pair splitting*, Phys. Rev. Lett. **107**, 2 (2011).

Fabrication of FD-SOI Single Electron Transistors for spin qubits readout

Fabio Bersano, Franco De Palma, Yingfen Wei and Adrian M. Ionescu¹

¹*Nanoelectronic Devices Laboratory (Nanolab), École Polytechnique Fédérale de Lausanne, Lausanne 1015, Switzerland*

Semiconductor based spin qubits are good candidates for the implementation of a quantum information processor thanks to the long coherence times of spins in semiconductors and scalability of the technology. Optimized fabrication recipes are needed for a precise control of electronic energy levels in quantum dots (qdots) while limiting spin decoherence due to charge noise. In our work we focus on one of the simplest devices based on the quantum dots technology, validating an optimized process flow for the fabrication of a Single Electron Transistor for charge sensing and spin qubits readout on Fully Depleted Silicon-On-Insulator substrates (FD-SOI) towards a future integration of FD-SOI qubits.

I. FD-SOI SET AS A CHARGE SENSOR FOR SPIN QUBITS READOUT

In 1998, Loss and DiVincenzo proposed the implementation of qubits with the spin of electrons confined in quantum dots through the use of electrostatic fields generated by conductive gates¹. This strategy has the important advantage of enabling qubits manipulations with the same gates used to induce the quantum confinement. Indeed, the interaction between dots can be simply controlled by tuning gates voltages and is greatly facilitated by the relatively large spatial extent of electron wave functions in semiconductor dots². FD-SOI qubits have the potential advantage of using independent gates to tune qubits properties and making further substrate engineering to reduce the charge noise while introducing additional vertical confinement thanks to the thin top silicon film. A noninvasive and fast sensing of charge displacement is needed to probe the dots occupancy for the qubits readout upon manipulation. To do so, common planar architectures implementing single-spin qubits and quantum logical two-qubits gates rely on linear arrays of quantum dots coupled to a charge readout system. In our work, we plan to investigate the technological advantages of SOI substrates with the integration of spin qubits arrays and single electron transistors for fast and high fidelity readouts.

DEVICE LAYOUT AND OPERATING PRINCIPLE

The SET is here taken as the leading qdot structure towards the fabrication of multiple-dot devices. In our device, a single quantum dot is electrostatically defined by two barrier gates (B1, B2 in fig.2a) and a plunger gate (PG) that respectively control depletion and inversion/accumulation of charges. Tunneling events through the qdot occur when electron energy levels sit within the bias window set by the drain to source voltage V_{SD} and the plunger gate voltage V_{PG} ; when this condition is satisfied, a current I_{SET} is measured, otherwise the charge transport is blocked. This effect is known as *Coulomb blockade*. Thanks to the high sensitivity to single electrical charges, SETs can be capacitively coupled to other qdots (such as qubits) to enable current fluctua-

tions when charge transitions occur³. The maximum sensitivity of the SET current to electrical field fluctuations is achieved when biasing the device to a Coulomb blockade edge, so that a small shift in the chemical potential of the dots results in an appreciable current fluctuation⁴. The several sources of noise can be studied analyzing the power spectral density components in frequency of the output signal, giving helpful physical insights for the optimization of the device layout and fabrication recipes (figure 1).

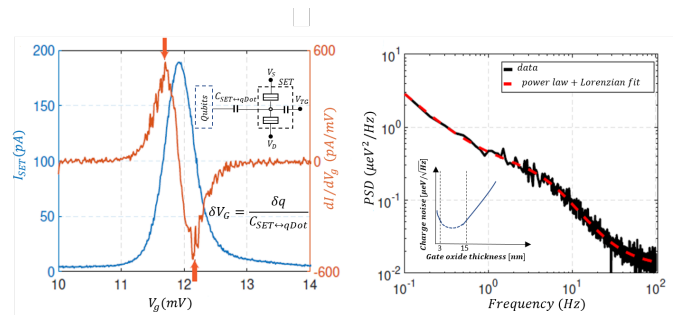


FIG. 1: current of a SET plotted in proximity to a Coulomb blockade edge and its power spectral density function versus frequency showing a typical $1/f$ noise⁴. Insets show the coupled architecture of the sensor with qubits and the expected dependence of charge noise on the gate oxide thickness.

II. FABRICATION RESULTS

Past works proved that charge noise in MOS-qdots is impacted by the quality and thickness of the oxide layers⁵. Therefore, we decided to analyze the charge trap density in the gate oxide through the electrical characterization of MOS capacitors fabricated with different processes. C-V curves have been measured at several frequencies before and after performing rapid thermal annealings (RTAs) to study their impact on the oxide quality. Figure 2b summarizes the results of C-V curves measured at 100 kHz, showing how the electrical characteristics shift towards ideal values when performing a dry oxidation in DCE and RTAs at 400°C. However, the high temperature annealing needed for dopants activa-

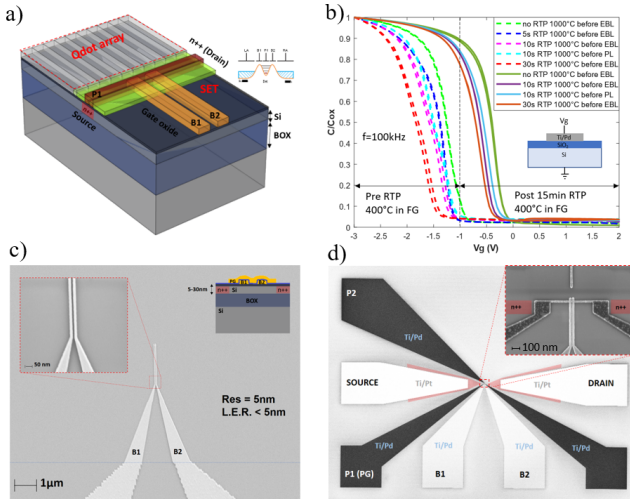


FIG. 2: a) schematic of a FD-SOI SET coupled to an array of quantum dots (i.e., qubits) b) effect of RTA at 400°C and 1000°C on C-V curves of MOS capacitors c) Ti-Pd barrier gates with minimal line edge roughness d) fabricated multi-layered device showing the dependence of metallic grains on the oxide underneath.

tion, when performed in N_2 atmosphere, negatively impacts the oxide. Another possible source for charge noise comes from metallic grains residues due to lithographic imperfections⁶. To solve this issue, we studied the optimal combination of electron beam current and doses to minimize the line edge roughness of Ti/Pd gates fabricated through evaporation and lift-off (figure 2c). Fi-

nally, figure 2d shows the complete EBL layout of the SET, where an additional top plunger gate (P2) is introduced to induce charges in proximity to the sensor. Here, barrier and plunger gates are separated by 5nm of Al_2O_3 deposited through atomic layer deposition. From the zoomed SEM image, it is evident that the RTP at 400°C improves the uniformity of barrier gates facing the high-quality thermally grown SiO_2 but not the ones on the deposited Al_2O_3 . Therefore, other interlayer oxides need to be tested and characterized with further experimental work.

III. CONCLUSIONS

A process flow for the fabrication of a SET with low charge traps density and high quality Palladium gates has been proposed and validated. The presented studies for the optimization of oxides and metallic gates will lead to the optimal integration scheme for future electron spin qubits architectures with high fidelity and low noise readout systems.

Acknowledgments

We would like to thank F. Braakman and M. Poggio for fruitful discussions about the integration scheme and planning of the work. This work is established as an initial part of the Electron Spin Qubits project conducted in collaboration with the University of Basel and IBM Zurich in the NCCR Spin network; it is funded by NCCR Spin.

¹ D. Loss and D. P. DiVincenzo, *Quantum computation with quantum dots*, Physical Review A **57**, 120 (1998).
² M. Eriksson, S. Coppersmith, and M. Lagally, *Semiconductor quantum dot qubits*, MRS bulletin **38**, 794 (2013).
³ J. Boter, *Scaling aspects of silicon spin qubits* (2020).
⁴ N. Holman, *Circuit Quantum Electrodynamics with Si/SiGe Quantum Dots* (The University of Wisconsin-Madison, 2020).

⁵ E. J. Connors, J. Nelson, H. Qiao, L. F. Edge, and J. M. Nichol, *Low-frequency charge noise in si/sige quantum dots*, Physical Review B **100**, 165305 (2019).
⁶ S. Kafanov, H. Brenning, T. Duty, and P. Delsing, *Charge noise in single-electron transistors and charge qubits may be caused by metallic grains*, Physical Review B **78**, 125411 (2008).

Poster abstract: Local and nonlocal quantum transport due to Andreev bound states in finite Rashba nanowires with superconducting and normal sections

Richard Hess, Henry F. Legg, Daniel Loss, and Jelena Klinovaja
 Department of Physics, University of Basel, Klingelbergstrasse 82, CH-4056 Basel, Switzerland

(Dated: September 8, 2021)

I. ABSTRACT

We analyze Andreev bound states (ABSs) that form in normal sections of a Rashba nanowire that is only partially covered by a superconducting layer. These ABSs are localized close to the ends of the superconducting section and can be pinned to zero energy over a wide range of magnetic field strengths even if the nanowire is in the nontopological regime [1–15]. For finite-size nanowires (typically $\lesssim 1 \mu\text{m}$ in current experiments, see e.g. Fig. 1), the ABS localization length is comparable to the length of the nanowire.

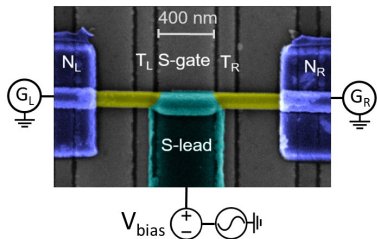


FIG. 1. Typical three-terminal device for conductance measurements: A semiconducting nanowire (yellow) is partially covered by a superconductor (green). Normal leads (blue) are attached to the left and right end of the nanowire. The figure is taken from reference [16]

The probability density of an ABS is therefore nonzero throughout the nanowire and differential-conductance calculations reveal a correlated zero-bias peak (ZBP) at both ends of the nanowire, see Fig. 2. When a second normal section hosts an additional ABS at the opposite end of the superconducting section, the combination of the two ABSs can mimic the closing and reopening of the bulk gap in local and nonlocal conductances accompanied by the appearance of the ZBP. These signatures are reminiscent of those expected for Majorana bound states (MBSs) but occur here in the nontopological regime. Our results demonstrate that conductance measurements of correlated ZBPs at the ends of a typical superconducting nanowire or an apparent closing and reopening of the bulk gap in the local and nonlocal conductance are not conclusive indicators for the presence of MBSs. Zero-energy sub gap states have already been measured in experiments. One example of magnetic field independent states is for example shown in Fig. 3, the experimental

setup for this measurement differs slightly from the setup shown in Fig. 1.

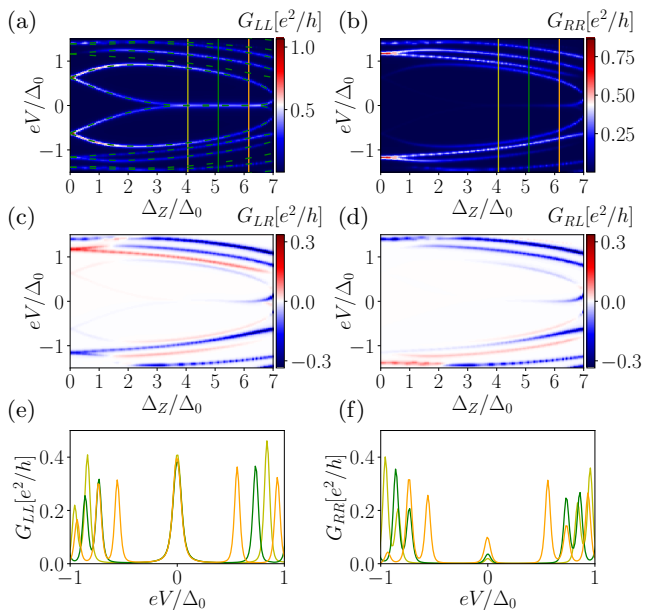


FIG. 2. Differential conductance in a non-topological nanowire containing one ABS on the left end that extends up to the right end. Both local conductances (a) G_{LL} and (b) G_{RR} exhibit a ZBP due to the extended nature of the ABS wave function. The conductance of the ABS is not quantized to $2e^2/h$ due to the shape of barriers chosen. This conductance pattern agrees well with the energy spectrum, indicated by the dark green dashed lines. The yellow, dark green, and orange solid line indicate line cuts of (e) G_{LL} and (f) G_{RR} at the Zeeman energies $\Delta_Z = \{4.01, 5.11, 6.16\}\Delta_0$. The non-local conductances (c) G_{LR} and (d) G_{RL} contain signatures of the extended ABSs and of the bulk-gap closing at Δ_Z^c . The figure is taken from reference [17]

II. ACKNOWLEDGEMENTS

This project has received funding from the European Union's Horizon 2020 research and innovation programme under Grant Agreement No 862046 and under Grant Agreement No 757725 (the ERC Starting Grant). This work was supported by the Georg H. Endress Foundation and the Swiss National Science Foundation.

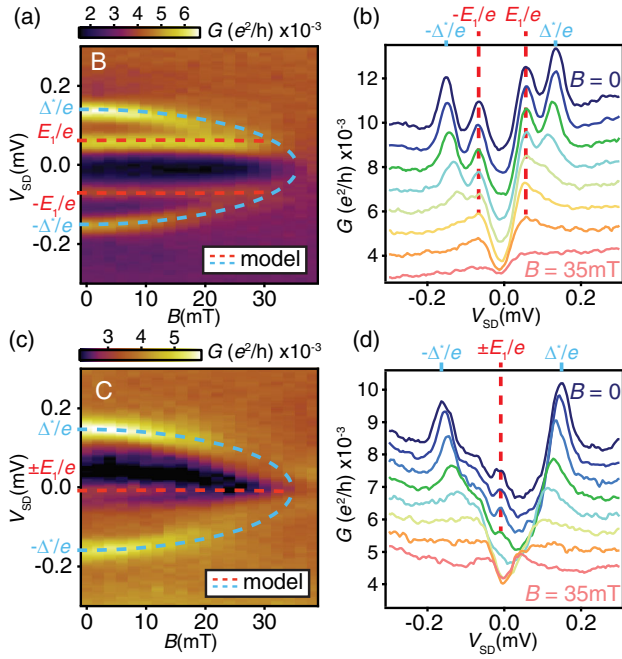


FIG. 3. Magnetic field independent sub gap states. The states can be pinned to zero energy. The figure is taken from reference [15]

-
- [1] G. Kells, D. Meidan, and P. W. Brouwer, *Phys. Rev. B* **86**, 100503 (2012).
 [2] E. J. H. Lee, X. Jiang, R. Aguado, G. Katsaros, C. M. Lieber, and S. De Franceschi, *Phys. Rev. Lett.* **109**, 186802 (2012).
 [3] J. Cayao, E. Prada, P. San-Jose, and R. Aguado, *Phys. Rev. B* **91**, 024514 (2015).
 [4] A. Ptok, A. Kobjalka, and T. Domański, *Phys. Rev. B* **96**, 195430 (2017).
 [5] C.-X. Liu, J. D. Sau, T. D. Stanescu, and S. Das Sarma, *Phys. Rev. B* **96**, 075161 (2017).
 [6] C. Reeg, O. Dmytruk, D. Chevallier, D. Loss, and J. Klinovaja, *Phys. Rev. B* **98**, 245407 (2018).
 [7] F. Peñaranda, R. Aguado, P. San-Jose, and E. Prada, *Phys. Rev. B* **98**, 235406 (2018).
 [8] C. Moore, T. D. Stanescu, and S. Tewari, *Phys. Rev. B* **97**, 165302 (2018).
 [9] A. Vuik, B. Nijholt, A. R. Akhmerov, and M. Wimmer, *SciPost Phys.* **7**, 61 (2019).
 [10] B. D. Woods, J. Chen, S. M. Frolov, and T. D. Stanescu, *Phys. Rev. B* **100**, 125407 (2019).
 [11] C.-X. Liu, J. D. Sau, T. D. Stanescu, and S. Das Sarma, *Phys. Rev. B* **99**, 024510 (2019).
 [12] J. Chen, B. D. Woods, P. Yu, M. Hocevar, D. Car, S. R. Plissard, E. P. A. M. Bakkers, T. D. Stanescu, and S. M. Frolov, *Phys. Rev. Lett.* **123**, 107703 (2019).
 [13] D. J. Alspaugh, D. E. Sheehy, M. O. Goerbig, and P. Simon, *Phys. Rev. Research* **2**, 023146 (2020).
 [14] E. Prada, P. San-Jose, M. W. A. de Moor, A. Geresdi, E. J. H. Lee, J. Klinovaja, D. Loss, J. Nygård, R. Aguado, and L. P. Kouwenhoven, *Nat. Rev. Phys.* **2**, 575 (2020).
 [15] C. Jünger, R. Delagrangé, D. Chevallier, S. Lehmann, K. A. Dick, C. Thelander, J. Klinovaja, D. Loss, A. Baumgartner, and C. Schönenberger, *Phys. Rev. Lett.* **125**, 017701 (2020).
 [16] P. Yu, J. Chen, M. Gomanko, G. Badawy, E. P. A. M. Bakkers, K. Zuo, V. Mourik, and S. M. Frolov, *Nat. Phys.* **17**, 482 (2021).
 [17] R. Hess, H. F. Legg, D. Loss, and J. Klinovaja, *Phys. Rev. B* **104**, 075405 (2021).

Storing single photons from an SPDC source in a Rb quantum memory

Madhavakkannan Saravanan,¹ Gianni Buser,¹ Roberto Mottola,¹

Björn Cotting,¹ Janik Wolters,^{2,1} and Philipp Treutlein¹

¹*Department of Physics, University of Basel, Switzerland*

²*Deutsches Zentrum für Luft- und Raumfahrt e.V. (DLR),
Institute of Optical Sensor Systems, Rutherfordstr. 2, 12489 Berlin, Germany*

Quantum memories are a key ingredient for the realization of quantum networks¹. Furthermore, they allow for the synchronization of probabilistic single photon sources significantly enhancing the generation rates of multiphoton states². We implemented a broadband, optical quantum memory in hot Rb vapor with on-demand storage and retrieval³. With a bandwidth matched spontaneous parametric downconversion source, we can generate heralded single photons suited for storage with a heralding efficiency $\approx 40\%$ ⁴. We report on our recent achievements in storing downconverted single photons with a linewidth of 370 MHz with the measurement of the second order autocorrelation of retrieved single photons results in $g^{(2)} \sim 0.2$, showing that the non-classical properties of the stored light are maintained.

I. INTRODUCTION

Single photons are a vital resource for optical quantum information processing. Experimental demonstrations of optical quantum processing have generally been implemented using non-deterministic sources, such as spontaneous parametric down conversion (SPDC) photon pair sources. Applications like linear optical quantum computing and boson sampling require N photon states to perform calculations on photonic circuits. Unfortunately, the scaling of spontaneous photon sources to N simultaneous photons is challenging. This problem is addressed by synchronization: Quantum memories capable of storing photons until they are needed solve this scaling limitation. Hot vapor memories in particular are a promising platform due to the high acceptance bandwidths and technical simplicity. The latter point promises reliable field-usability and miniaturization akin to what we have seen in the development of vapor cell based atomic clocks once the memory performance justifies this kind of scaling. A long standing problem that has plagued both our own past implementation³ and those of many others⁵ is read-out noise ruining the retrieved photon quality as measured by number statistics. Furthermore, only a few hot vapor memories have been interfaced with actual single photon sources due to source compatibility issues. We address both of these problems by exploiting polarization selection rules to operate the memory with low noise in the long-lived electronic ground state, and by building a tailored photon source⁴, designed to match the performance of our memory.

A. SPDC Source

Spontaneous parametric down conversion is a non-linear process where one high energy photon from a pump beam is split into two low-energy signal and idler photons. This is generally implemented using a solid state non linear crystal, where the crystal is pumped using a pump beam to produce degenerate or non degenerate

down converted photons. To interface such sources with atomic memories requires tailoring the source frequency and bandwidth to the atomic lines used for storage. Considerable progress along those lines has been made in recent years, including cavity SPDC sources. In our experiment a blue laser of wavelength 404 nm is shone on a periodically poled potassium titanyl phosphate crystal to produce non-degenerate signal and idler photons at 795 nm and 822 nm respectively. The poling of the crystal was engineered such that the wavelength of the signal photons matched the ⁸⁷Rb D₁ line. The idler photon heralds the presence of a signal photon on its way to the memory, and a heralding efficiency of 40 % was achieved in our setup⁴.

B. Rb Quantum Memory

In the last decade many implementations of quantum memories have been shown, including in ultra cold atomic ensembles and lattices, trapped ions, and atoms inside cavities. In our setup the memory is implemented in the ground state of a room temperature Rb vapor cell using the principle of electromagnetically induced transparency (EIT). EIT is a nonlinear optical phenomenon observed in atoms which have a Λ scheme energy level structure. Two optical fields, a signal field that carries the quantum information and a strong control field, couple the excited states to their corresponding ground states. If the control field is absent the signal field is partially or completely absorbed. However, in the presence of the control field, the propagation of the signal field through the medium is altered. If both fields are near resonant with the transition the different paths for light absorption interfere destructively and create a transparency window for the signal photons to transverse. This also changes the group velocity of the signal field inside the medium to slow down the signal photons. By adiabatically turning the control field off the signal field is stored in the medium. This stored signal field can be retrieved on demand by applying the control field following time reversal symmetry. The level scheme

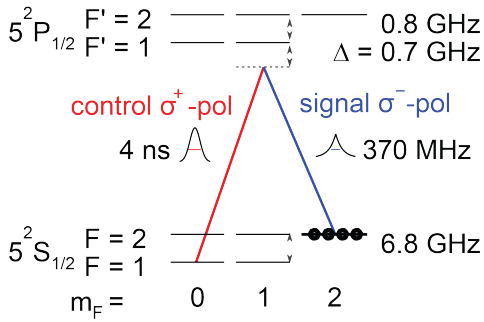


FIG. 1: Level scheme of the Rb atoms used in our experiment

of the ^{87}Rb D_1 line is shown in Fig 1. In our experiment optical pumping and selection rules are used to isolate a four-level lambda system. The signal field couples $|g\rangle = |F = 2, m_F = 2\rangle \rightarrow |e\rangle = |F' = 1, m'_F = 1\rangle$ and the control field couples $|s\rangle = |F = 1, m_F = 0\rangle \rightarrow |e\rangle$. Both fields are equally red detuned from their transitions. In the presence of the control field, the signal field is stored as a spin wave excitation between the initially prepared

ground state $|g\rangle$ and the storage state $|s\rangle$.

II. POSTER

We report low-noise single-photon storage by combining a tailored heralded single photon source based on spontaneous parametric down-conversion and a matched memory based on electromagnetically induced transparency in warm ^{87}Rb vapor. The bandwidth of the 795 nm photons emitted by the source is 370 MHz, placing it both in a technologically relevant regime and well within the acceptance bandwidth of the memory. Simultaneously, the experimental complexity is kept comparatively low, all components operating at or above room-temperature. Using polarization selection rules in the Zeeman substructure of the atoms we reduce the noise of the memory considerably while storing the photons in the electronic ground state of the atoms. The memory preserves the quantum signature in the photon number statistics of the retrieved photons, with $g_{\text{c,ret}}^{(2)} \sim 0.2$ proving that the emission from the memory is dominated by single photons.

- ¹ N. Sangouard, C. Simon, H. De Riedmatten, and N. Gisin, *Quantum repeaters based on atomic ensembles and linear optics*, *Reviews of Modern Physics* **83**, 33 (2011).
- ² J. Nunn, N. K. Langford, W. S. Kolthammer, T. F. M. Champion, M. R. Sprague, P. S. Michelberger, X.-M. Jin, D. G. England, and I. A. Walmsley, *Enhancing multiphoton rates with quantum memories*, *Physical Review Letters* **110**, 133601 (2013).
- ³ J. Wolters, G. Buser, A. Horsley, L. Béguin, A. Jöckel, J.-P. Jahn, R. J. Warburton, and P. Treutlein, *Simple atomic quantum memory suitable for semiconductor quantum dot*

- single photons*, *Physical Review Letters* **119**, 060502 (2017).
- ⁴ R. Mottola, G. Buser, C. Müller, T. Kroh, A. Ahlrichs, S. Ramelow, O. Benson, P. Treutlein, and J. Wolters, *An efficient, tunable, and robust source of narrow-band photon pairs at the ^{87}Rb $D1$ line*, *Optics Express* **28**, 3159 (2020).
- ⁵ K. Heshami, D. G. England, P. C. Humphreys, P. J. Bustard, V. M. Acosta, J. Nunn, and B. J. Sussman, *Quantum memories: emerging applications and recent advances*, *Journal of Modern Optics* **63**, 2005 (2016).

Fractional boundary charges with quantized slopes in interacting one- and two-dimensional systems

Katharina Laubscher,¹ Clara S. Weber,² Dante M. Kennes,^{2,3} Mikhail Pletyukhov,² Herbert Schoeller,² Daniel Loss,¹ and Jelena Klinovaja¹

¹*Department of Physics, University of Basel, Klingelbergstrasse 82, CH-4056 Basel, Switzerland*

²*Institut für Theorie der Statistischen Physik, RWTH Aachen, 52056 Aachen, Germany and JARA - Fundamentals of Future Information Technology*

³*Max Planck Institute for the Structure and Dynamics of Matter, Center for Free Electron Laser Science, 22761 Hamburg, Germany*

In this work,¹ we study fractional boundary charges (FBCs) in strongly interacting systems. We study (i) strongly interacting nanowires in the presence of a spatially modulated potential and (ii) the fractional quantum Hall effect (FQHE) at odd filling factors in a Corbino disk geometry threaded by an external flux. In both cases, the FBCs show universal features that do not depend on microscopic details of the system. In the nanowire (FQHE) case, we find that the FBC depends linearly on the phase offset of the potential (the external flux) with a universally quantized slope. Furthermore, different possible values of the FBC at a fixed phase offset (fixed flux) label different degenerate ground states that cannot be connected adiabatically. These results allow for several simple ways to probe strongly interacting phases via boundary charge measurements.

I. INTRODUCTION

Charge fractionalization in topologically nontrivial systems is a recurring theme in modern condensed matter physics. One manifestation of this phenomenon is the emergence of well-defined fractional charges in the ground state of topological insulators. Early examples include the Jackiw-Rebbi² and Su-Schrieffer-Heeger³ models, where domain walls between topologically non-equivalent phases bind fractional charges that are quantized due to symmetry. Similarly, fractional boundary charges (FBCs) can accumulate at the boundaries of topological insulators. Importantly, the possible presence of edge states influences the total boundary charge only by an integer number, while the *fractional* part of the boundary charge contains contributions from all extended states and is directly related to bulk properties via the Zak-Berry phase. Furthermore, while the presence of symmetries leads to a quantization of the FBC in rational units,⁴ certain *universal* features of the FBC persist even in the absence of symmetries. For generic 1D tight-binding models with periodically modulated on-site potentials, it was shown that the FBC depends linearly on the phase offset of the potential with a universally quantized slope even in the presence of disorder.^{5–8} Furthermore, this slope can be directly related to the Hall conductance in the 2D integer quantum Hall effect.⁶

While the above results on FBCs were mostly obtained for non- or weakly interacting systems, the aim of this work is to study the universal properties of the FBC in strongly interacting systems. For this, we consider two main examples that will be discussed in the following.

II. FBCS IN STRONGLY INTERACTING NANOWIRES

First, we consider a 1D nanowire with a periodic potential of the form $V_m(x) = 2V_m \cos(2mk_F x + \alpha)$, where

k_F is the Fermi momentum, m an integer, and α a phase offset. For $m = 1$, a charge density wave (CDW) gap is opened at the Fermi level even in the non-interacting limit. In the presence of sufficiently strong interactions, a gap can also be opened for $m > 1$. We now consider a semi-infinite nanowire with a single edge at $x = 0$. Using a bosonized description of the strongly interacting nanowire, we then calculate the excess charge accumulating at the edge of the wire at $x = 0$. We find that this boundary charge is given by

$$Q_B^{1D} = \frac{\alpha}{2\pi m} + \frac{p}{m} \pmod{1} \quad (1)$$

in units of the electron charge e and where p is an integer. This result has several interesting features: Firstly, we see that the FBC is a linear function of α with a slope of $1/2\pi m$. For $m = 1$, this agrees with the result that was previously obtained for noninteracting systems.⁶ Secondly, for fixed α , there are m different values for the FBC, $Q_B^{1D} - \alpha/2\pi m \in \{0, 1/m, \dots, (m-1)/m\}$. For $m > 1$, we therefore find that the ground state is m -fold degenerate. Thirdly, these different ground states cannot be connected to one another under adiabatic evolution of α . As such, a given branch of the FBC is $2\pi m$ -periodic, while the Hamiltonian is 2π -periodic. Finally, we emphasize that these results do not depend on microscopic details such as the exact strength of the electron-electron interactions, but hold whenever the CDW term is relevant in the renormalization group (RG) sense.

III. FBCS IN THE FRACTIONAL QUANTUM HALL EFFECT

Next, we extend our considerations to a two-dimensional electron gas (2DEG) in the FQHE regime at odd filling factors $\nu = 1/(2l + 1)$, where l is an integer. In order to treat the strongly interacting system

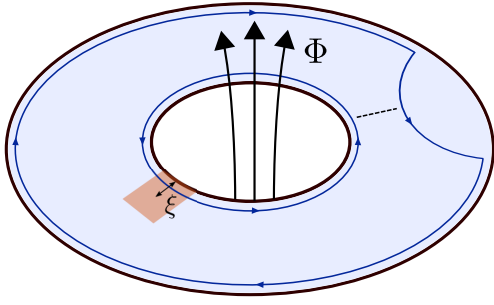


FIG. 1: Corbino disk in the FQHE regime threaded by an external flux Φ . The FBC is measured in the red region, which extends into the bulk to the order of a few edge state localization lengths ξ . In the presence of a constriction, indicated by the dashed line, tunneling of fractional charges between the chiral edge states (blue lines) is allowed.

analytically, we make use of a coupled-wires construction to model the FQHE.⁹ We arrange the wires in a cylinder geometry and study the FBC in the presence of an external flux Φ threading the cylinder. We find that the FBC can be calculated from the 1D boundary charge $Q_{B,n}^{1D}$ of each individual wire as

$$Q_B^{2D} = \sum_n Q_{B,n}^{1D} = \frac{\Phi\nu e}{2\pi\hbar} + p\nu \pmod{1} \quad (2)$$

in units of the electron charge e and where p is again an integer. Thus, the FBC depends linearly on Φ with a slope that is quantized in units of $\nu e/h$. At fractional filling $\nu = 1/(2l+1)$ with $l > 0$, this slope is $(2l+1)$ times smaller than in the integer case $l = 0$. Furthermore, there are $2l+1$ different branches of the FBC that cannot be connected under adiabatic evolution of Φ . Finally, the Hall conductance can be obtained from the FBC via $\sigma_{xy} = e\dot{Q}_B^{2D}/\dot{\Phi} = e^2\nu/h$.

The sample geometry described above can be realized in a Corbino disk, see Fig. 1. The FBC is then accessible using, e.g., scanning tunneling microscopy (STM) techniques. This allows for several interesting ways to probe the FQHE: Firstly, observing the slope of the linear flux dependence allows one to probe the filling factor, see Eq. (2). Moreover, as Φ is varied adiabatically, the FBC will be $(2\pi/\nu)$ -periodic with a jump of size unity

occurring at a particular value of Φ . Secondly, the different branches of the FBC can be connected if fractional charges are allowed to tunnel between opposite boundaries due to, e.g., a constriction, see again Fig. 1. By measuring the FBC repeatedly in the presence of a constriction, one finds that it can take $2l+1$ different values, reflecting the $(2l+1)$ -fold ground state degeneracy. Similarly, if one now observes the evolution of the FBC with Φ , also jumps of fractional size $s/(2l+1)$, where $s = 1, \dots, 2l$ is another integer, can be observed when the system switches from one ground state to another. Thus, boundary charge measurements open up a direct way to probe the fractionalization of charges in the FQHE and, most importantly, allow for a direct experimental verification of the ground state degeneracy.

IV. CONCLUSIONS

We have studied FBCs in strongly interacting CDW-modulated nanowires and in Corbino disks in the FQHE regime at odd filling factors threaded by an external flux. In both cases, the FBC displays universal features that do not depend on microscopic details of the models such as the exact values of the interaction parameters. The observation of these features is well within experimental reach and opens up a promising route to probe strongly interacting phases via FBCs.

Acknowledgments

This work was supported by the Deutsche Forschungsgemeinschaft via RTG 1995, the Swiss National Science Foundation (SNSF) and NCCR QSIT and by the Deutsche Forschungsgemeinschaft (DFG, German Research Foundation) under Germany's Excellence Strategy - Cluster of Excellence Matter and Light for Quantum Computing (ML4Q) EXC 2004/1 - 390534769. We acknowledge support from the Max Planck-New York City Center for Non-Equilibrium Quantum Phenomena. Simulations were performed with computing resources granted by RWTH Aachen University under project thes0753. Funding was received from the European Union's Horizon 2020 research and innovation program (ERC Starting Grant, Grant Agreement No. 757725).

¹ K. Laubscher, C. S. Weber, D. M. Kennes, M. Pletyukhov, H. Schoeller, D. Loss, and J. Klinovaja, Phys. Rev. B **104**, 035432 (2021).

² R. Jackiw and C. Rebbi, Phys. Rev. D **13**, 3398 (1976).

³ W. P. Su, J. R. Schrieffer, and A. J. Heeger, Phys. Rev. Lett. **42**, 1698 (1979).

⁴ M. Pletyukhov, D. M. Kennes, K. Piasotski, J. Klinovaja, D. Loss, and H. Schoeller, Phys. Rev. Research **2**, 033345 (2020).

⁵ J.-H. Park, G. Yang, J. Klinovaja, P. Stano, and D. Loss,

Phys. Rev. B **94**, 075416 (2016).

⁶ M. Thakurathi, J. Klinovaja, and D. Loss, Phys. Rev. B **98**, 245404 (2018).

⁷ M. Pletyukhov, D. M. Kennes, J. Klinovaja, D. Loss, and H. Schoeller, Phys. Rev. B **101**, 165304 (2020).

⁸ M. Pletyukhov, D. M. Kennes, J. Klinovaja, D. Loss, and H. Schoeller, Phys. Rev. B **101**, 161106(R) (2020).

⁹ J. C. Y. Teo and C. L. Kane, Phys. Rev. B **89**, 085101 (2014).

Precision spectroscopy and coherent manipulation of single trapped molecular ions

Mikolaj Franciszek Roguski,¹ Aleksandr Shlykov,¹ Mudit Sinhal,¹ Ziv Meir,¹ and Stefan Willitsch¹

¹*Chemistry Department, University of Basel, CH-4056 Basel, Switzerland*

Trapped atoms and atomic ions are among the best-controlled quantum systems which find widespread applications in quantum science. However, similar exquisite control over molecules has remained elusive so far due to their complex energy-level structure with additional rotational and vibrational degrees of freedom. We employ a quantum-logic protocol that uses a single co-trapped atomic ion as a probe for the molecular state. Specifically, we demonstrate a quantum non-demolition state detection on N_2^+ with fidelities exceeding 99%. Our detection technique does not destroy the molecule or the molecular state itself. The present method paves a way for the implementation of molecular qubits with excellent coherence properties, for establishing new frequency standards in the mid-IR regime, for investigating state-to-state dynamics of chemical reactions and for exploring beyond-standard-model physics by tracking a possible temporal variation of fundamental constants.

I. INTRODUCTION

For the past decades, cold trapped atoms and atomic ions have emerged as one of the best-controlled quantum systems and found their way to widespread applications in quantum science. They are used to form a basis for the most precise clocks,¹ to perform quantum simulations² and to compute quantum algorithms.³ Similar degree of control over molecules and molecular ions is still missing. There are challenges in adapting techniques routinely used for atomic species to molecules because their dense energy level structure results in the lack of optical cycling transitions that are commonly used for cooling and detection. However, it would be desirable to explore a broad range of transitions with frequencies covering a frequency range from MHz regime up to 100s of THz, some with very good coherence properties, that comes from additional rotational and vibrational degrees of freedom in molecules.

N_2^+ is an excellent candidate for a molecular clock and a molecular qubit with outstanding coherence properties.⁴ In particular, transitions within the electronic ground state have very low systematic Stark and black body radiation shifts due to lack of permanent dipole moment. In N_2^+ molecules, many magnetically insensitive dipole-forbidden transitions were identified in the different radiofrequency, microwave and infrared domains with sensitivities as small as 20 mHz/mG.⁴

In our experiment, we use a co-trapped atomic Ca^+ ion that serves as a coolant and is used to probe the internal state of a molecule. We demonstrate a quantum logic protocol that detects the state of N_2^+ ions while conserving its internal state. It is an important step towards full coherent control over a molecular state.

II. PREPARATION OF N_2^+ IONS IN THEIR INTERNAL AND EXTERNAL GROUND STATE

N_2^+ molecular ions are created in their electronic, vibrational and rotational ground state by Resonance-Enhanced Multi-Photon Ionisation (REMPI)⁵ from a molecular beam source of rotationally cold neutral molecules. Single molecular ions are trapped in a lin-

ear quadruple radio-frequency trap and sympathetically cooled by a pre-loaded cloud of atomic Ca^+ ions for fast and efficient cooling, followed by reduction of excess atomic ions until a single molecular ion and a single atomic ion remain in the trap.⁶ We use a resolved side-band cooling technique on the atomic ion that sympathetically cools its molecular neighbour via Coulomb interaction. It results in a Coulomb crystal consisting of Ca^+ and N_2^+ in the motional ground state with a final motional quantum number along the cooling axis of $n = 0.02$.

III. MOLECULAR QUANTUM NON-DEMOLITION STATE DETECTION

In the past, readout of the state of a molecule involved the destruction of the state or the molecule's chemical identity.⁷ Here, we demonstrate a quantum *non-demolition* state detection on N_2^+ with fidelities exceeding 99% without destroying the molecular state.⁸ It is done by mapping the internal state of a molecule on the motional mode of the Coulomb crystal, and then probing the motional state on the co-trapped auxiliary atomic ion.

We use an optical-dipole force (ODF) to excite the coherent motion of the ion-molecule crystal. ODF is implemented via the AC Stark shift. The ODF strength, and hence the amplitude of the coherent motion, depends on the molecular state through the frequency detuning of the ODF laser beam from resonance in the molecule. Two counter-propagating laser beams, with a relative detuning corresponding to the frequency of a motional mode of the two-ion crystal, generate a running 1D optical lattice. This running lattice gives rise to an optical dipole force on the molecule depending on its state. Experiments are performed @ 787.5 nm at which wavelength a molecule in the ro-vibronic ground state experiences a much larger ODF amplitude compared to other states.

As an extension to the current state detection technique, we were also able to extract hyperfine structure information of the ion with phase-sensitive state detection. By interrogation of the relative forces between the atomic and molecular ion, we retrieved a relative phase

shift between them. Through comparison to the theoretical evaluation of the energy level system, identification of molecular states that experience similar ODF amplitudes was possible.⁹

IV. ELECTRONIC QUANTUM-LOGIC SPECTROSCOPY OF N_2^+

As an application of our state detection technique, we performed force spectroscopy on the ro-vibronic ground state transition of N_2^+ molecule. Since the amplitude of the AC Stark shift is (inversely) proportional to the detuning, we were able to extract spectroscopic information about the centre frequency of a molecular transition.⁸

V. OUTLOOK

The present method is a step towards a full coherent control and state-readout of molecular ions. Cur-

rently, we are implementing precision-spectroscopy measurements on narrow quadruple transitions. It can be used for creating a molecular clock that would serve as a mid-IR frequency standard of importance for modern communication. It will also lead to the implementation of molecular qubits with excellent coherence properties. Furthermore, achieving full control over a single molecule will be useful for investigating the dynamics of chemical reactions on a single collision level. Last but not least, molecular transitions are predicted to be excellent candidates for exploring beyond-standard-model physics by tracking a possible temporal variation of fundamental constants.

Acknowledgments

We acknowledge funding from the Swiss National Science Foundation as part of the National Centre of Competence in Research, Quantum Science and Technology (NCCR-QSIT) and the University of Basel.

-
- ¹ C.-w. Chou, D. Hume, J. Koelemeij, D. J. Wineland, and T. Rosenband, *Frequency comparison of two high-accuracy Al^+ optical clocks*, Physical review letters **104**, 070802 (2010).
- ² R. Blatt and D. Wineland, *Entangled states of trapped atomic ions*, Nature **453**, 1008 (2008).
- ³ T. Monz, D. Nigg, E. A. Martinez, M. F. Brandl, P. Schindler, R. Rines, S. X. Wang, I. L. Chuang, and R. Blatt, *Realization of a scalable shor algorithm*, Science **351**, 1068 (2016).
- ⁴ K. Najafian, Z. Meir, and S. Willitsch, *From megahertz to terahertz qubits encoded in molecular ions: theoretical analysis of dipole-forbidden spectroscopic transitions in N_2^+* , Physical Chemistry Chemical Physics **22**, 23083 (2020).
- ⁵ A. Gardner, T. Softley, and M. Keller, *Multi-photon ionization spectroscopy for rotational state preparation of N_2^+* ,

Scientific reports **9**, 1 (2019).

- ⁶ Z. Meir, G. Hegi, K. Najafian, M. Sinhal, and S. Willitsch, *State-selective coherent motional excitation as a new approach for the manipulation, spectroscopy and state-to-state chemistry of single molecular ions*, Faraday discussions **217**, 561 (2019).
- ⁷ M. Germann, X. Tong, and S. Willitsch, *Observation of electric-dipole-forbidden infrared transitions in cold molecular ions*, Nature Physics **10**, 820 (2014).
- ⁸ M. Sinhal, Z. Meir, K. Najafian, G. Hegi, and S. Willitsch, *Quantum-nondemolition state detection and spectroscopy of single trapped molecules*, Science **367**, 1213 (2020).
- ⁹ K. Najafian, Z. Meir, M. Sinhal, and S. Willitsch, *Identification of molecular quantum states using phase-sensitive forces*, Nature Communications **11**, 1 (2020).

Development of a millikelvin STM for single spin resonance

Daria Sostina,¹ Wantong Huang,² David Collomb,² Christoph Sürgers,² Philip Willke,² and Wolfgang Wernsdorfer^{1,2}

¹*Institute for Quantum Materials and Technologies (IQMT),
Karlsruhe Institut of Technology, Karlsruhe, Germany*

²*Physics Institut (PHI), Karlsruhe Institut of Technology, Karlsruhe, Germany*

In the last decade detection and manipulation of spins at the atomic scale has been achieved by combining techniques like electron spin resonance (ESR) with scanning tunneling microscopy (STM). Here we demonstrate an ultra-high vacuum (UHV) STM operational at milliKelvin (mK) temperatures capable of ESR. By implementing radio frequency compatible cabling, we achieve appreciable RF amplitudes at the tunneling junction while maintaining mK base temperature.

I. INTRODUCTION

Coherent control of single atoms and molecules on surfaces has attracted a lot of attention over the past few years aiming to create new solid-state architectures for magnetic sensing and quantum information processing. Their design requires characterization of the geometric, electronic, and magnetic properties of individual spin centers on surfaces and knowledge about the environment of a quantum object to protect it from noise and energy exchange. One of the powerful tools for such studies is the recently realized combination of electron spin resonance and scanning tunneling microscopy (ESR-STM) [1]. However, crucial properties of potential quantum spins such as the phase coherence time T_2 and the spin relaxation time T_1 remain constrained by the instrumental limits of existing microscopes, since both T_1 and T_2 are affected by the proximity to the metallic electrodes of tip and substrate providing thermally excited electrons [2-3]. Consequently, higher T_1 and T_2 could be attained by achieving lower temperatures. Another advantage of the DR-STM system is increased thermally initialized ground state population which would allow us to exploit different object for quantum manipulations - nuclear spins. Moreover, since the ground state population as well as T_1 scales with the resonance frequency [2], better RF transmission at high frequencies is also desired for ESR-STM.

II. DILUTION REFRIGERATOR

Here, we present the design and implementation of a unique dilution refrigerator scanning tunneling microscope for electron spin resonance, lowering the temperature to the milliKelvin range for ESR-STM. The design is based on the Sionludi table top dilution refrigerator, which was previously used for the operation of quantum algorithms on single molecules [4]. Such design is advantageous compared to existing ESR-STM systems in the base temperature and time required for cooling down. Hence, we were able to reach 75 mK of sample temperature and maintain it with additional heat load from

radio frequency (RF) radiation applied to the junction and coarse motion of the sample stage. A closed helium 4 cycle implemented using pulse tube liquefier allows us to maintain millikelvin base temperature without refill of liquid helium.

In order to ensure vibrational isolation of tunneling junction several stages of active mechanical damping were designed. It was possible to mount an external system of springs and flexible bellow due to full separation of UHV chamber inside Sionludi dilution fridge. Additionally a 4K stage of the fridge hosts an array of permanent magnets providing eddy current damping.

III. SCANNING TUNNELING MICROSCOPE

It was found that spin relaxation time increases with external magnetic field [2]. Therefore a fast sweep dry vector magnet was designed for our STM system capable of creating 1.5T of magnetic field out of plane and 1T in plane field. It was possible to dramatically decrease the size of magnetic coils by inverting the traditional for STM scanning heads position of coarse motion piezos. This solution allowed us to keep vacuum chamber containing sample and, hence, tunneling junction very small in diameter.

However, since the resonance frequency of ESR scales linearly with magnetic field according to the Zeeman splitting, RF transmission at high frequencies is also required. In the table-top dilution refrigerator the RF cabling can be easily optimized due to the fast cooling of the cryostat (3h) allowing to potentially improve the transmission function. In order to accommodate GHz excitation with sufficient RF amplitude, we adapted high frequency low loss cabling in UHV environment to establish tip transmission line. A semi rigid copper cable was used in both dilution refrigerator and UHV chamber hosting the STM. All in-situ connections, including the direct connections to the sample and tip, were made with SMP and SMA connectors rated to 40 GHz. As a result our new type of DR-STM will path the way to establish quantum logic operations and quantum entanglement on single spin centers on surfaces.

Quantum Simulations: Setting up increasingly complex quantum systems - atom by atom

Apurba Das, Deviprasath Palani, Florian Haße, Lennart Guth, Ingolf Kaufmann, Amir Mohammadi, Ulrich Warring, Tobias Schaetz

Physikalisches Institut, Universität Freiburg, Hermann-Herder-Straße 3, D-79104 Freiburg, Germany

Systems of individually trapped atomic ions are a well studied platform for quantum information processing, quantum metrology, quantum simulation. Coherent control over such system with high fidelities have been demonstrated. Re-configurable and fully controllable quantum systems have been successfully set up with individual atoms in multidimensional arrangements. Building on this, we adopt another method to enable broadband cooling of an array of trapped ions to enable more efficient control.

Single trapped atoms exhibit internal degrees of freedom, i.e., discrete electronic states and external degrees of freedom, i.e., continuous variable states. They are isolated from their environment enabling precise control and long coherence time. Tremendous advancements in research on individual trapped atoms in the last 30 years allow to work on qubit states¹, simulate intractable models from quantum physics², prepare method for database searching³ and build one of the most precise atomic clocks⁴ etc. Entangling gate fidelities higher than 99.99%⁵ have already been achieved. Building on this success, we extend our system to manipulate multiple atoms at very low temperatures to build up more complex systems with a high level of control⁶. Customized trap architectures with suitable local and global control fields enable us to set up and tune increasingly complex quantum systems^{7,8}. We tailor the external parameters to engineer interactions between constituents. For individual state control and coupling of internal and

external degrees of freedom in the system, we typically implement two photon stimulated Raman transition⁹. In our future work, in addition to our established control features, we want to bring ground state cooling based on electromagnetically-induced-transparency¹⁰ to enable broadband cooling of multiple modes to deterministically prepare the system to its global ground state. This will allow us to prepare the atom arrays for further quantum operations more efficiently. Here we present required technical developments: customized VECSEL¹¹ systems.

Acknowledgments

This research work is being performed under QUSTEC programme in the group of Prof. Dr. Tobias Schätz, Institute of Physics, Freiburg University. The QUSTEC programme has received funding from the European Union's Horizon 2020 research and innovation programme under the Marie Skłodowska-Curie grant agreement number 847471.

¹ T. Schaetz, Nature **528**, 337 (2015), ISSN 1476-4687.

² A. Trabesinger, Nature Physics **8**, 263 (2012), ISSN 1745-2481.

³ L. K. Grover, Phys. Rev. Lett. **79**, 4709 (1997).

⁴ N. Huntemann, C. Sanner, B. Lipphardt, C. Tamm, and E. Peik, Phys. Rev. Lett. **116**, 063001 (2016).

⁵ T. P. Harty, D. T. C. Allcock, C. J. Ballance, L. Guidoni, H. A. Janacek, N. M. Linke, D. N. Stacey, and D. M. Lucas, Phys. Rev. Lett. **113**, 220501 (2014).

⁶ U. Warring, F. Hakelberg, P. Kiefer, M. Wittemer, and T. Schaetz, Advanced Quantum Technologies **3**, 1900137 (2020).

⁷ P. Kiefer, F. Hakelberg, M. Wittemer, A. Bermúdez,

D. Porras, U. Warring, and T. Schaetz, Phys. Rev. Lett. **123**, 213605 (2019).

⁸ F. Hakelberg, P. Kiefer, M. Wittemer, U. Warring, and T. Schaetz, Phys. Rev. Lett. **123**, 100504 (2019).

⁹ M. Mielenz, H. Kalis, M. Wittemer, F. Hakelberg, U. Warring, R. Schmied, M. Blain, P. Maunz, D. L. Moehring, D. Leibfried, et al., **7**, ncomms11839 (2016).

¹⁰ G. Morigi, J. Eschner, and C. H. Keitel, Phys. Rev. Lett. **85**, 4458 (2000).

¹¹ S. C. Burd, D. T. C. Allcock, T. Leinonen, J. P. Penttinen, D. H. Slichter, R. Srinivas, A. C. Wilson, R. Jördens, M. Guina, D. Leibfried, et al., Optica **3**, 1294 (2016).

Interpretable and unsupervised phase classification

Julian Arnold,¹ Frank Schäfer,¹ Martin Žonda,^{2,3} and Axel U. J. Lode²

¹Department of Physics, University of Basel, Klingelbergstrasse 82, 4056 Basel, Switzerland

²Institute of Physics, Albert-Ludwigs-Universität Freiburg,

Hermann-Herder-Strasse 3, 79104 Freiburg im Breisgau, Germany

³Department of Condensed Matter Physics, Faculty of Mathematics and Physics, Charles University, Ke Karlovu 5, Praha 2 CZ-121 16, Czech Republic

Phase diagrams and phase transitions are of paramount importance to physics. While many-body systems have a large number of degrees of freedom, their phases are usually characterized by a small set of physical quantities like order parameters. For instance, the thermal phase transition in the celebrated two-dimensional classical Ising model¹ is revealed by the magnetization. However, in general the identification of phases and their order parameters is a complex problem which involves a large state space. Machine learning methods are apt for this task²⁻⁶ as they can deal with large data sets and efficiently extract information from them. Ideally, such machine learning methods should not require prior knowledge about the phases, e.g., in the form of spin configurations that are labelled by their correct phase, or even the number of distinct phases. That is, the methods should be unsupervised^{2,4,7,8}.

Yet, they should also allow for a straightforward physical insight into the character of phases: We desire *interpretable* methods for which we have an intuitive understanding why they yield a given phase classification, i.e., whose decision making is fully explainable. Significant progress in this direction has been made recently⁹⁻¹¹, but many open issues regarding the interpretability of phase classification methods remain.

A good example of both progress in the field of unsupervised phase classification and relevant challenges regarding interpretability is the *prediction-based method* introduced in Ref.⁷. This approach is based on a predictive model $m : x \rightarrow \hat{p}(x)$ trained to infer the parameters p of a physical system from input data x – obtained by experimental measurements or numerical simulations – that characterize the system’s state. Intuitively, the predictions for the system parameters \hat{p} in the prediction-based method change most strongly near phase boundaries. Consequently, the vector-field divergence of the deviations of the predicted system parameters with respect to their true values serves as an indicator of phase transitions (see label I in Fig. 1).

The prediction-based method was hitherto successfully applied to symmetry-breaking⁷, driven-dissipative⁷, quantum⁸, and topological phase transitions^{8,12} in various systems. The method requires a predictive model with sufficient expressive power to resolve different phases. Without prior system knowledge deep neural networks (DNN) constitute a good choice due to their capability of approximating arbitrary target functions efficiently. However, the more expressive a machine learning

model, such as a DNN, the more difficult it is to interpret the underlying functional dependence of the predictions on the input data. Thus, the prediction-based method typically functions as a black-box model which allow for a given phase classification task to be solved, but whose internal workings remain a mystery to the user.

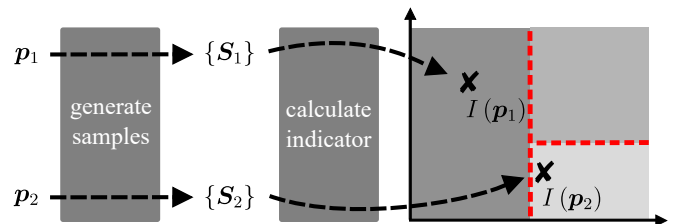


FIG. 1: Our workflow to predict a phase diagram with indicators I for phase transitions. Here, we illustrate the procedure for a two-dimensional parameter space: The parameter space is sampled on a grid which yields a set of points $\{p_i\}$ of fixed system parameters. At each such point p_i a set of samples $\{S_i\}$ is generated. Based on these samples, a scalar indicator for phase transitions, $I(p_i)$, is calculated. This indicator highlights the boundaries (red) between phases (grey). Different unsupervised phase classification schemes, such as the prediction-based method and mean-based method, are established via different choices of indicators.

In our contribution¹³, we render the prediction-based method interpretable by deriving the form of its optimal predictions as a function of the input data. Therefore, we gain a complete understanding of the resulting phase classification and the associated values of the indicator for phase transitions. These insights pave the way for the key result of our work: a novel interpretable and unsupervised phase classification method referred to as the *mean-based method*. The method requires input data that characterizes the state of a physical system for various choices of system parameters in a representation that is invariant under the system’s symmetry group. For each sampled point in parameter space, one calculates the magnitude of the difference between mean input features of neighbouring points in parameter space. This quantity serves as an alternative indicator of phase transitions and reveals the underlying phase diagram, because it is largest at phase boundaries (see Fig. 1). As such, the mean-based method is conceptually simple, computationally cheap, and generic in nature. In particular, the computation of its indicator does not rely on a black-box

predictive model and allows for this data-driven method to be directly explainable.

As a physical system, we considered the two-dimensional spinless Falicov-Kimball model (FKM)¹⁴ described by

$$\mathcal{H} = -t \sum_{\langle ij \rangle} (d_i^\dagger d_j + d_j^\dagger d_i) + U \sum_i d_i^\dagger d_i f_i^\dagger f_i. \quad (1)$$

Here, t is the hopping integral, U is the on-site interaction strength, f_i^\dagger (f_i) and d_i^\dagger (d_i) are the creation (annihilation) operators of heavy (f) and light (d) fermions at lattice site i . The number operator $n_{f,i} = f_i^\dagger f_i$ commutes with the Hamiltonian for all i , such that we can replace it by its eigenvalues $w_i \in \{0, 1\}$. The ground state is thus determined by the classical f -particle configuration $\{w_i\}$ that minimizes the system energy. We focus on the “neutral” case¹⁵, characterized by an equal density of heavy and light particles $\rho = N_f/L^2 = N_d/L^2$. Here, N_f (N_d) is the total number of heavy (light) particles and L is the linear size of the square two-dimensional lattice with periodic boundary conditions.

The FKM is used to address a broad range of con-

temporary physical problems, such as fractionalized metals¹⁶, topological phenomena at finite temperature¹⁷, or various quasiparticles¹⁸. Moreover, it serves as a standard test bed for the development of methods in the context of strongly correlated systems^{19–21}. Hitherto, the classification of the ground-state phases in the FKM was a manual and – due to the richness of the phase diagram – lengthy and cumbersome task. This complexity makes the FKM a challenging example for phase classification: To the best of our knowledge no phase classification method has been successfully applied to systems featuring a phase diagram with such a plethora of different orderings so far.

We find that the mean-based method is an excellent tool to classify the ground-state phases of the FKM. Moreover, the simplicity of method allows for direct insights into the relevant change in order governing each detected phase transition. Due to the flexibility of the mean-based method we infer that applications to arbitrary phase diagrams featuring, e.g., quantum or topological phase transitions are feasible. In particular, applications to quantum-classical systems such as the FKM and its numerous generalizations are straightforward.

-
- ¹ L. Onsager, *Crystal Statistics. I. A Two-Dimensional Model with an Order-Disorder Transition*, Phys. Rev. **65**, 117 (1944).
- ² L. Wang, *Discovering phase transitions with unsupervised learning*, Phys. Rev. B **94**, 195105 (2016).
- ³ J. Carrasquilla and R. G. Melko, *Machine learning phases of matter*, Nat. Phys. **13**, 431 (2017).
- ⁴ E. P. Van Nieuwenburg, Y.-H. Liu, and S. D. Huber, *Learning phase transitions by confusion*, Nat. Phys. **13**, 435 (2017).
- ⁵ B. S. Rem, N. Käming, M. Tarnowski, L. Asteria, N. Fläschner, C. Becker, K. Sengstock, and C. Weitenberg, *Identifying quantum phase transitions using artificial neural networks on experimental data*, Nat. Phys. **15**, 917 (2019).
- ⁶ A. Bohrdt, C. S. Chiu, G. Ji, M. Xu, D. Greif, M. Greiner, E. Demler, F. Grusdt, and M. Knap, *Classifying snapshots of the doped Hubbard model with machine learning*, Nat. Phys. **15**, 921 (2019).
- ⁷ F. Schäfer and N. Lörch, *Vector field divergence of predictive model output as indication of phase transitions*, Phys. Rev. E **99**, 062107 (2019).
- ⁸ E. Greplova, A. Valenti, G. Boschung, F. Schäfer, N. Lörch, and S. D. Huber, *Unsupervised identification of topological phase transitions using predictive models*, New J. Phys. **22**, 045003 (2020).
- ⁹ C. Casert, T. Vieijra, J. Nys, and J. Ryckebusch, *Interpretable machine learning for inferring the phase boundaries in a nonequilibrium system*, Phys. Rev. E **99**, 023304 (2019).
- ¹⁰ S. Blücher, L. Kades, J. M. Pawłowski, N. Strodthoff, and J. M. Urban, *Towards novel insights in lattice field theory with explainable machine learning*, Phys. Rev. D **101**, 094507 (2020).
- ¹¹ A. Dawid, P. Huembeli, M. Tomza, M. Lewenstein, and A. Dauphin, *Phase detection with neural networks: interpreting the black box*, New J. Phys. **22**, 115001 (2020).
- ¹² J. Singh, M. S. Scheurer, and V. Arora, *Conditional generative models for sampling and phase transition indication in spin systems*, SciPost Phys. **11**, 43 (2021).
- ¹³ J. Arnold, F. Schäfer, M. Žonda, and A. U. J. Lode, *Interpretable and unsupervised phase classification*, Phys. Rev. Res. **3**, 033052 (2021).
- ¹⁴ L. M. Falicov and J. C. Kimball, *Simple Model for Semiconductor-Metal Transitions: SmB₆ and Transition-Metal Oxides*, Phys. Rev. Lett. **22**, 997 (1969).
- ¹⁵ R. Lemański, J. K. Freericks, and G. Banach, *Stripe Phases in the Two-Dimensional Falicov-Kimball Model*, Phys. Rev. Lett. **89**, 196403 (2002).
- ¹⁶ M. Hohenadler and F. F. Assaad, *Fractionalized Metal in a Falicov-Kimball Model*, Phys. Rev. Lett. **121**, 086601 (2018).
- ¹⁷ M. Gonçalves, P. Ribeiro, R. Mondaini, and E. V. Castro, *Temperature-Driven Gapless Topological Insulator*, Phys. Rev. Lett. **122**, 126601 (2019).
- ¹⁸ A. Kauch, P. Pudleiner, K. Astleithner, P. Thunström, T. Ribic, and K. Held, *Generic Optical Excitations of Correlated Systems: π -tons*, Phys. Rev. Lett. **124**, 047401 (2020).
- ¹⁹ T. Maier, M. Jarrell, T. Pruschke, and M. H. Hettler, *Quantum cluster theories*, Rev. Mod. Phys. **77**, 1027 (2005).
- ²⁰ J. K. Freericks, V. M. Turkowski, and V. Zlatić, *Nonequilibrium Dynamical Mean-Field Theory*, Phys. Rev. Lett. **97**, 266408 (2006).
- ²¹ H. Aoki, N. Tsuji, M. Eckstein, M. Kollar, T. Oka, and P. Werner, *Nonequilibrium dynamical mean-field theory and its applications*, Rev. Mod. Phys. **86**, 779 (2014).

Corner and Edge Charges in Systems with Chiral Hinge Modes

Yuhao Zhao, Katharina Laubscher, Daniel Loss, Jelena Klinovaja¹

¹*Department of Physics, University of Basel, CH-4056 Basel, Switzerland*

I. ABSTRACT

The higher order topological insulator (HOTI) is an N -dimensional insulator, which has gapless boundary states emerging at its $N - d$ dimensional boundaries for $d > 1$. [1] The appearance of the higher order topological phases in an N -dimensional system is usually accompanied by the filling anomalies in its corresponding $N - 1$ dimensional system obtained by dimensional reduction. [2] These filling anomalies are denoted as the corner (or edge) charges according to their locations. In previous work [3], the fractional boundary charges in 1D are related to the integer Hall conductance in 2D system. In this work, we show that the topological properties in the 3D system can be revealed by the behavior of the filling anomalies with respect to an external parameter in its 2D counterpart. Specifically, the corner charge in the 2D plane reduced from a 3D system with chiral hinge modes changes linearly with respect to an external flux. We further argue that this linear behavior is a general property for all 3D HOTIs with chiral hinges modes, and the constant slope of the linear change can serve as a topological invariant characterizing 3D HOTIs with chiral hinge modes.

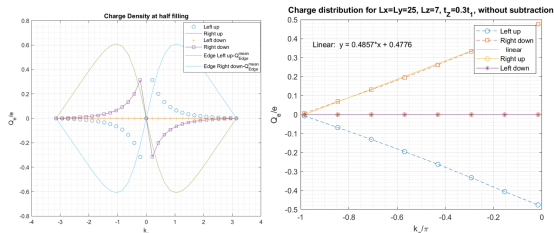


FIG. 1. The behavior of the corner and edge charges in different setups. The system is taken from [4], and is reduced to 2D by closing the boundary in z -direction. Left: non-linear behavior of the corner and edge charges with respect to k_z while there is only one unit cell along z -direction. The edge charges are marked by solid curves while the dotted lines represent the corner charges. Additional to the non-linear behavior, the corner charges jump by one at $k_z = 0$. Right: after increasing the number of the unit cells in z -direction, the edge charges disappear and the linear behavior of the corner charges is spotted.

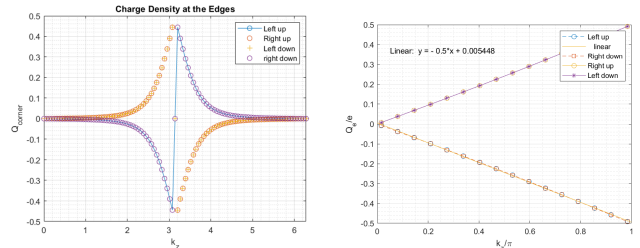


FIG. 2. We show the behavior of the corner charges in another toy model with different setups. Left: non-linear behavior of the corner and edge charge with respect to k_z with one unit cell along z -direction. In this model, there is no edge charge and the corner charges are marked by dotted lines. The corner charges manifest similar pattern in both HOTI systems. Right: linear behavior appears after increasing the number of the unit cells in z -direction.

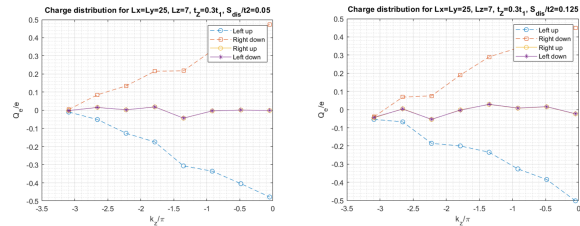


FIG. 3. The disorder is added into the system from [4]. We can still observe linear behavior up to some oscillations as long as the system remains in the topological non-trivial regime.

ACKNOWLEDGMENTS

We would like to thank Flavio Ronetti and Zhe Hou for helpful and fruitful discussions. This work was supported by the Swiss National Science Foundation and NCCR QSIT. Funding was received from the European Union's Horizon 2020 research and innovation program (ERC Starting Grant, Grant Agreement No. 757725).

[1] W. A. Benalcazar, B. A. Bernevig, and T. L. Hughes, Electric multipole moments, topological multipole moment pumping, and chiral hinge states in crystalline insulators, *Physical Review B* **96**, 245115 (2017).
 [2] L. Trifunovic, Bulk-and-edge to corner correspondence, *Physical Review Research* **2**, 043012 (2020).

[3] M. Thakurathi, J. Klinovaja, and D. Loss, From fractional boundary charges to quantized hall conductance, *Physical Review B* **98**, 245404 (2018).
 [4] K. Plekhanov, F. Ronetti, D. Loss, and J. Klinovaja, Hinge states in a system of coupled rashba layers, *Physical Review Research* **2**, 013083 (2020).

Protecting RF-circuitry with superconducting low-pass filters

Deepankar Sarmah,¹ Jann Hinnerk Ungerer,^{1,2} Joost Ridderbos,¹ Artem Kononov,¹ and Christian Schönenberger^{1,2}

¹Quantum- and Nanoelectronics Lab, University of Basel, CH-4056 Basel, Switzerland

²Swiss Nanoscience Institute, University of Basel, CH-4056 Basel, Switzerland

Circuit quantum electrodynamics (QED) is a promising approach for scalable quantum architecture. We aim to achieve strong spin-photon coupling in a resonator-nanowire hybrid system. For this we need to use a high-impedance resonator, as the resonator-dot coupling depends on the impedance. The resonator is coupled to a Ge/Si core/shell nanowire where the quantum dots are defined by bottom-gates. These bottom-gates are connected to the dc-control lines. Since the resonator is capacitively coupled to the dc-lines, it opens a loss channel for the microwave signal and hence the quality factor degrades. To prevent this loss, we make use of superconducting low-pass filters on these dc-lines, which suppresses the leakage of the microwave signal to the environment. Thereby, preserving the quality factor and hence the photon coherence.

I. INTRODUCTION

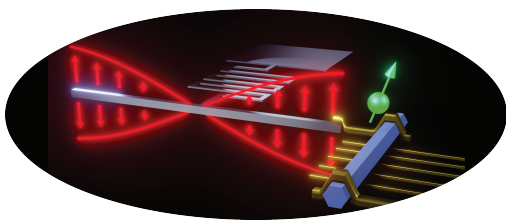
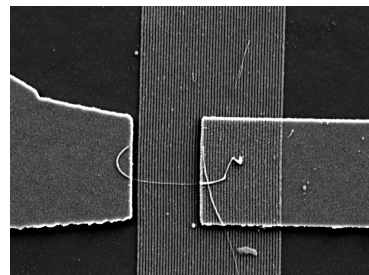


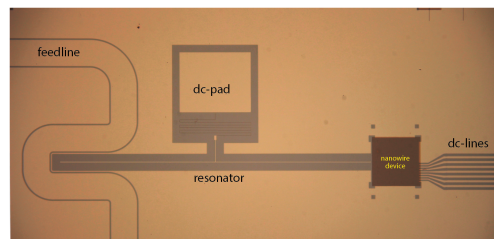
Figure 1: Schematic depicting the coupling between microwave-photon, in a resonator, and a hole spin, in a nanowire, defined by bottom gates [Image credit: Mehdi Ramezani]

Our long term goal is to achieve the spin-photon coupling in a resonator-nanowire hybrid system as shown in Figure 1. For this purpose we use a high-impedance $\lambda/2$ -resonators, as the dot-resonator coupling is given by $g_c \propto \sqrt{Z_r}$, where Z_r is the impedance of the resonator¹². The resonators are fabricated from thin-film(10nm) high-kinetic-impedance NbTiN_x, on top of intrinsic-Si substrate. They are magnetic field resilient, up to several Teslas in-plane and around 300mT out-of-plane magnetic field. These resonators have quality-factor of more than 300,000. High-quality factor of the resonators is a major requirement as we want to have long microwave-photon coherence. The quantum dots(QDs) in the Ge/Si core/shell nanowire is defined by bottom-gates(with 60nm pitch) as shown in Figure 2a. These bottom-gates are then connected to the dc-lines. The complete picture can be seen in Figure 2b. This opens a loss channel for the signal in resonator, whereby it can leak to the electromagnetic environment.

The quality-factor of the bare resonator is obtained to be more than 300,000 whereas the quality-factor after the integration of the nanowire QDs to the resonator goes down drastically to around 700. This is shown in the curve shown in Figure 3, where we plot the phase vs frequency sweep and fit the curve to obtain the quality factors. We suspect this happens due to the leakage of



(a) SEM image of a Ge/Si core/shell nanowire on top of parallel bottom-gates structure of pitch 60nm. The nanowire and bottom-gates are separated by HfO₂ dielectric.



(b) Optical image of our full device showing the feedline, resonator, nanowire device stage and the dc-lines

Figure 2: Images of the typical device

microwave signal to the environment through the dc-lines as they are capacitively coupled to the resonator.

II. IMPLEMENTATION

We fabricate LCL low-pass filters, with inductance of 47nH and capacitance of 1.5pF. The cut-off frequency of this filter is around 850MHz and the transmission is highly suppressed in the frequency range of 2 – 4GHz, as shown in Figure 4. This is the range of operation for our resonator. Hence, the high-frequency signals are not allowed to leak to the environment through the dc-lines.

These filters are patterned from thin-film NbTiN_x on top of intrinsicSi/SiO₂(100nm) substrate. This allow us to dc-characterised the filters at room temperature due to the presence of oxide layer. We fabricate a set

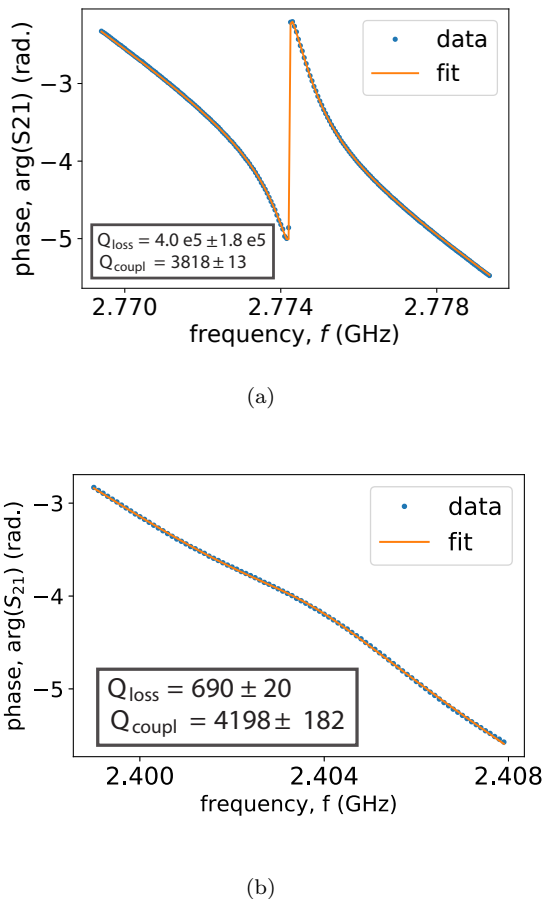


Figure 3: (a) Fitted resonance curve of the bare resonator without dc-lines (b) Fitted resonance curve of the resonator coupled to the nanowire with dc-lines

of 10 – 12 filters on a chip and place it alongside the resonator-nanowire hybrid device as shown in Figure 5. The dc-pads, connecting to bottom-gates, are then connected to one port of the filter and the bond from other port is connected to the circuit lines in the PCB which then goes to the dc-lines out of the fridge. By the use of this filter we expect to enhance the quality factor of the resonator when coupled to the QDs in the nanowire.

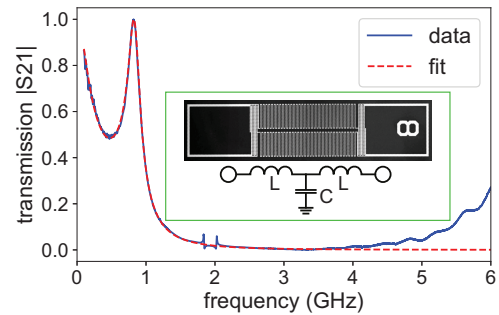


Figure 4: Transmission measured through the two ports of the low-pass filter and fitted with the ABCD-matrix theory. The inset shows the SEM image of the filter with meandered inductors on either side and an interdigitated capacitor in the middle, the schematic is also shown.

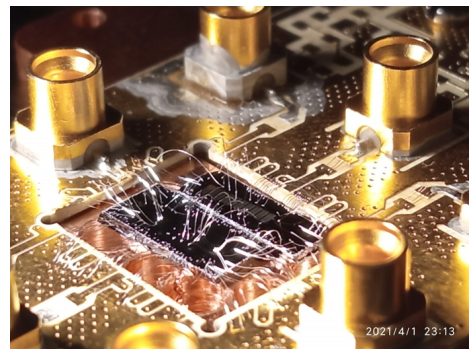


Figure 5: Image of the circuit board with two chips, (right) chip containing resonator-nanowire and (left) chip with a set of low-pass filters

Acknowledgments

We would like to acknowledge support from NCCR SPIN, the Swiss National Science Foundation, the Swiss Nanoscience Institute (SNI) and the European Research Council (ERC). We would also like to thank the RF-team at quantum- and nanoelectronics group in the university of Basel for their support.

¹ P Harvey-Collard, G Zheng, J Dijkema, N. Samkharadze, A Sammak, G Scappucci, and L.M.K Vandersypen. On-Chip Microwave Filters for High-Impedance Resonators with Gate-Defined Quantum Dots. *Phys. Rev. Applied*, 14:034025, 2020.

² N. Samkharadze, G. Zheng, N. Kalhor, D. Brousse, A. Sammak, U. C. Mendes, A. Blais, G. Scappucci, and L. M. K. Vandersypen. Strong spin-photon coupling in silicon. *Science*, 359:1123, 2018.

Platforms for measuring the thermal conductivity of Superlattices Nanowires

C. Arya^{1*}, M.Y. Swinkels¹, Y. Kaur¹, I. Zardo¹

¹ Department Physik, Universität Basel, Klingelbergstrasse 82, CH-4056 Basel, Switzerland
*corresponding author: chaitanya.arya@unibas.ch

Phonons are quantized vibrations of atoms in crystals responsible for the transmission of sound and heat. Therefore, the capability to engineer phonons in condensed matter corresponds to the capability to tune the sonic and thermal properties of materials, with great potential also for new technological applications. Nanowires are a very interesting platform for investigating and designing phonon interference effects because they offer unique possibilities in terms of heterostructuring (i.e. combining materials that cannot be joined in 2D because of lattice mismatch and realizing crystal phase superlattices) and they enable the growth of high-quality nanowire junctions or networks. In this work, we discuss our progresses in the realization of experiments for probing phonon interference effects by means of thermal transport experiments on nanowire superlattices and nanowire junctions.

Superlattice Nanowires

In the last decades, continuous efforts have been made to understand and control phonons with great potential for numerous technological applications [1]. The objective of this project is to investigate phonons interference and different phonon transport regimes, which is crucial for the manipulation of phonons. Nanowires are promising candidates for studying the phonons interference effect because they offer unique possibilities in terms of heterostructure and also enables the growth of high-quality nanowire junctions. In this respect, a superlattice (a lattice made by different materials alternated periodically) can be used to investigate the behavior of phonons scattered from interfaces. Phonons scattered from single interfaces lose their phase information, leading to diffusive thermal transport. However, for periodic repetition of interfaces with a period comparable to the phonon mean free path, scattered phonons can interfere before losing their phase information resulting in a modified phonon dispersion and thermal conductivity of the nanowire [2].

Measuring thermal conductivity

A nanowire has a typical length of few micrometers and its thermal conductivity is very low. Therefore, measuring the thermal conductivity of a single nanowire requires a platform with good

isolation where the temperature change across the nanowire can be controlled and measured with very high sensitivity. Therefore, a suspended microdevice is fabricated to perform controlled measurements at the nanoscale. The fabricated microdevice is based on the device used by Shi et al. [3]. The microdevice consists of gold deposited on 0.5mm long suspended SiNx beam to ensure thermal isolation as shown in figure 1. These SiNx beams supports two meanders platform in the center with gold coils that act as a heater and sensor. The nanowire is suspended between the two platforms using a micromanipulator. To measure the thermal conductivity, the temperature is raised on one platform while the change in temperature on the second platform is measured as a function of heating power. To assess the temperature, the resistance of meanders is measured by four-point probe technique. The heat flux across the nanowire is calculated by measuring the power dissipated in the meanders. The total power dissipated in heating up the platform is calculated using equation 1, assuming that half of the power dissipated in the lines contributes to heating up the meanders [4].

$$P_{total} = P_{meanders} + 0.5P_{lines} \quad (1)$$

Equation 1 is the total power dissipated in the meanders while the power going through the

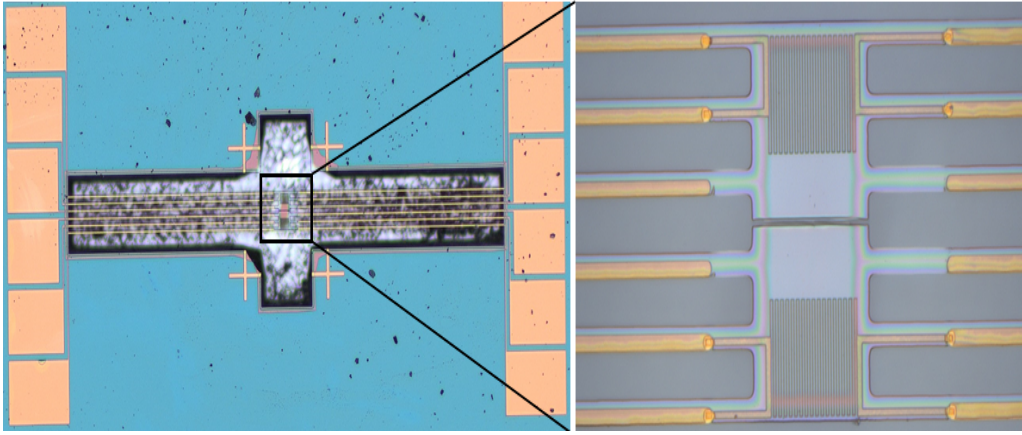


Figure 1: *Suspended microdevice for measuring thermal transport in nanowires.*

nanowire is less because some power is dissipated to the environment. The energy balance for the total system is given in equation 2 where P_H and P_S is the power dissipated in the heating and sensing coils, G_B is the thermal conductance of the suspension beams, and ΔT is the temperature difference. Assuming that both platforms have similar beam conductance, equation 3 is obtained. To calculate the conductance of the nanowires, the heat balance equation (4) is written for the sensing membrane, where G_N is the conductance of the nanowire [4]. Finally, the thermal conductivity of the nanowire is calculated using the G_N , and nanowire's length and diameter.

$$P_H + P_S = G_{B,H}\Delta T_H + G_{B,S}\Delta T_S \quad (2)$$

$$G_B = \frac{P_H + P_S}{\Delta T_H + \Delta T_S} \quad (3)$$

$$G_{B,S}\Delta T_S = G_N(\Delta T_H - \Delta T_S) \quad (4)$$

Microdevice Fabrication

SiNx is deposited onto a 2-inch silicon wafer by plasma enhanced chemical vapor deposition. Optical lithography is used for the definition of the

beams using a laser writer and gold is deposited using an electron beam evaporator. Electron beam lithography is used for writing the meanders, followed by metal deposition. Before etching the Silicon underneath the device, SiNx is deposited to protect the device during the etching process. After that, dry etching is performed using reactive ion etching followed by wet etching in TMAH and KOH to remove SiNx and Silicon, respectively. The microdevice is dried in Isopropanol to get the suspended two-terminal devices. Finally, focused ion beam is performed on suspended device to separate the heating and sensing platform.

Acknowledgement

We acknowledge both Eucor, The European Campus, and SNSF, the Swiss National Science Foundation (Project Grant No. 184942) for financial support this project. The QUSTEC program has received funding from the European Union's Horizon 2020 research and innovation program under the Marie Skłodowska-Curie grant agreement number 847471.

References

- [1] M. Maldovan, *Nature* **503**, 209 (2013).
- [2] M. Maldovan, *Nature* **14**, 667 (2015).
- [3] P. Kim, *Physical Review Letters* **87**, 19 (2001).
- [4] L. Shi, *Journal of Heat Transfer* **125**, 881 (2003).

Hierarchical equations of motions (HEOM) approach to the study of thermodynamic uncertainty relations

Salvatore Gatto, Michael Thoss^{1,2}

¹*Institute of Physics, Albert-Ludwigs-Universität Freiburg*

²*EUCOR Centre for Quantum Science and Quantum Computing*

The thermodynamic uncertainty relation (TUR) is a cost-precision trade-off relationship in transport systems, relating the fluctuations in the heat and particle currents to the reversibility of the operation regime. While some violations had been reported for the classical TUR, it has been found out that the geometry of quantum non-equilibrium steady-states alone directly implies the existence of a general quantum TUR. The aim of the project is to shed light on the relationship between quantum effects and current fluctuations in autonomous machines. The hierarchical equation of motion (HEOM) approach is employed, which allows a numerically exact simulation of nonequilibrium transport in general open quantum systems involving multiple bosonic and fermionic environments.

I. MOTIVATIONS

The thermodynamic uncertainty relations (TUR) are cost-precision trade-off relationships in transport systems. It was recently derived for classical markovian systems operating at steady state¹, with generalizations to finite-time², time-discrete and driven Markov chains³. The thermodynamic uncertainty relation has generated significant research work directed at understanding its ramifications to dissipative systems such as biochemical motors and heat engines⁴ and probing its validity in the classical regime⁵ and beyond⁶.

For a two-terminal single-affinity system, the TUR connects the steady state averaged current $\langle j \rangle$, its normalized variance $\langle \langle j^2 \rangle \rangle_c$, and the entropy production rate σ in a nonequilibrium process as

$$\frac{\langle \langle j^2 \rangle \rangle_c}{\langle j \rangle^2} \frac{\sigma}{k_B} \geq 2. \quad (1)$$

Eq. (1) points to a fundamental trade-off between precision and dissipation: a precise process with little noise is realized with a high thermodynamic (entropic) cost.

II. TUR FOR QUANTUM SYSTEMS

Recently, it has been shown⁷ that the classical TUR Eq. (1) can be violated in the quantum regime.

Autonomous machines operate in a regime known as non-equilibrium steady state (NESS), characterized by a non-zero entropy production rate and by an ability to maintain non-zero average currents across the system.

Generalizing the idea of Gibbs distributions to the set of NESSs is known as the non-equilibrium statistical operator approach, or the McLennan-Zubarev form⁸.

The geometry of quantum NESS, by itself, already implies the existence of a TUR of the form

$$\langle \hat{\sigma} \rangle \geq \langle \hat{\mathbf{J}} \rangle^T \mathbf{\Delta}^{-1} \langle \hat{\mathbf{J}} \rangle, \quad (2)$$

where $\mathbf{\Delta}$ is the normalized covariance matrix between different steady-state currents. By restricting to the single-

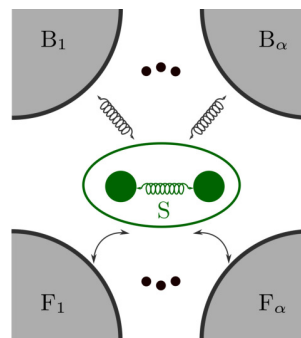


FIG. 1: Sketch of an open quantum systems coupled to multiple fermionic and bosonic environments.

component vector case, one immediately in particular obtains

$$\frac{\Delta j_\alpha}{\langle \hat{j}_\alpha \rangle^2} \langle \hat{\sigma} \rangle \geq 1, \quad (3)$$

which, compared to the classical result in Eq. (1), shows that our bound involving the variance of currents can in principle be two times looser. This result shows the universal nature of TURs, generalizing the concept of thermodynamics of precision to a much larger class of physical processes.

III. THE HEOM APPROACH

The HEOM method was originally developed by Tanimura and Kubo⁹ and was later extended for more general models, which include multiple bosonic and fermionic environments¹⁰, allowing to study more general scenarios such as electronic and phononic heat transport induced by bias voltages or temperature differences.

IV. METHOD

We consider an open quantum system described by a subsystem S , which is coupled to both bosonic (B) and a fermionic (F) environments. The total Hamiltonian is given by

$$H = H_S + H_{SB} + H_B + H_{SF} + H_F. \quad (4)$$

The central quantity of the approach is the reduced density matrix $\rho(t)$ of the subsystem, defined by the trace over the DOFs of the environment of the total density matrix $\varrho(t)$,

$$\rho(t) = \text{Tr}_{B+F} \{ \varrho(t) \}. \quad (5)$$

Exploiting the Gaussian properties of the noninteracting environments, a formally exact path-integral for the reduced density matrix of the subsystem involving a Feynman-Vernon influence functional can be derived.¹¹ The hierarchical equations of motion are constructed by consecutive time-derivatives of the influence functional, leading to¹²

$$\begin{aligned} \frac{\partial}{\partial t} \rho_{g|h}^{(m|n)} = & - \left(i\mathcal{L}_S + \sum_{l=1}^m \gamma_{gl} + \sum_{l=1}^n \gamma_{hl} \right) \rho_{g|h}^{(m|n)} \\ & - \sum_{h_x} \mathcal{A}_{h_x} \rho_{g|h_x^+}^{(m|n+1)} - \sum_{l=1}^n (-1)^l \mathcal{C}_{h_l} \rho_{g|h_l^-}^{(m|n-1)} \\ & + \sum_{g_x} \mathcal{B}_{g_x} \rho_{g_x^+|h}^{(m+1|n)} + \sum_{l=1}^m \mathcal{D}_{g_l} \rho_{g_l^-|h}^{(m-1|n)}, \quad (6) \end{aligned}$$

with the multi-indices $g = (p, \alpha)$, $h = (q, \alpha, s)$, the notation for the multi-index vectors $v = v_1 \cdots v_p$, $v_x^+ = v_1 \cdots v_p v_x$, and $v_l^- = v_1 \cdots v_{l-1} v_{l+1} \cdots v_p$, and $\mathcal{L}_S \mathcal{O} = [H_S, \mathcal{O}]$. Here, $\rho^{(0|0)}$ represents the reduced density operator of the subsystem, and the higher-tier auxiliary density operators (ADOs) $\rho_{g|h}^{(m|n)}$ encode the influence of the environment on the subsystem dynamics. Tier by tier the ADOs introduce the effect of higher order system-bath correlations.

The operators \mathcal{A}_{h_x} and \mathcal{C}_{h_l} connect the n th-fermionic-tier ADO to the $(n+1)$ th- resp. $(n-1)$ th-fermionic-tier ADOs and the operators \mathcal{B}_{g_x} and \mathcal{D}_{g_l} connect the m th-bosonic-tier ADO to the $(m+1)$ th- resp. $(m-1)$ th-bosonic-tier ADOs via

$$\mathcal{A}_{h_x} \rho_{g|h}^{(m|n)} = \Gamma \left(W^{s_{h_x}} \rho_{g|h}^{(m|n)} + (-1)^{(n)} \rho_{g|h}^{(m|n)} W^{s_{h_x}} \right), \quad (7a)$$

$$\mathcal{B}_{g_x} \rho_{g|h}^{(m|n)} = \Lambda \left[V, \rho_{g|h}^{(m|n)} \right], \quad (7b)$$

$$\mathcal{C}_{h_l} \rho_{g|h}^{(m|n)} = (-1)^n \eta_{h_l} W^{\bar{s}_{h_l}} \rho_{g|h}^{(m|n)} - \eta_{h_l}^* \rho_{g|h}^{(m|n)} W^{\bar{s}_{h_l}}, \quad (7c)$$

$$\mathcal{D}_{g_l} \rho_{g|h}^{(m|n)} = \eta_{g_l} V \rho_{g|h}^{(m|n)} - \eta_{g_l}^* \rho_{g|h}^{(m|n)} V, \quad (7d)$$

leading to a two-fold hierarchy of equations of motion.

V. CONCLUSION

Investigating the validity of the thermodynamic uncertainty relations opens up an interesting perspective, as it would in principle allow one to use quantum effects to reduce the deleterious current fluctuations without compromising the engine's efficiency and output power¹³.

Within this project, the HEOM method allows the study of quantum transport through nanosystems induced by bias voltages and/or temperature differences in a numerically exact manner for both types of environments on equal footing.

Applications of the extended HQME method to more complex models and/or time-dependent setups are possible and promise to reveal further interesting physical effects in nanosystems.

Acknowledgments

The QUSTEC programme has received funding from the European Union's Horizon 2020 research and innovation programme under the Marie Skłodowska-Curie grant agreement number 847471. I would like to thank the support by the state of Baden-Württemberg through bwHPC and the German Research Foundation (DFG).

¹ A. C. Barato and U. Seifert, Phys. Rev. Lett. **114**, 158101 (2015).

² P. Pietzonka and U. Seifert, Phys. Rev. E **96**, 012101 (2017).

³ K. Proesmans and C. V. den Broeck, Europhysics. Letters **119** (2), 20001 (2017).

⁴ R. M. III and J. England, Rep. Prog. Phys. **81**, 016601 (2018).

⁵ C. Hyeon and W. Hwang, Phys. Rev. E **96**, 012156 (2017).

⁶ T. H. K. Brandner and K. Saito, Phys. Rev. Lett. **120**, 090601 (2018).

⁷ K. Ptaszyński, Phys. Rev. B **98** (2018).

⁸ D. Zubarev, Cond. Matt. Phys **4** (1994).

⁹ Y. Tanimura and R. Kubo, J. Phys. Soc. Jpn. **58**, 101 (1989), ISSN 0031-9015.

¹⁰ J. Jin, X. Zheng, and Y. Yan, J. Chem. Phys. **128**, 234703 (2008), ISSN 0021-9606.

¹¹ R. P. Feynman, Phys. Rev. **84**, 108 (1951), ISSN 0031-899X.

¹² C. Schinabeck, R. Härtle, and M. Thoss, Phys. Rev. B **97**, 235429 (2018), ISSN 2469-9950.

¹³ R. Kosloff, Entropy **15**, 2100 (2013).

Quality of gate-induced 2D hole gases in silicon with 10 nm oxide

Petar Tomić,^{1,*} Felix Schupp,² Matthias Mergenthaler,² Gian Salis,² Andreas Fuhrer,² Thomas Ihn,¹ and Klaus Ensslin¹

¹Laboratory for Solid State Physics, ETH Zürich, CH-8093 Zürich, Switzerland

²IBM Research – Zürich, Säumerstrasse 4, 8803 Rüschlikon, Switzerland

A large-scale quantum computer based on the electron/hole spin degree of freedom in silicon quantum dots relies on building reliable and reproducible quantum dot arrays¹. Hence, it is of great importance to fabricate metal-oxide-semiconductor (MOS) stacks with high quality. Therefore, in this work, we investigate two dimensional hole gases (2DHG) in silicon MOSFET Hall bars, as 2DHGs are not as thoroughly studied as 2DEGs in respective structures. The analysis is performed through magnetotransport and capacitance measurements. Furthermore, we show the effect of annealing on the carrier mobility.

Introduction

Long coherence time, scalability potential and CMOS compatibility make spin of electrons and holes in silicon quantum dots a promising platform for building a large-scale quantum computer. While electrons show longer coherence times, holes are more promising for implementations with all-electrical control. Strong spin-orbit interaction allows for fast qubit driving via electric-dipole spin resonance (EDSR) and coherence times can be improved with gate tunable spin-orbit coupling².

One of the promising architectures is based on two dimensional quantum dot arrays where quantum dots are defined at the interface of oxide and silicon in MOS structures. Therefore, in order to build reproducible and reliable arrays of hole quantum dots it is of crucial importance to fabricate MOS stacks with high quality.

So far, the literature is only focused on the electrons, in this work, we characterize two dimensional hole gas in Si-MOSFET Hall bar structures by measuring Hall mobility and evaluate interface traps with capacitance measurements. Furthermore, we use annealing techniques to improve the interface quality.

Devices

Investigated MOS devices are based on nominally undoped silicon substrate, covered with a 10 nm silicon oxide layer with a 20 nm titanium nitride gate. By applying negative gate voltages to the gate, 2DHG is accumulated at the Si-SiO_x interface. 2DHG is contacted via platinum silicide which favors hole transport since its Fermi energy is close to the valence band of silicon. Furthermore, silicide is contacted via aluminium bond pads.

Two types of gating configurations were used. First, single gated devices were patterned where only one gate is used to simultaneously accumulate carriers in the channel of the Hall bar and its leads. Second, double gated devices were fabricated allowing independent tunability of the densities in the leads and the channel of the Hall bar. In such devices, leads were tuned to highest densities (limited by leakage) to allow for better contacts.

Measurements

Devices were first characterized via magneto-transport measurements performed in the temperature range of 70 mK to 60 K. In the low temperature regime, 1.2 K, gate voltage dependence of density, mobility and mean free path were extracted. Linear density - gate voltage relation was observed with an onset density of $2 \times 10^{12} \text{ cm}^{-2}$ at gate voltage of -3 V . The peak mobility was found to be $300 \text{ cm}^2/\text{Vs}$ at a density of $3.8 \times 10^{12} \text{ cm}^{-2}$ corresponding to a mean free path of 10 nm. Additionally, temperature dependence of strong positive magnetoresistance was probed in the low temperature regime which was interpreted as weak antilocalization.

Contrary, high temperature measurements showed thermally activated two subband transport with an onset temperature of 30 K which showed weak gate voltage dependence. However, second subband couldn't be occupied with gate voltages at lower temperatures even at densities of $1.6 \times 10^{13} \text{ cm}^{-2}$. This is not in accordance with theoretical calculations of subband energies^{3,4}. Furthermore, a simple two-subband model neglecting inter-subband scattering was used to fit the data yielding high occupation/low mobility subband and vice versa with 10 fold difference in mobility in favor of low occupied subband.

Double gated configuration of Hall bars allowed for capacitance measurements. Channel gate forms a capacitor with 2DHG while leads supply charge carriers to the 2DHG through 4 grounded contacts. Due to large contact resistance, capacitance measurements were limited to $< 1 \text{ kHz}$ frequencies. Furthermore, using the gate dependent conductance and capacitance measurements we estimated an interface trap density of $6.5 \times 10^{11} \text{ cm}^{-2} \text{ eV}^{-1}$.

Annealing

We investigated how annealing affects transport characteristics of Hall bar devices. Annealing was performed in a forming gas atmosphere, 5% H₂ and 95% N₂, at a temperature of 400 °C for 20 minutes. Increased density range, $1 - 10 \times 10^{12} \text{ cm}^{-2}$, was observed in annealed de-

vices. Furthermore, the threshold voltage was lowered to -1.8 V from initial -3 V. Annealed devices also showed increased peak mobility reaching 580 cm²/Vs at densities of 2×10^{11} cm⁻² corresponding to a mean free path of 15.5 nm. Interestingly, the density of interface traps remained unchanged after annealing.

Outlook

As the mean free path measured in our devices is of the same order as typical silicon quantum dots, further efforts need to be invested in optimization of the MOS stack to increase the mean free path. Furthermore, assessment of the interface trap density needs dedicated structures to minimize the contact resistance enabling measurements at higher frequencies. Finally, optimal annealing time

should be investigated as well as at which step of fabrication process should annealing be done.

Acknowledgments

We thank the Cleanroom Operations Team of the IBM Binnig and Rohrer Nanotechnology Center (BRNC) for their help and support. We acknowledge the support from Peter Maerki and Thomas Baehler. P.T. and F.S acknowledge support from the Swiss National Science Foundation through NCCR SPIN. This work is supported by the Swiss National Science Foundation and NCCR SPIN. M.M. acknowledges funding from the European Union's Horizon 2020 research and innovation programme under the Marie Skłodowska-Curie grant agreement No 899018.

* Electronic address: ptomic@phys.ethz.ch

¹ L. M. Vandersypen and M. A. Eriksson, *Quantum computing with semiconductor spins*, Physics Today **72**, 8 (2019).

² S. Bosco, B. Hetényi, and D. Loss, *Hole spin qubits in Si finfets with fully tunable spin-orbit coupling and sweet spots for charge noise*, PRX Quantum **2**, 010348 (2021).

³ S. Rodriguez, J. A. López-Villanueva, I. Melchor, and J. Carceller, *Hole confinement and energy subbands in a sil-*

icon inversion layer using the effective mass theory, Journal of applied physics **86**, 438 (1999).

⁴ F. J. Ohkawa and Y. Uemura, *Hartree approximation for the electronic structure of a p-channel inversion layer of silicon mos*, Progress of Theoretical Physics Supplement **57**, 164 (1975).

Control of Growth Direction of Ge Nanowires

Nicolas Forrer¹, Gerard Gadea¹, Ilaria Zardo¹

¹*Nanophononics Group, Universität Basel, Kingelbergstrasse 82, CH-4056 Basel, Switzerland*

Ge-Si core-shell nanowires constitute an excellent candidate for their application as qubits in quantum computation. For this, nanowires of high quality and controlled axial directions are needed. In this work, we show a way to directly influence the direction of nanowires grown by the vapour-liquid-solid method by changing the surface density of the nanoparticles deposited on the substrate.

I. MOTIVATION

In order to build reliable quantum computers, Ge-Si core-shell nanowires (NW) could be used as platforms to host fast and fully electrical controlled qubits [1]. Namely, Ge-Si core-shell NWs exhibit a strong hole confinement and a large direct Rashba spin-orbit coupling (by adding an electric field) [1]. To maximise the spin-orbit energy, high quality NWs grown along $\langle 110 \rangle$ direction [2], virtually perfect crystallinity and abrupt Ge-Si interfaces are needed. By using vapour-liquid-solid (VLS) growth processes we want to understand and control the mechanisms that rule the leading NW growth direction, especially since the growth direction is a crucial property for defect free core-shell NWs [3].

II. VAPOUR-LIQUID-SOLID PROCESS

After deposition of metal catalyst nanoparticles (NPs) on a crystalline substrate, the substrate is heated up until the particles melt and mix with the substrate, forming eutectic alloy nano-droplets (figure 1a). Once the eutectic alloy is formed, the precursor gas (e.g. GeH_4) is injected into the reactor chamber at the desired temperature and pressure conditions. Then, the NP acts as catalyst to transform the GeH_4 to Ge and H_2 . The Ge now accumulates in the NP until it is saturated. At this point the Ge starts to precipitate out of the NP in a layer-by-layer manner, following the underlying lattice order, when compatible - i.e. epitaxially. The NW starts to grow, in the so called bottom-up fashion (figure 1b and figure 1c). As a last step, the growth conditions are changed and SiH_4 is injected into the chamber. SiH_4 decomposes and deposits in a conformal manner, leading to the formation of a Si shell around the Ge core (figure 1d).

III. SAMPLE PREPARATION

The Ge-Si core-shell NWs were grown by VLS approach using a gold catalysed reaction for the Ge core and an uncatalyzed one for the Si shell. The gold NPs (diameter of 5 and 10 nm) were deposited onto a Si $\langle 100 \rangle$ substrate from a commercial colloidal suspension, which was diluted in deionized water at different factors, ranging from undiluted to 1 : 300 dilution. For the deposition an electrostatic approach was employed, triggered by the addition of HCl 0.1 M [4]. Before growth, the samples

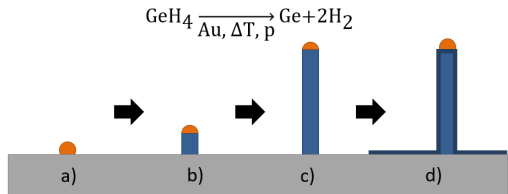


FIG. 1. General VLS process with a) formation of eutectic alloy nano-droplets (liquid), b) the addition of the precursor gas into the reaction chamber (vapour) and start of growth, c) elongation of the wires (solid), d) uncatalysed shell growth.

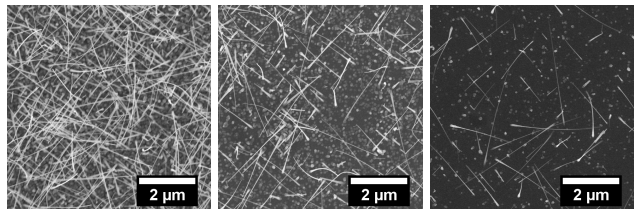


FIG. 2. SEM images of Ge-Si core-shell NWs with different dilutions. From left to right: undiluted, 1:3 and 1:30.

were immersed into a 2% HF solution for 1 min to remove the native silicon oxide. The growth protocol consisted of three steps: a nucleation step at 350°C for 15 min and an elongation step at 280°C for 180 min, both at GeH_4 partial pressure of 0.2 Torr, and a shell deposition step at 600°C for 15 min with a SiH_4 partial pressure of 0.1 Torr. After growth, the NWs were imaged by scanning electron microscopy (SEM) to determine the nanowires' orientation. The SEM scan direction was thereby oriented parallel to the natural cleaving plane of the Si chip, whose edge lines follow $\langle 110 \rangle$ directions. Figure 2 shows a series of SEM images of Ge-Si core shell NWs grown under the same conditions and Au-NP surface densities decreasing from left to right.

IV. RESULTS AND DISCUSSION

On the right-hand side of figure 3, we show a schematic drawing of the NWs when viewed from top, i.e. like in top view SEM imaging. Here the $\langle 110 \rangle$ NWs are represented as diagonal lines and the $\langle 111 \rangle$ NWs as horizontal and vertical lines. Figure 4 shows the projected angle of NWs grown using 5 nm and 10 nm NPs, and increasing

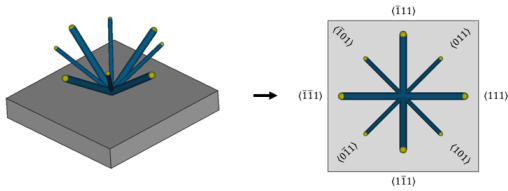


FIG. 3. Schematic of the analysis procedure to determine the growth direction. During the imaging the scan direction was oriented parallel to the natural cleaving plane of the Si substrate. This way, the $\langle 110 \rangle$ direction is oriented diagonally and the $\langle 111 \rangle$ direction horizontally and vertically, when seen from top.

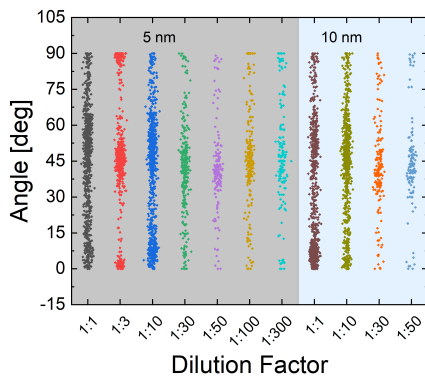


FIG. 4. Projected angles of the analysed NWs, from the SEM images (figure 3). Due to the 4-fold symmetry of the Si/Ge cubic crystals, a modulus 90° was applied to the data (initially spanning from 0 to 360°), for the sake of clarity.

dilution of the colloidal suspension (x-axis), i.e. decreasing surface density. Three agglomerations can be found, one at 45° representing the $\langle 110 \rangle$ NWs and two (at 0° and 90°), representing the $\langle 111 \rangle$ NWs. The agglomeration around 45° becomes predominant for higher dilutions, for which we can conclude that the NWs show a preferred growth direction along $\langle 110 \rangle$.

From the data plotted in figure 4 we can determine the density of NWs grown along the $\langle 110 \rangle$ direction by selecting only angles in the range of $45^\circ \pm 10^\circ$. By dividing the count of NWs by the NP surface density the

yield of $\langle 110 \rangle$ -oriented NWs (figure 5, open symbols) and the total number of NWs (figure 5, filled symbols) with respect to the number of NPs is calculated. We can argue that the ratio of $\langle 110 \rangle$ oriented NWs is increasing, with increasing dilution, i.e. with decreasing NP surface density. In general, bigger colloids show a higher NW yield, which agrees well with the Gibbs-Thomson-Effect [5]. The yield of the 1:50 dilution for the 10 nm NPs cannot be explained yet.

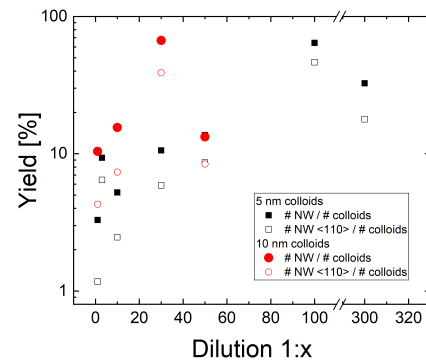


FIG. 5. Yield of NW grow for different dilutions and colloid sizes. An increase in success rate is observable with increasing dilution.

V. CONCLUSION AND OUTLOOK

We applied a reliable way of determining the orientation of the NWs using only SEM imaging. With higher dilutions, the $\langle 110 \rangle$ growth direction is preferred and we can control the NW yield by changing the dilution of the colloids. In further experiments we will investigate the use of other catalysts to fabricate thin and untapered NWs. By integrating a lithography step to define a controlled array of nanoparticles, we will be able to tune the composition and the dimensions of the catalyst, and designing them according to our needs.

ACKNOWLEDGMENTS

This work is supported by the Swiss National Science Foundation and NCCR SPIN.

- [1] C. Kloeffel, M. Trif, and D. Loss, *Strong spin-orbit interaction and helical hole states in ge/si nanowires*, Physical Review B **84**, 195314 (2011).
- [2] C. Kloeffel, M. J. Rančić, and D. Loss, *Direct rashba spin-orbit interaction in si and ge nanowires with different growth directions*, Physical Review B **97**, 235422 (2018).
- [3] S. Conesa-Boj, A. Li, S. Koelling, M. Brauns, J. Ridderbos, T. T. Nguyen, M. A. Verheijen, P. M. Koenraad, F. A. Zwanenburg, and E. P. Bakkers, *Boosting hole mobility in coherently strained [110]-oriented ge-si core-shell*

- nanowires*, Nano letters **17**, 2259 (2017).
- [4] J. H. Woodruff, J. B. Ratchford, I. A. Goldthorpe, P. C. McIntyre, and C. E. Chidsey, *Vertically oriented germanium nanowires grown from gold colloids on silicon substrates and subsequent gold removal*, Nano letters **7**, 1637 (2007).
- [5] S. A. Dayeh and S. Picraux, *Direct observation of nanoscale size effects in ge semiconductor nanowire growth*, Nano letters **10**, 4032 (2010).

Planar heterostructures for quantum dot spin qubits

Arianna Nigro,¹ Santhanu Panikar Ramanandan,² Anna Fontcuberta i Morral,² Gerard Gadea,¹ and Ilaria Zardo¹

¹*Nanophononics Group, Universität Basel, CH-4056 Basel, Switzerland*

²*Laboratoire des Matériaux Semiconducteurs, Ecole Polytechnique Fédérale de Lausanne, Lausanne, 1015, Switzerland*

A great deal of interest is directed nowadays towards the development of innovative technologies in the field of quantum information and quantum computing, with emphasis in obtaining reliable qubits as the building blocks. In this framework, Germanium-Silicon heterostructure quantum wells are gaining popularity as they allow to develop highly accessible, stable and scalable spin-qubit devices. In this work, we explored the Chemical Vapor Deposition growth conditions and the quality of epitaxial Ge layers on Si, a step that is crucial for the subsequent fabrication of highly functional Ge-Si quantum well qubits.

I. INTRODUCTION

Recently Germanium (Ge) has emerged as a fundamental material for quantum information because of its attractive properties. Ge/SiGe heterostructures were developed as a successful planar technology able to combine low disorder, fast qubit driving and scalability as well as compatibility with the mainstream micro-fabrication techniques widely employed in the integrated circuitry industry. Under electrostatic gating, undoped Ge/SiGe quantum wells (QWs) accumulate holes showing a very high mobility (highest among common semiconductors), light effective mass ($\sim 0.08m_e$), and a tunable spin-orbit interaction, allowing a fast and fully electrical control of spin qubits¹⁻⁴.

Any defect in the Ge layer or at the Ge/SiGe interface can potentially serve as scattering center reducing the mobility and the coherence of the spin state of the holes, compromising the qubit operation. For this reason, it is crucial to obtain single crystal, epitaxial Ge and SiGe layers, and clean heterointerfaces.

However, the heteroepitaxial growth of SiGe layers having a high Ge content over Si wafers is challenging because of the large lattice mismatch between Si and Ge ($\sim 4.2\%$), which leads to the formation of misfit (MDs) and threading dislocations (TDs). Therefore, the heterostructure has to be engineered and optimized to reduce the defect density. So far, the most successful approach is the so-called “reverse grading”, shown in fig.1, consisting of six layers: (I) Ge buffer layer, (II) $\text{Si}_{1-x}\text{Ge}_x$ graded substrate, (III) $\text{Si}_{1-\alpha}\text{Ge}_\alpha$ buffer layer of uniform composition, (IV) Ge quantum well, (V) $\text{Si}_{1-\alpha}\text{Ge}_\alpha$ barrier of uniform composition and (VI) Si protective cap. With this approach, smooth layers are achieved, with low roughness and TD density (TDD)⁵. In this case, the SiGe layer is over-relaxed under small biaxial tensile strain, while the QW undergoes compressive strain. These features further enhance the hole mobility because of strain-induced valence band splitting that reduces intervalley scattering and further lowers the hole effective mass⁶.

The use of chemical vapor deposition (CVD) allows the epitaxial growth of thin films with high structural quality and at elevated rates, compared to other techniques (e.g. molecular beam epitaxy, sputtering). The

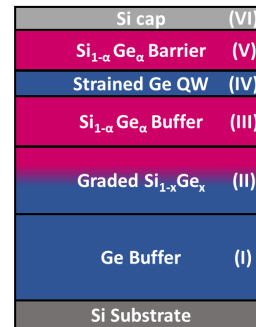


FIG. 1: Layer schematic of the Ge/SiGe QW heterostructure.

CVD growth conditions (temperature, pressure, flows, plasma power and growth time) influence dramatically the deposition rate and properties (mobility, crystallinity, interfaces quality) of the deposited layers. While this allows for a highly controllable process, the wide range of degrees of freedom makes it challenging and calls for a thoroughly optimization study.

This work focuses on the deposition of epitaxial Ge layers on (100) Si, which serve as buffer layer (I in fig.1) and the active layer of the QW (IV in fig.1). The CVD growth rate and the crystalline quality of the as-deposited films were characterized over a wide range of deposition conditions.

II. RESULTS

The Ge layer deposited on top of the Si substrate should be relaxed, smooth and with a low TDD to guarantee a high quality for the successive films. For this purpose, a two temperature growth method⁷ can be employed. The Ge buffer consists of a combination of two layers, namely a thin (~ 100 nm) low temperature seed (LT) and a thick (> 1 μm) high temperature layer (HT). At low temperatures ($T \leq 400^\circ\text{C}$), monolayer islands are generated and coalesce to form a 2D layer proceeding in a Frank-van der Merwe growth mode (layer-by-layer

growth). In this regime, the temperature is high enough to maintain crystallinity but it keeps the epitaxial surface as smooth as possible by suppressing further island growth. A high TDD is generated, allowing the next HT layer to relax the maximum amount of strain possible. The deposition of the successive HT layer reduces the roughness of the surface and lowers the TDD⁷.

The Ge layers within this study were grown by CVD using GeH₄ as gaseous precursor. A single side polished (100) Si wafer was chosen as substrate, and, prior to the growth, it was cleaned for 1 minute in a HF solution to desorb any native oxide. Ge layers were grown for 15 minutes at different temperatures and GeH₄ partial pressures, ranging from 300°C to 500°C and from 50 mtorr to 1000 mtorr, respectively. By measuring the thickness of the deposited Ge layers it was possible to establish the trends in the growth rate (GR), shown in fig.2.

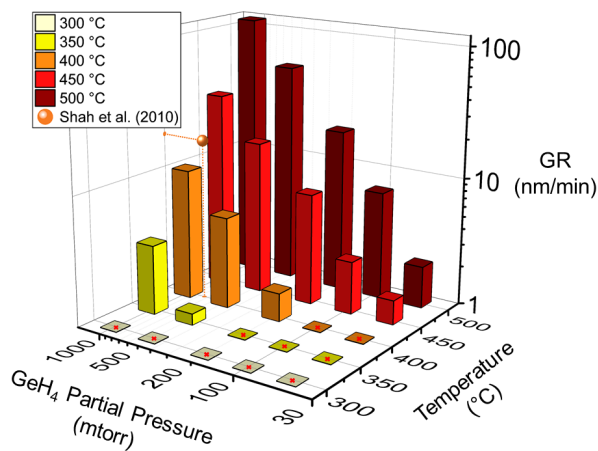


FIG. 2: Growth rate under different conditions of temperature and pressure.

Below 350°C and 500 mtorr no deposition could be observed. The growth rate increases with increasing temperature and pressure, which is explained by the thermal activation of the dissociative adsorption of GeH₄ and the increasing impinging rate at higher partial pressures according to Graham's law. Furthermore, increasing the growth temperature, the pressure values at which a successful growth is observed lowers, up to the minimum level of 50 mtorr.

Fig.3a shows a TEM cross section of a Ge thin film grown at 450°C and 200 mtorr GeH₄ partial pressure on

top of a (100) Si substrate. In the bright field image, a 130 nm thin film is observed, with dislocations originating at the Ge/Si interface and threading up to the top surface, decreasing in density in the process due to mutual annihilation upon interaction. The electron diffraction pattern (fig.3b) taken at the Ge/Si interface reveals two superimposed patterns, aligned and with different lattice parameters, corresponding to the Si substrate and the Ge film. This confirms the successful growth of an epitaxial and relaxed Ge layer, which can be used as a buffer in the reverse grading approach (layer I in fig.1).

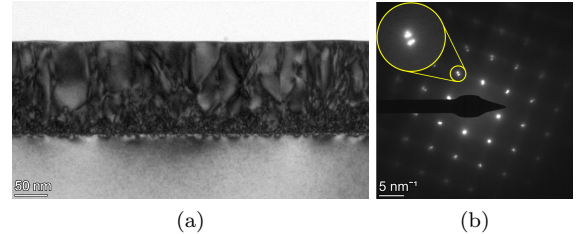


FIG. 3: (a) TEM cross section of a 130 nm thick Ge thin film grown at 450°C and 200 mtorr GeH₄ partial pressure. (b) Electron diffraction pattern at the Ge/Si interface.

III. CONCLUSIONS AND OUTLOOK

Ge thin films were grown on top of Si (100) substrates by means of CVD using GeH₄ as precursor for their application in the fabrication of hole spin qubits hosted in Ge/SiGe QWs. Increase in temperature and GeH₄ partial pressure led to higher growth rate, and minimum values of 350°C and 50 mtorr were deemed necessary to attain deposition. TEM cross section studies confirmed the high quality of the Ge film, which was epitaxial and relaxed, as well as the reduction of the TDD with increasing film thickness.

In the future, we will proceed with the growth and optimization of the successive layers, starting from the Si_{1-x}Ge_x buffer, to complete the whole heterostructure. As a further step, we will focus on the post-growth surface patterning to improve both the confinement and scalability.

Acknowledgments

This work is supported by the Swiss National Science Found and NCCR SPIN.

¹ M. Lodari, N. W. Hendrickx, W. Lawrie, T.-K. Hsiao, L. Vandersypen, A. Sammak, M. Veldhorst, and G. Scappucci, *Low percolation density and charge noise with holes in germanium*, Mater. Quantum Technol. **1** (2021).

² W. J. Hardy, C. T. Harris, Y.-H. Su, Y. Chuang, J. Moussa,

L. N. Maurer, J.-Y. Li, T.-M. Lu, and D. R. Luhman, *Single and double hole quantum dots in strained Ge/SiGe quantum wells*, Nanotechnology **30** (2019).

³ R. Pillarisetty, *Academic and industry research progress in germanium nanodevices*, Nature **479** (2011).

- ⁴ A. Sammak, D. Sabbagh, N. W. Hendrickx, M. Lodari, W. B. Paquelet, A. Tosato, L. Yeoh, M. Bollani, M. Virgilio, M. A. Schubert, et al., *Shallow and Undoped Germanium Quantum Wells: A Playground for Spin and Hybrid Quantum Technology*, *Adv. Funct. Mater.* **29** (2019).
- ⁵ O. Skibitzki, M. H. Zoellner, F. Rovaris, M. A. Schubert, Y. Yamamoto, L. Persichetti, L. Di Gaspare, M. De Seta, R. Gatti, F. Montalenti, et al., *Reduction of threading dislocation density beyond the saturation limit by optimized reverse grading*, *Phys. Rev. Materials* **4** (2020).
- ⁶ A. Dobbie, V. H. Nguyen, R. J. H. Morris, X.-C. Liu, M. Myronov, and L. D. R., *Thermal Stability of Thin Compressively Strained Ge Surface Channels Grown on Relaxed $\text{Si}_{0.2}\text{Ge}_{0.8}$ Reverse-Graded Buffers*, *J. Electrochem. Soc.* **159** (2012).
- ⁷ V. A. Shah, A. Dobbie, M. Myronov, and D. R. Leadley, *High quality relaxed Ge layers grown directly on a Si(001) substrate*, *Solid-State Electronics* **62** (2011).

Thermal rectification in telescopic nanowires

Y. Kaur^{1*}, M. Camponovo¹, M.Y. Swinkels¹, W. Kim², A. Fontacuberta²,
M.L. Suárez³, R. Rurali³, I. Zardo¹

¹ Department Physik, Universität Basel, Klingelbergstrasse 82, CH-4056 Basel, Switzerland

² Laboratory of Semiconductor Materials, Institute of Materials, École Polytechnique Fédérale de Lausanne, 1015 Lausanne, Switzerland

³ Institute de Ciència de Materials de Barcelona, Campus de Bellaterra, 08193 Barcelona, Spain
*corresponding author: yashpreet.kaur@unibas.ch

Photonics and Electronics have reached a high level of control and sophistication in technology today, but heat manipulation still remains a challenge. In this work, heat rectification is being studied in diameter varying semiconducting nanowires referred to as telescopic nanowires. Here, the temperature dependence of thermal conductivity is being used as a tool to manipulate the heat flux. To perform thermal transport measurements which need precise control, devices with suspended bridges are used to apply thermal gradients and to perform resistive and Raman thermometry.

Introduction

In this era, where nanoscale devices have made their way to industry, the problem of heat management still hinders their performances and is a limiting factor. The ultimate control over heat flow is obtained in a thermal diode, a system where heat preferentially flows in one direction. This could be used to more effectively cool closely packed systems in current microchips. Efforts have been made as early as 1936 to demonstrate heat rectification in metals [1], followed by several other theoretical and experimental studies in the 20th and 21th century for thermal rectification like thermal warping, different work functions of the materials, asymmetric phonon conduction mechanisms by mass loading or temperature dependent thermal conductivities. Continuous miniaturization by nanoscaling has opened a whole new world of possibilities to understand, design and realize systems which might eventually lead to development of thermal circuit elements such as diodes, regulators, transistors and switches.

In this work, the temperature dependence of thermal conductivities has been used as a tool to manipulate heat flux to get thermal rectification. Peyrard *et al.* in 2006 through numerical calculations showed that, if we combine two materials with sufficiently different thermal conductivities as a function of space and temperature, one can get a thermal rectifier [2]. Nanos-

tructuring further helps in tuning the thermal conductivity since it provides a hope to tune e.g. boundary scattering; exploiting this effect, thermal rectification in telescopic nanowires was shown through molecular dynamic simulations in 2015 [3]. Here, an account to experimentally demonstrate the concept of thermal rectification in telescopic nanowires has been detailed.

GaAs Telescopic Nanowires

For carrying out thermal transport experiments, semiconducting nanowires of GaAs with abruptly varying diameters have been employed. These nanowires were grown by molecular beam epitaxy using self-assisted Vapor Liquid Solid mechanism at EPFL Lausanne [4]. The diameter of the nanowire is decided by the size of the gallium droplet. These nanowires are referred to as “telescopic” since they have a thick and a thin part with approximate diameters of 350 nm and 100 nm with Zinc Blende and Wurtzite crystal structures, respectively, and are typically few microns (between 10 to 20 μm) in length.

We did Raman spectroscopy to characterize the GaAs phonon modes in the thin and the thick part of the nanowires. The characteristic TO phonon mode for GaAs at 268 cm^{-1} was characterized. The E_2^{H} mode at 257 cm^{-1} which is a fingerprint of the Wurtzite crystal structure,

seemed quenched in the thin part. In addition, the temperature calibration of the TO peak in thick and thin parts was done to get the Raman shift with respect to temperature which was found to be $-0.017 \text{ cm}^{-1}/\text{K}$ and $-0.02 \text{ cm}^{-1}/\text{K}$ in the thin and the thick parts, respectively. This calibration was then used to measure the lattice temperature along the nanowires using Raman thermometry.

Measurement Method

The thermal transport measurements in these nanowires are performed using electronic and optoelectronic techniques to perform resistive and Raman thermometry. Microdevices called as ‘‘Suspended thermal Bridges’’ with two adjacently suspended silicon nitride membranes and long SiN_x beams for thermal isolation are used for performing electronic measurements. The membranes have gold meanders structured on them, which act both as heaters and thermometers [5]. These devices are sensitive to small temperature changes and provide more precise control over the applied thermal gradients. We fabricated these devices using 2-step lithography processes to define the membranes and beams as well as the metal patterns, followed by dry and wet etching to suspend them in air (fig 1a & b). The nanowire is bridged between these membranes using micro-

manipulators (fig 1c). Then, the temperature gradient is applied by sending a current in one side of the device causing a heat flow through the nanowire from hot to the cold side. The amount of heat transported through the nanowire can be measured at the other end of the nanowire by measuring the resistance change on the cold side. Applying energy balance equations for the system, the thermal conductivity of the nanowire can be determined. The same process is repeated by inverting the temperature gradient and measuring the heat flux. If the heat flux is different on reversing the temperature gradients, there is rectification.

To get a temperature profile along the nanowire and complement the electronic measurements, we performed Raman thermometry upon application of a thermal gradient. This gives us information about the temperature drop in the thin and thick parts of the nanowire and the temperature drop at the interface between the thick and thin parts. The thermal gradient is applied electronically in the suspended bridges and Raman spectra are acquired along different positions on the suspended nanowire with and without the gradient. The difference in peak position between these two spectra can be related to the local temperature using the previously discussed calibration.

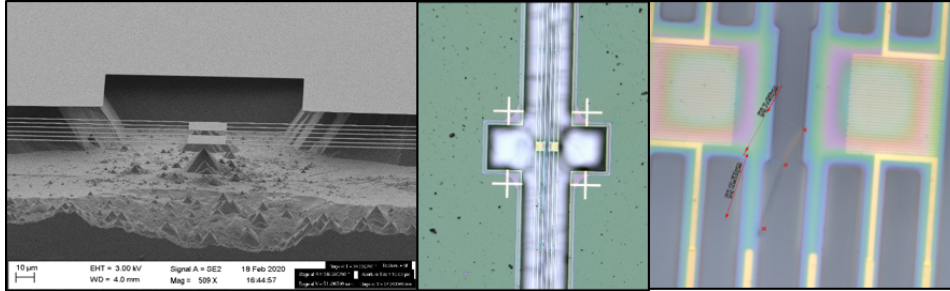


Figure 1:(a) SEM Image of the suspended device- side view (b) Optical image of the suspended device-top view (c) Optical image of a nanowire suspended between the bridges

Results and Discussion

Telescopic nanowires were measured electronically on Suspended bridges by applying thermal gradients of the order of 50 K at base temperature of 300 K. We measured a telescopic nanowire of $20 \mu\text{m}$ length, with thin part $7.5 \mu\text{m}$ long and the thick part $13.6 \mu\text{m}$ long (fig 1c); the thermal conductance of the wire was found to be

$6.08 \times 10^{-9} \text{ W/K}$ in forward direction (thermal gradient from thick to thin part) and $5.48 \times 10^{-9} \text{ W/K}$ in reverse direction (thermal gradient from thin to thick part). This would give us a rectification value of 10% but this is inclusive of the rectification coming from the asymmetry of the device which has to be corrected by additional measurements.

Further, Raman thermal thermometry was performed to extract the temperature profile along this nanowire applying the same gradient at the same base temperature. We observed that most of the temperature drops along the thin part of the nanowire because of its high thermal resistance (fig 2). In principle, the temperature profiles from the thin and thick part can be extrapolated to get the temperature jump at the interface. However, in this case it is rather difficult as the temperature jump is too small to be detected with the experimental sensitivity of this type of measurements. Additionally, we can extrapolate the temperature profiles to the contacts to see the contact resistance; here the contact resistance appears small as the temperature drop between the contact and the wire at thick part is

around 3 K; whereas it is a bit larger on the thin side when used as the hot junction. The error in these measurements is around 5 K by the spectral resolution of the spectrometer. These are the first measurements of its kind on this material system and give us a good insight of the transport along the axis of the nanowire. However, more measurements with large gradients and lower base temperatures are needed to study the interface contribution and achieve sizeable rectification.

Acknowledgement

This project has received funding from European Research Council under the European Union's Horizon 2020 research and innovation program (grant No 756365 and through grant 'INDEED').

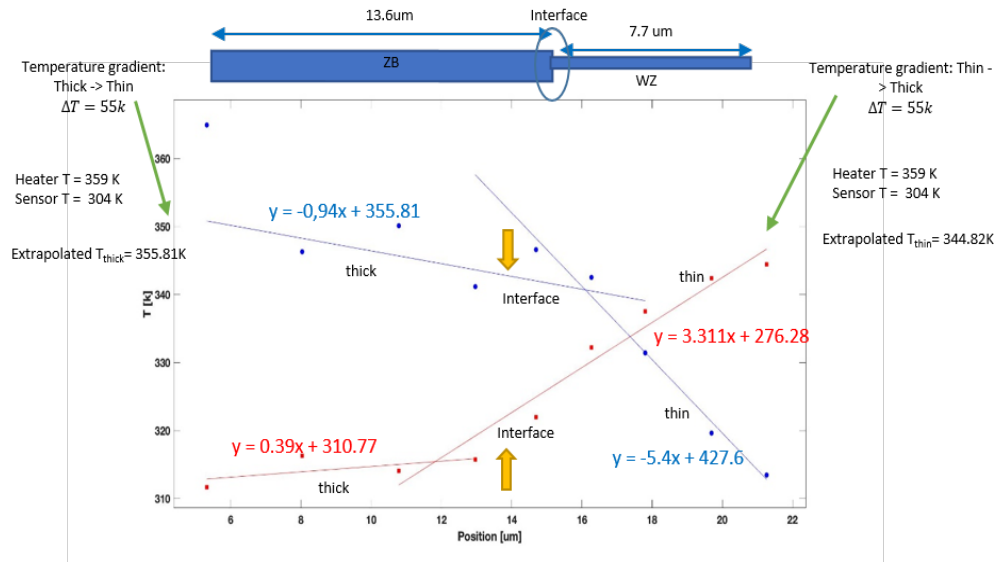


Figure 2: Temperature profile of the telescopic nanowire on reversing temperature gradients

References

- [1] Starr, C., 1936. The copper oxide rectifier. *Physics*, 7(1), pp.15-19.
- [2] Peyrard, M., 2006. The design of a thermal rectifier. *EPL (Europhysics Letters)*, 76(1), p.49.
- [3] Cartoixà, X., Colombo, L. and Rurali, R., 2015. Thermal rectification by design in telescopic Si nanowires. *Nano letters*, 15(12), pp.8255-8259.
- [4] Kim, W., Dubrovskii, V.G., Vukajlovic-Plestina, J., Tutuncuoglu, G., Francaviglia, L., Guniat, L., Potts, H., Friedl, M., Leran, J.B. and Fontcuberta i Morral, A., 2018. Bistability of contact angle and its role in achieving quantum-thin self-assisted GaAs nanowires. *Nano letters*, 18(1), pp.49-57.
- [5] Shi, L., Li, D., Yu, C., Jang, W., Kim, D., Yao, Z., Kim, P. and Majumdar, A., 2003. Measuring thermal and thermoelectric properties of one-dimensional nanostructures using a microfabricated device. *J. Heat Transfer*, 125(5), pp.881-888.

Electrical and optical techniques to observe hydrodynamic phonon transport in 2D materials

Giulio de Vito*,¹ Grazia Raciti*,¹ Begoña Mayor,¹ Aswathi K. Sivan,¹ Milo Yaro Swinkels,¹ and Ilaria Zardo¹

¹*Nanophononics Group, Department of Physics, University of Basel, CH-4056 Basel, Switzerland*

In recent years, the CMOS technology has demanded new materials for heat dissipation, that could improve computing performances. 2D materials in hydrodynamic regime became the focus of interest because they display a remarkable heat conductivity.

Materials like Graphene and Hexagonal Boron Nitride, in a temperature window between 50 K and room temperature, exhibit hydrodynamic heat conduction. In this condition, the quasi-particles heat carriers, phonons, have a behavior similar to water molecules in a plumbing. Little is known nowadays due to the novelty of the subject and limited experimental protocols.

This abstract provides a description of an experimental protocol to probe heat hydrodynamic transport. A pump-probe setup capable of transient thermal reflectivity measurements and Raman spectroscopy is presented together with a new MEMS device that combines electrical measurements with Raman spectroscopy.

* Presenters

Contacts: giulio.devito@unibas.ch; grazia.raciti@unibas.ch

Website: www.nanophononics.physik.unibas.ch

I. HEAT HYDRODYNAMIC

In the past decades, the increasing demand for effective thermal management of microelectronic devices and efficient thermoelectrics has raised the need for new materials with extremely high thermal conductivity. In the last century, a new phenomenon of heat transport emerged that resemble wave propagation in liquids, known as heat hydrodynamic. This effect arises when normal phonon scattering dominates over Umklapp scattering, thus implying that the phonon momentum is mainly conserved and, consequently, temperature fluctuations can be observed. This is known as *Second Sound* and it was experimentally discovered in superfluidic helium in 1944 [1], NaF [2] and graphite samples [3], [4]. A timescale in between the normal and the Umklapp phonon scattering time ($\tau_N < \tau_{exp} < \tau_U$) is needed to investigate second sound phenomena. Theoretical studies have predicted for graphene [5] a nanosecond timescale to observe second sound. Therefore, pump-probe spectroscopy experiments are well suited for measuring the thermal response at this timescale.

II. PUMP-PROBE EXPERIMENTAL SETUP

Ultrafast pump-probe technique provides a powerful tool to investigate thermal transport properties at a sub-picosecond timescale. It consists of an ultrashort pulsed laser, the pump, which is used to bring the system out of equilibrium. Then a second pulsed laser, the probe, is sent on the sample to measure the effect of the pump excitation as a function of time. A mechanical delay line enables to control the time delay between the pump and the probe. Thus, we can monitor the system evolution as a function of the time delay between the two beams. Figure 1 shows the schematic of our pump-probe setup

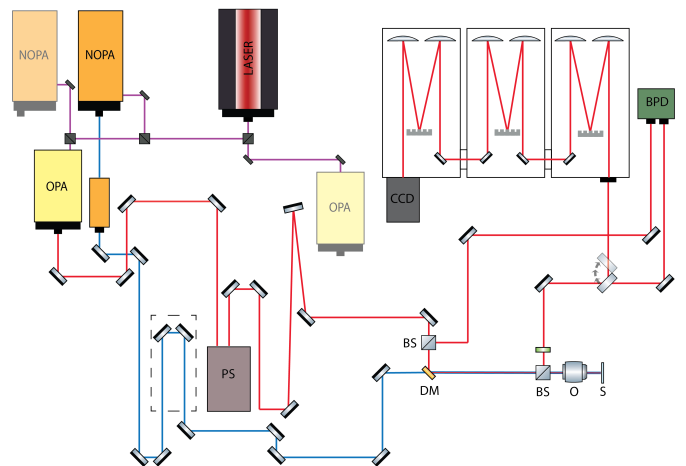


FIG. 1. **Scheme of the pump-probe setup.** A femtosecond pulsed laser is split into two beams. One of them, the probe, goes through an optical parametric amplifier (OPA), the other one, the pump, goes through a non-collinear optical parametric amplifier (NOPA). A mechanical delay line in the pump path produces a variable time delay between pump and probe, that allows to follow the time evolution of the system on sub-picosecond scale. Two different detection systems are used to realize either TRRS or TR. A pulse shaper (PS) is used to tune the pulse duration and increase frequency resolution, and a triple spectrometer is used to realize Raman spectroscopy. Instead in TR, a balanced photodiode (BPD) is used to reconstruct the changes in reflectivity of the sample.

which can be used to realize both time-resolved Raman spectroscopy (TRRS) or transient reflectivity (TR) experiments. TRRS is an inelastic light scattering and non-destructive technique that allows the investigation of the

phonon dynamics in nanostructures [6]. This technique is able to track the temporal evolution of specific phonon modes, moreover we directly measure the effective lattice temperature. This makes TRRS a unique technique to study ultrafast lattice dynamics of materials.

TR technique is widely applied to examine the thermal properties of materials. It monitors the change in reflectance as a function of time on a sub-picosecond scale [7]. This change in reflectance, induced by the change in the material's dielectric constant generated by the heat pulse, can then be used to understand light matter interaction and extract transport properties, such as the electron-phonon coupling as well as the thermal conductivity[8].

Using TRRS we are able to map the temperature profile of a phonon mode over time, and reconstruct the wave-like propagation of the heat which is a fingerprint of hydrodynamic heat transport[4]. Instead, TR gives us information about the decay channels of electrons into phonons and how both systems relax towards equilibrium. Therefore, it provides access to the average phonon behavior in the materials.

III. SUSPENDED FOUR TERMINAL BRIDGES

Probing a deviation of heat flow from the Fourier's law requires a highly sensitive device and good isolation from the environment. A suspended four terminal device, with thermometer coils placed on top of a bridged silicon nitride (SiNx) membranes, is fabricated. This device enables to simultaneously perform electrical and thermal measurement by the means of Joule effect and Raman thermometry. It provides optimal isolation from the environment while assessing the thermal conductivity of the specimen under investigation.

The four coils are made of platinum and are placed on top of SiNx membranes, which are bridged to the surrounding by SiNx beams. The beams provide mechanical stability and loose thermal conductance to the environment. By electrically heating one coil is possible to generate an heat pulse that raises the temperature in the membrane, therefore it heats one side of the sample. The remaining membranes can be used as sensors to probe the change in temperature in their respective sides. Since in our newly designed devices there are four coils, it is possible to probe temperature in several points of the sample or swap the heating sides with the sensor side.

Fabrication

A 2-inches Si wafer is taken and a SiNx layer is deposited on both sides. On one side an etching mask is patterned using laser lithography, then through reactive ion etching (RIE) the SiNx is removed, opening windows for the first Si wet etching. The first wet etching is performed using sodium hydroxide (NaOH) and potassium hydroxyde (KOH), this creates through out holes in the silicon that

can be used as markers for the other side of the wafer. At the same time, a fine mesh of 19 μm squares are etched to partially remove silicon under the devices. On the other side, a photoresist mask is patterned through laser lithography to deposit the gold metal contacts for electronic characterization, followed by lift off in acetone to remove the exceeding metal. Using the markers created in the previous step, the gold contacts are aligned with the sites where the devices will be suspended. PMMA photoresist is laid on top of gold to perform an electron beam lithography (EBL), to define the thermometers on top of the membranes through platinum evaporation and lift off. At this point another laser photolithography step, to outline the suspended SiNx beams of the membranes, is performed and the sample to investigate (Graphene, hBN, others 2D materials) is transferred onto the membranes. Finally, Si wet etching using KOH is done to complete the suspension of the device.

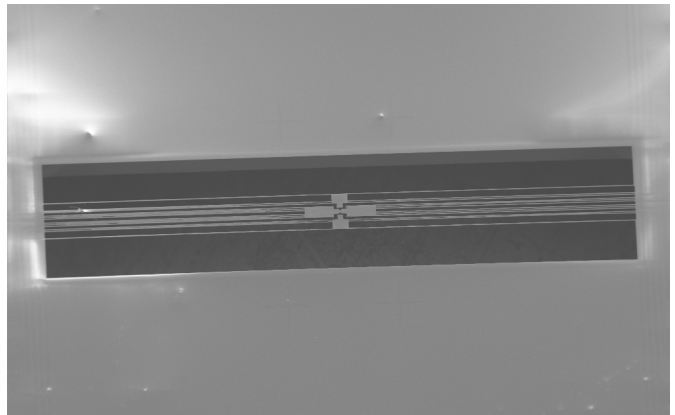


FIG. 2. **Suspended thermometer, four terminal device.** Tilted view of the suspended thermometer taken in the SEM after the second wet etching of silicon. In the centre there are visible four suspended membrane of SiNx with the platinum meanders on top, the two central membranes are connected to each other, while the other two side membranes are just suspended by the beams. Not visible in the image, there are the gold pads, on the extreme sides of the image, for electrical connection, those are linked to the meanders in the center through gold lines on top of the beams. This image is acquired through S.E.M. machine based in the physic department of the University of Basel.

Combined measurements

Once the fabrication is completed, the sample can be assessed by Raman spectroscopy to map the temperature distribution of the flake. The coils generate heat pulses or fix the temperature on one side of the sample, while the remaining coils can measure the temperature of the sample's sides on top of the other membranes. Since the device is suspended on a through-out hole, the laser beams can be sent and collected from the top and bottom of the flake and TEM analysis or mechanical vibrational

modes measurements can also be performed.

ACKNOWLEDGMENTS

We acknowledge both Eucor, The European Campus, and SNSF, the Swiss National Science Foundation (Project Grant No. CRSII5_189924), for financial support this project. The QUSTEC program has received funding from the European Union's Horizon 2020 research and innovation program under the Marie Skłodowska-Curie grant agreement number 847471.

-
- [1] R. D. Maurer and M. A. Herlin, *Second Sound Velocity in Helium II*, Physical Review **76**, 948 (1949), URL <https://journals.aps.org/pr/abstract/10.1103/PhysRev.76.948>.
- [2] T. F. McNelly, S. J. Rogers, D. J. Channin, R. J. Rollefson, W. M. Goubau, G. E. Schmidt, J. A. Krumhansl, and R. O. Pohl, *Heat Pulses in NaF: Onset of Second Sound*, Physical Review Letters **24**, 100 (1970), URL <https://journals.aps.org/prl/abstract/10.1103/PhysRevLett.24.100>.
- [3] Y. Machida, N. Matsumoto, T. Isono, and K. Behnia, *Phonon hydrodynamics and ultrahigh-room-temperature thermal conductivity in thin graphite*, Science **367**, 309 (2020), ISSN 10959203, URL <http://science.sciencemag.org/>.
- [4] S. Huberman, R. A. Duncan, K. Chen, B. Song, V. Chiloyan, Z. Ding, A. A. Maznev, G. Chen, and K. A. Nelson, *Observation of second sound in graphite at temperatures above 100 k* downloaded from, Science (2019).
- [5] S. Lee, D. Broido, K. Esfarjani, and G. Chen, *Hydrodynamic phonon transport in suspended graphene*, Nature Communications **6** (2015), ISSN 20411723.
- [6] R. B. Versteeg, J. Zhu, P. Padmanabhan, C. Boguschewski, R. German, M. Goedecke, P. Becker, and P. H. V. Loosdrecht, *A tunable time-resolved spontaneous raman spectroscopy setup for probing ultrafast collective excitation and quasiparticle dynamics in quantum materials*, Structural Dynamics **5** (2018), ISSN 23297778.
- [7] S. Sandell, E. Chávez-Ángel, A. E. Sachat, J. He, C. M. S. Torres, and J. Maire, *Thermoreflectance techniques and raman thermometry for thermal property characterization of nanostructures*, Journal of Applied Physics **128** (2020), ISSN 10897550.
- [8] M. Segovia and X. Xu, *High Accuracy Ultrafast Spatiotemporal Pump-Probe Measurement of Electrical Thermal Transport in Thin Film Gold*, Nano Letters p. [acs.nanolett.1c02210](https://pubs.acs.org/doi/10.1021/acs.nanolett.1c02210) (2021), ISSN 1530-6984, URL <https://pubs.acs.org/doi/10.1021/acs.nanolett.1c02210>.

Towards Andreev Spin Qubits with Proximitized InAs 2DEG

Carlo Ciaccia,¹ Jann Hinnerk Ungerer,¹ Luk Yi Cheung,¹ Libin Wang,¹ Artem Kononov,¹ Michael J. Manfra,^{2,3,4,5,6} Thomas Reisinger,⁷ Ioan Pop,^{7,8} and Christian Schönenberger^{1,9}

¹*Quantum- and Nanoelectronics Lab, University of Basel, CH-4056 Basel, Switzerland*

²*Department of Physics and Astronomy, Purdue University, West Lafayette, Indiana 47907, USA*

³*Birck Nanotechnology Center, Purdue University, West Lafayette, Indiana 47907, USA*

⁴*Microsoft Quantum Purdue, Purdue University, West Lafayette, Indiana 47907, USA*

⁵*School of Electrical and Computer Engineering,*

Purdue University, West Lafayette, Indiana 47907, USA

⁶*School of Materials Engineering, Purdue University, West Lafayette, Indiana 47907, USA*

⁷*IQMT, Karlsruhe Institute of Technology, Eggenstein-Leopoldshafen 76344, Germany*

⁸*Physikalisches Institut, Karlsruhe Institute of Technology, Karlsruhe 76131, Germany*

⁹*Swiss Nanoscience Institute, University of Basel, Klingelbergstrasse 82, Basel, Switzerland*

The realization of a scalable quantum computing platform has been one of the most active research areas in the last decade. Different approaches have been explored, for instance, trapped ions, silicon quantum dots, diamond vacancies, and superconducting qubits. In this proposal, we take a different route and aim at the realization of a Andreev qubit based on an InAs 2DEG proximitized with an epitaxial Al layer. We plan to couple a planar Josephson junction to a high impedance half-wavelength microwave resonator. The goal is to couple the quasiparticle spin to the resonator via electric field fluctuations. This is enabled thanks to the large Spin Orbit Interaction in InAs.

4.1 Zurich Instruments

Your Qubits. Controlled.

Meet the next generation quantum computing control system setting new standards for the control, readout and error correction of superconducting qubits.

- Up to 8.5 GHz without mixer calibration
- Optimal readout and gate fidelity
- Fast system tune-up and characterization
- Fully integrated room-temperature setup
- Scalable to about 100 qubits



Contact us today
www.zhinst.com

4.2 Linktronix

Tektronix[®]

—

SOLUTIONS FOR SCIENTIFIC AND ENGINEERING RESEARCH





SOLUTIONS FOR SCIENTIFIC AND ENGINEERING RESEARCH

You'll find Tektronix at the frontier of science and technology, partnering with engineers and scientists to find solutions to the most cutting-edge challenges.

Our products and solution offerings enable you to capture, measure, analyze and simulate the physical world with ever-increasing ease and insight and in compliance with the most up-to-date standards.

- Quantum
- High Energy Physics
- Optical Communications
- Nanotechnologies
- Energy and Efficiency Research
- Next Generation Wireless

[TEK.COM](https://www.tek.com)

QUANTUM RESEARCH – FLEXIBLE, LOW NOISE SIGNALS FOR TRIGGERING QUBITS

There's a race going on to develop technology based on uniquely quantum or subatomic phenomena. Institutions are working to take data processing to the next level through quantum computing. Laboratories are studying and developing applications of quantum entanglement to create instantaneous communication anywhere in the universe. We are standing at the edge of a new age of science and potentially the birth of new, culture shifting technologies.

It may not sound like a quantum computer, a miles long laser-interferometer and a quantum entanglement have much in common, but when you zoom out, these technological developments all face similar challenges. How do you set up the signals that trigger what you want to observe? How do you ensure timing? How do you scale up a solution?

8 Channels, 16 Bit Resolution.
Less Noise. Cleaner Signals.

The New Tektronix 5200A Arbitrary Waveform Generator combines high signal fidelity at a low cost with scalability. With code compatibility you can fast forward integration and scaling while simplifying waveform design. Test and validate complex, sensitive devices with the accuracy and quality you expect from Tektronix AWG's.

Oscilloscopes for Troubleshooting and High-Speed Acquisition

Tektronix builds oscilloscopes for applications ranging from basic undergraduate lab work, to microwave signal analysis. Mixed Domain Oscilloscopes like the MDO3000 Series and MDO4000C Series combine an oscilloscope and spectrum analyzer in one instrument, providing visibility in both the time and frequency domains. They include digital inputs so you can see as many as 20 analog and digital signals at once.

The MDO4000C lets you see both time and frequency information at the same time, so you can see how a spectrum changes with respect to other signals in the system. The MSO/DPO70000C/DX/SX Series provides high-speed signal acquisition performance up to 70GHz and 200 GS/s with over 30 customizable application-specific software analysis packages.

Resources

[Measurement System Signal Integrity: Important Factors to Consider –](#)

Sufficient bandwidth is a key oscilloscope requirement for making accurate measurements. However, there are a number of other factors and specifications that can help you properly perform signal integrity characterization.

[Fundamentals of the MDO4000 Series Mixed Domain Oscilloscope –](#)

Learn how a Mixed Domain Oscilloscope (MDO) offers time-correlated analog, digital, and RF signal acquisition for a complete system view. Discover the benefits of seeing both the time and frequency domains in one glance, and the advantages of viewing RF spectrum changes over time.

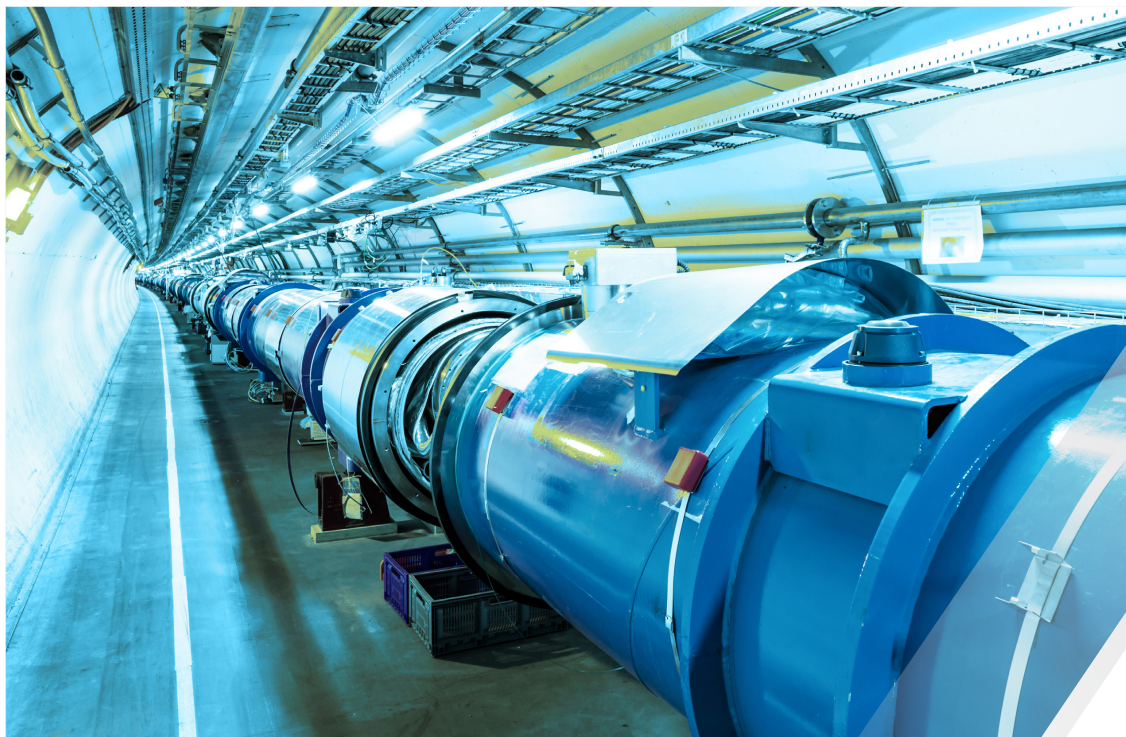
[XYZ's of Signal Generators Primer –](#)

Explains the basics of Signal Generators, including the many types of generators, their applications and their contribution to a complete test and measurement solution.

[Overcoming RF Signal Generation Challenges in Quantum Computing with New DAC Technologies White Paper –](#)

In this document, some important features for direct RF complex signal generation are presented followed by a discussion on two architectural techniques that can expand frequency coverage with a focus on reducing cost and complexity for multi-channel applications.

TEK.COM



HIGH ENERGY PHYSICS – MEASURING AT HIGH-SPEED

With new and compelling questions about the origin of particle masses, the nature of dark matter and the role of neutrinos, scientists need instruments that can capture or simulate fleeting events that represent the world of fundamental particles. Our oscilloscopes are used in the quest to achieve longer-duration reactions, such as high gain nuclear fusion, to capture high-speed pulses and to test the latest generation of accelerators and synchrotrons.

TEK.COM



The World's Standard in Oscilloscopes

Scientists around the world trust Tektronix to capture high-speed pulses and test the latest generation of accelerators and synchrotrons. With the broadest portfolio of digital oscilloscopes available, the most extensive analysis capability, and our award-winning service and support, Tektronix has the right oscilloscope to meet your needs.

The World's Fastest and Most Versatile Signal Generators for Today's Complex Signals

With sample rates up to 50 GS/s, our 10-bit digital-to-analog technology enables AWG70000 Series Arbitrary Waveform Generators to cover a wide range of HEP applications, from replicating pulse detector signals to generating RF events. These signal generators can create virtually any signal - analog or digital, ideal or distorted, standard or custom. RFXpress software lets you experiment with complex RF/IF/IQ waveforms. SerialXpress helps you build serial data streams on your PC. And ArbExpress is free, general purpose waveform editing software that lets you develop signals to simulate real world events.

World's Leading Step, Pulse, and Impulse Generators

Our pulse generators provide ultra-performance in a broad range of dimensions for step, pulse and impulse sources. These include shortest transition time, most versatile risetime/falltime control, maximum frequency and duration control and high signal amplitudes, providing the highest performance for this class of source products.

Real-Time Spectrum Analyzers

Real time spectrum analyzers are invaluable for tracking high-frequency electromagnetic interference and characterizing transient RF events.

Resources

[Fundamentals of Signal Integrity](#)

Primer – Review the challenges associated with sending and receiving high-speed signals. Learn measurement techniques that may be used to uncover problems and characterize performance.

[Fundamentals of Real-Time Spectrum](#)

Analysis Primer – Find out how real-time spectrum analyzers reliably detect and characterize rapidly changing RF signals.

[Asynchronous Time Interleaving](#)

White Paper – Introduces new technology that extends the bandwidth performance of real-time oscilloscopes to 70 GHz.

[XYZs of Signal Generators Primer](#)

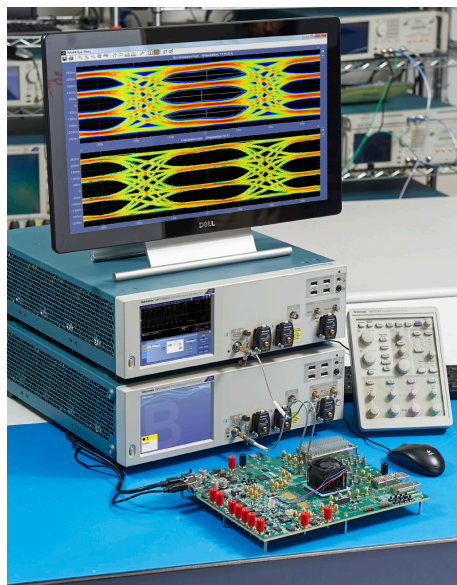
Explains the basics of Signal Generators, including the many types of generators, their applications and their contribution to a complete test and measurement solution.



OPTICAL RESEARCH – A COMPLETE RX/TX MEASUREMENT SOLUTION

Whether you work on optical components, transceiver sub-assemblies or transmission systems, there are critical PHY layer tests that need to be done: eye diagrams and jitter performance, stressed receiver testing, crosstalk & BER tests, and optical modulation analysis. Tektronix provides you with the expertise and equipment to perform standards compliant TX, RX and Coherent Optical testing to 400 Gb/sec and beyond.

As network demands increase, long-haul communications are becoming more complex. Advanced test tools are required to test the latest communication systems for 100G, 400G, 1Tb/s and beyond. Tektronix is the only test and measurement vendor that can offer a complete coherent optical test system from signal generation to modulation, coherent detection, acquisition, and analysis.



Signal Acquisition and Analysis: The World's Lowest-Noise, Real-Time Oscilloscope and More

The MSO/DPO70000C/DX/SX Series oscilloscope delivers exceptional signal acquisition performance and analysis capability. The DPO70000SX 70 GHz oscilloscope provides the industry's lowest-noise real time acquisition using Tektronix' patented Asynchronous Time Interleaving (ATI) technology. Discover your real signals with uncompromised acquisition on all 4 channels and capture more signal details with the industry's highest waveform capture capability. Automate setup, acquisition and analysis of high-speed serial data signals with a toolset engineered to deliver faster design and compliance testing.

All Tektronix high performance oscilloscopes, can be equipped with SignalVu Vector Signal Analysis (VSA) Software for wideband modulation analysis. In coherent optical research, SignalVu Software helps with phase correction using multi-tone calibration. It is ideal for demodulating orthogonal frequency division multiplexing (OFDM) modulation.

TEK.COM



DSA8300 Series Sampling

Oscilloscopes are suitable for accurate characterization of optical transmitter performance using built-in optical reference receivers and very low jitter noise floor. With an industry-leading intrinsic jitter of less than 100 fs, the DSA8300 Series provides support for today's optical communications standards, time domain reflectometry and S-parameter analysis. The DSA8300 Digital Sampling Oscilloscope is a complete high-speed PHY Layer testing platform for data communications from 155Mb/sec to 100G.

The OM4245 Coherent Optical Modulation Analyzer, together with the MSO/DPO70000SX 70 GHz Series oscilloscopes, makes an ideal coherent optical signal acquisition system for 400G, 1Tb/s and beyond. The OM4245 optical modulation analyzer provides laboratory instrument-grade optics and optical-to-electrical conversion capable of handling the latest coherent optical signals up to 80 GBaud. The OM2210 Coherent Receiver Calibration Source provides a simple solution for calibrating the OM4245 or other coherent receivers.

Developed specifically for coherent optical analysis, OM1106 Coherent Lightwave Signal Analyzer software provides state-of-the-art demodulation, measurements and visualization tools for all of today's coherent optical standards. It also includes support for spatial (or modal) division multiplexing that requires an OMA to down convert and digitize data for each channel. Multi-carrier communication applications also require one OMA per wavelength channel when the

wavelength separation is more than the OMA bandwidth. Unique MATLAB integration provides unparalleled levels of algorithm, signal processing, and workflow customization. The OM1106 analysis software is available separately or included with the OM4245 Coherent Optical Modulation Analyzer.

Setting the Standard for Signal Generation

The AWG70000 Series of arbitrary waveform generators represents the cutting edge in sample rate, signal fidelity and waveform memory. The AWG70000 Series can reach sampling rates as high as 50 GS/s with 10 bits vertical resolution, enabling creation of multi-level signals such as 16QAM or 64QAM at up to 32 GBaud data rates. Up to 4 instruments can be synchronized to provide 4 channels at 50 GS/s each.

The AWG5200 Series of arbitrary waveform generators deliver the industry's best combination of sample rate and vertical resolution at a surprisingly low price. Create real-life environments based on accurate, noise-free signals, and 10 GS/s 16-bit performance that allows for direct generation of signals up to 6 GHz.

The PPG3000 Series is capable of generating patterns up to 40 Gb/s and offers up to 1, 2, or 4 channels in a single instrument for creation of dual-polarization I-Q waveforms.

The OM5110 Multi-format Optical Transmitter provides the flexibility to modulate all of the most common coherent optical formats at rates up to

46 GBaud. The OM5110 Multi-Format Optical Transmitter is a C- and L-Band transmitter capable of modulating the most common coherent optical modulation formats such as PM-QPSK and PM-16QAM. For those who are testing multi-carrier systems, the OM2012 Tunable Laser provides extra lasers in both C- and L-band.

Bit Error Rate Testing

PatternPro® PPG and PED Series Single and Multi-Channel Pattern Generators and Error Detectors are ideal for simultaneous BER testing of up to four lanes at 32Gb/s, and now include pattern generation and error detection capability at rates up to 40 Gb/s.

BERTScope BSA Series Bit Error Rate Testers use long pseudo-random patterns and accurate BER measurements for comprehensive signal integrity measurements on communications systems up to 28 Gb/s.

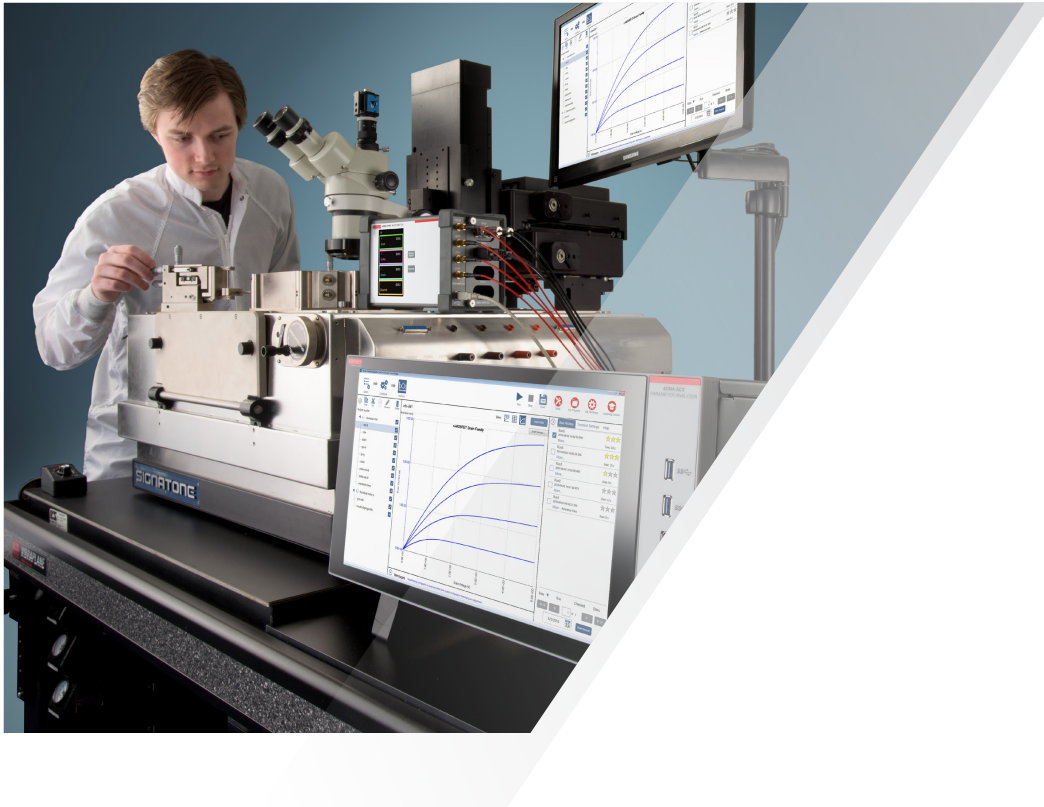
Resources

[Physical Layer Tests of 100 Gb/s Communications Systems App Note](#) –

Learn how to prepare for compliance measurements on 100G standards.

[Coherent Optical Signal Generation with High Performance Arbitrary Waveform Generator App Note](#) –

Learn how instrument characteristics influence the ability to generate different modulation schemes, how to compensate for internal and external device imperfections, and to emulate component and link distortions.



NANOTECHNOLOGY – ADVANCED MEASUREMENT FOR ADVANCED MATERIALS

If you're researching or developing the materials or devices of the future like silicon-based compound semiconductors, thin film for solar cells, graphene and other nanoscale materials, you're at the fore-front of breakthroughs in new applications in semiconductor technology, electronics, medical devices, health care and more.

Our comprehensive solutions for electrical characterizations of new materials and devices can help you innovate further and reimagine our world.

TEK.COM

Source-Measure Units- (SMU) Instruments

Source-measure units or SMUs are ideal instruments for making nanoscopic material and device measurements. They are a smart alternative to separate power supplies and digital multimeters (DMMs). Keithley SourceMeter@SMU instruments combine a power supply, true current source, 6.5-digit DMM, arbitrary waveform generator, V or I pulse generator with measurement, electronic load and trigger controller in one instrument with a convenient DMM-like user interface.

A source and measure unit can rapidly switch from outputting a specified voltage and accurately measuring the resulting current, to the other way around. When materials such as carbon nanotubes (CNTs) or graphene are in a high impedance state, the SMU can source voltage and measure current quickly and accurately. When the material is in a low impedance state, the SMU can quickly reconfigure to source current and measure voltage. Furthermore, the SMU has a current compliance function that can automatically limit the DC current level to prevent damage to the material or device under test (DUT).

From 3000V to 10nV and 50A pulse to 1fA, Keithley's family of SourceMeter SMU instruments offers the broadest measurement range available. Each is fully programmable and provides higher precision, resolution and flexibility for materials research, semiconductor devices (transistor, BJT, diode, power MOSFET, power semi, LED), electronic circuits, and more.



Highest Performance Parameter Analyzer

Keithley's 4200A-SCS is a modular, customizable, and fully-integrated parameter analyzer that provides synchronized insight into current-voltage (I-V), capacitance-voltage (C-V), and ultra-fast pulsed I-V electrical characterization. Its optional 4200A-CVIV Multi-switch module enables effortless switching between I-V and C-V measurements without re-cabling or lifting probe needles. Offering up to 2X faster characterization insight, the 4200A-SCS accelerates testing of complex devices for materials research, semiconductor device design, process development or production.

Keithley also offers the industry's most complete line of picoammeters, electrometers and nanovoltmeters for highly sensitive voltage, current and resistance measurements for nanoscience applications.

Resources

[Advances in Electrical Measurements for Nanotechnology eBook](#) – Learn why sensitive electrical measurement tools are essential for nanoscience research. Understand how these tools provide the data needed to understand the electrical properties of new materials fully and the electrical performance of new nanoelectronic devices and components.

[Electrical Characterization of Carbon Nanotube Transistors \(CNT FETs\) with the Model 4200-SCS Parameter Analyzer App Note](#) – Learn how to perform IV characterization on carbon nanotube FETs.



ENERGY AND EFFICIENCY RESEARCH – MEASURING FOR TODAY AND TOMORROW

Sustainable energy research aims to meet the energy needs of the present without sacrificing the ability of future generations to meet their needs. The technologies are wide-ranging, including renewable energy sources, such as hydroelectricity, solar energy, wind energy, wave power, geothermal energy, artificial photosynthesis, and tidal power. Sustainable energy research also aims to improve energy efficiency and power consumption on widely used power converters, electronics, common appliances and battery operated portable devices. Tektronix offers several categories of instruments in the areas of precision power measurement, waveform analysis, transducers (probing), and semiconductor characterization.

TEK.COM



Power Analyzers for Accurate Power Measurements

Power analyzers are designed especially for making accurate power measurements on a wide range of power conversion systems: from cell-phone chargers to 1000 kW grid-connected inverters. PA3000 Series Power Analyzers can be configured with one to four input channels for testing three-phase devices, or for testing input and output power simultaneously. The PA3000 also includes special modes for testing efficiency and standby power on power supplies, PWM motor drives, LED drivers and lighting ballasts. The PA1000 is designed for precision power analysis and testing power consumption on single phase applications such as appliances, power supplies and hand tools. Both analyzers enable you to measure conversion efficiency and perform pre-compliance testing.

Power Supply Switching Analysis

A significant amount of power is lost during FET switching, and many Tektronix oscilloscopes can be outfitted with special power analysis software to quantify this important switching loss. For example, an MSO/DPO5000B equipped with DPOWR power analysis software can measure switching loss, magnetic loss, safe operating area and harmonics.

IsoVu isolated measurement systems combine bandwidth up to 1GHz, common mode rejection of 10000:1 and complete optical isolation to enable accurate measurements on next generation GaN and SiC switching devices.

Making High-speed Current Measurements

Making accurate current amplitude measurements even at high slew rates is critical to achieving maximum power efficiency. Tektronix current probes provide industry-leading measurement sensitivity down to 1mA and bandwidths up to 100 MHz. When paired with today's Tektronix oscilloscopes the latest current probes automatically scale the readings to amperes and provide status information right on the oscilloscope display. The IsoVu isolated measurement system can also be used to measure current across shunt resistors up to 1 GHz.



Resources

[Power Supply Measurement and Analysis Primer](#) – Discover how to make many common power measurements including switching loss, safe operating area, magnetic power loss, and harmonic analysis.

[Testing Power Semiconductor Devices with Keithley High Power System SourceMeter SMU Instruments](#) – Learn about the most commonly performed power semiconductor device tests, the challenges associated with them, and how SMU instruments can simplify the testing process.



NEXT GENERATION WIRELESS – SPEEDING INTO THE FUTURE

If you're working in 5G you're developing new protocols, like WiGig, while simultaneously designing and creating devices to meet these, as yet, undefined standards. You're chasing the dream of ever lower latency and higher data rates, operating with the lowest possible power. And you're also chasing impossible deadlines.

At Tektronix, we're continuously developing new measurement tools and solutions to advance world-changing research and innovations. From higher speeds for cutting edge performance, to built-in tests for ease-of-use, our solutions are designed to get you the insights you need quickly and efficiently.

[TEK.COM](https://www.tek.com)



Real-Time Spectrum Analyzers

Our RSA spectrum analyzer series provides the speed and real-time capability to help you find elusive transient signals quickly and efficiently. The disaggregated form factor enables a lower cost and more flexibility as you use the same software package across the range. They range from 40 MHz bandwidth RSA306B handheld spectrum analyzers to RSA7100 RF recording and analysis solution with up to 800MHz of real-time bandwidth.

Ultra-Low Power Analysis Solution

Our Keithley digital multi-meters and high performance power supply solutions enable you to characterize total power consumption of your device. Measure performance when the device is in sleep or active mode, capture transients that last microseconds and measure current change as the battery discharges.



The World's Highest Bandwidth, Real-Time Oscilloscope

The DPO70000SX 70 GHz oscilloscope provides the most accurate real-time performance for ultra-bandwidth applications. Coupled with SignalVu Option SV30 software, the DPO70000SX offers 2.5 percent (-32.0 dB) error vector magnitude (EVM) precision for the industry's most accurate solution for wide bandwidth, with a single instrument that uses zero down-conversion.

6-in-1 Versatility in One Powerful Oscilloscope

Our Mixed Domain Oscilloscope series includes up to six built-in instruments, each with exceptional performance to address tough challenges. Every MDO4000C features powerful triggering, search and analysis. The only scopes to offer synchronized analog, digital and RF signal analysis at the same time, so you can view events across domains simultaneously.

Resources

[WiGig Case Study](#) – Learn more about how Tektronix DPO70000SX was used to overcome WiGig test and measurement challenges.

[WiGig Webinar](#) – Focusing on how this technology is being commercially adopted and the challenges related to that adoption, this webinar features insights on the key factors to consider when performing transmitter testing to IEEE 802.11ad.

[Determining Power Consumption and Battery Life in Low Power . Portable IoT Devices Webinar](#) – presents options for measuring power consumption, simulating a battery and creating a model of a battery to provide an optimum solution for assessing battery life.

Contact Information:

Australia* 1 800 709 465
Austria 00800 2255 4835
Balkans, Israel, South Africa and other ISE Countries +41 52 675 3777
Belgium* 00800 2255 4835
Brazil +55 (11) 3759 7627
Canada 1 800 833 9200
Central East Europe / Baltics +41 52 675 3777
Central Europe / Greece +41 52 675 3777
Denmark +45 80 88 1401
Finland +41 52 675 3777
France* 00800 2255 4835
Germany* 00800 2255 4835
Hong Kong 400 820 5835
India 000 800 650 1835
Indonesia 007 803 601 5249
Italy 00800 2255 4835
Japan 81 (3) 6714 3010
Luxembourg +41 52 675 3777
Malaysia 1 800 22 55835
Mexico, Central/South America and Caribbean 52 (55) 56 04 50 90
Middle East, Asia, and North Africa +41 52 675 3777
The Netherlands* 00800 2255 4835
New Zealand 0800 800 238
Norway 800 16098
People's Republic of China 400 820 5835
Philippines 1 800 1601 0077
Poland +41 52 675 3777
Portugal 80 08 12370
Republic of Korea +82 2 6917 5000
Russia / CIS +7 (495) 6647564
Singapore 800 6011 473
South Africa +41 52 675 3777
Spain* 00800 2255 4835
Sweden* 00800 2255 4835
Switzerland* 00800 2255 4835
Taiwan 886 (2) 2656 6688
Thailand 1 800 011 931
United Kingdom / Ireland* 00800 2255 4835
USA 1 800 833 9200
Vietnam 12060128

* European toll-free number. If not accessible, call: +41 52 675 3777

Find more valuable resources at TEK.COM

Copyright © Tektronix. All rights reserved. Tektronix products are covered by U.S. and foreign patents, issued and pending. Information in this publication supersedes that in all previously published material. Specification and price change privileges reserved. TEKTRONIX and TEK are registered trademarks of Tektronix, Inc. All other trade names referenced are the service marks, trademarks or registered trademarks of their respective companies.
03/17 EA 55W-30503-2

